African Journal of Engineering Research and Innovation

AJERI Vol 1. No. 1. 2023

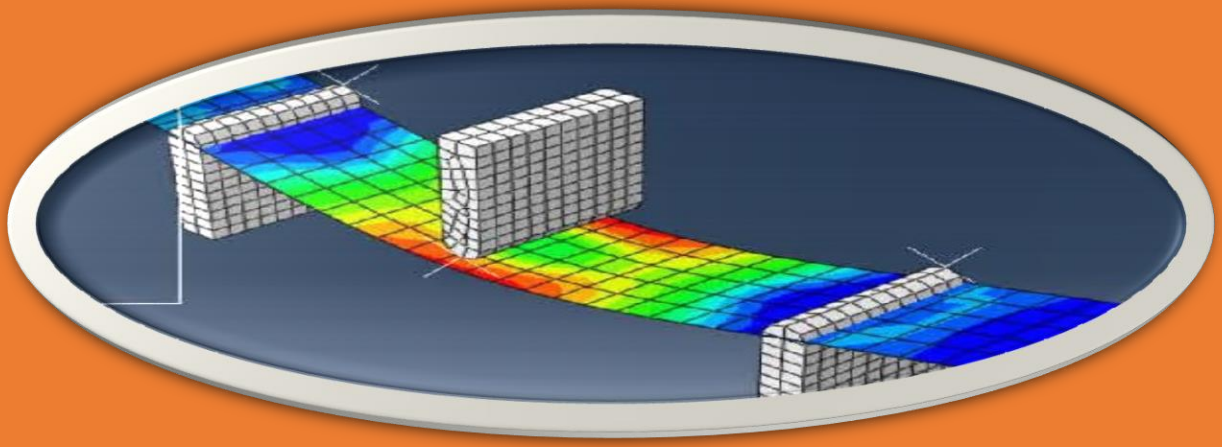

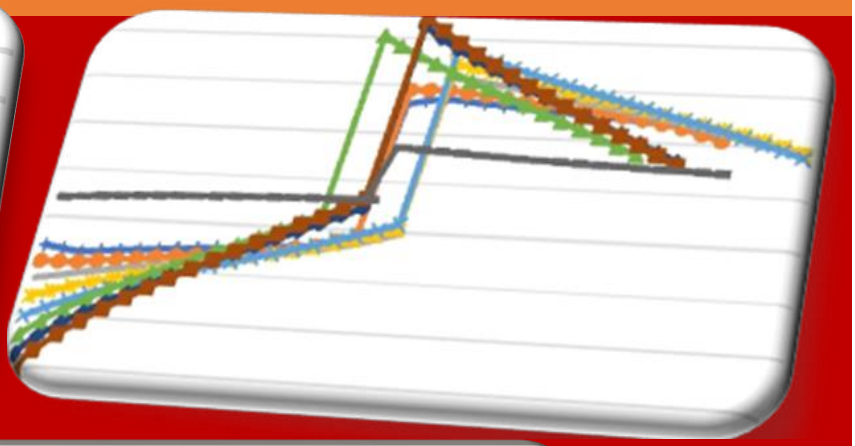

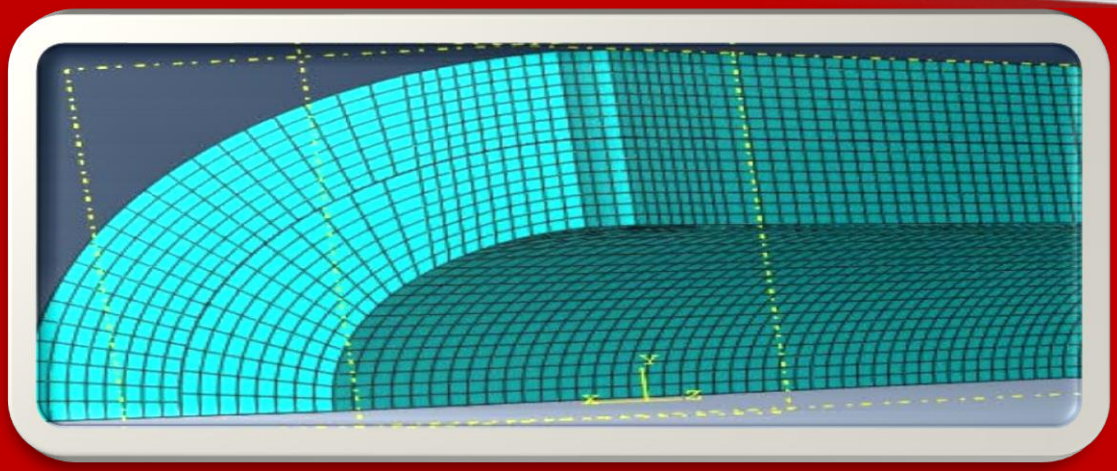

The Institution of Engineers of Kenya

ISSN: 2957- 7780

In partnership with

AJERI

African Journal of Engineering in Research and the Innovation

ISSN: 2957- 7780 Volume 1. No 1. 2023

Published by:

The *Institution of Engineers of Kenya*

P.O Box 41346- 00100
City Square Nairobi Kenya
Tel: +254 (20) 2729326, 0721 729363, (020) 2716922
Email: editor@iekenya.org
Website: www.iekenya.org

IEK

African Journal of Engineering Research and Innovation (AJERI), is published by **The *Institution of Engineers of Kenya,*** IEK, as an international forum for publication of high-quality papers in all areas of Engineering

CONTENTS **Pages**

EFFECTS OF RADIAL CIRCULAR CROSS BORE SIZE ON PRESSURE CARRYING ABILITY OF THICK COMPOUND CYLINDER

N. Kiplagat[1], L. M. Masu[2], and P. K. Nziu[3]

[1,3] Moi University, School of engineering, Department of Manufacturing Industrial & Textile Engineering, Eldoret, P. O. Box 3900 Eldoret, KENYA.

[2] Technical University of Kenya, Faculty of engineering and the built environment, School of Mechanical and manufacturing engineering, Department of Mechanical and Mechatronic Engineering, Haile Selassie Avenue, P.O. Box 52428, Nairobi, 00200, Tel +254(020) 343672, 2249974, 2251300, 341639, Nairobi, Kenya,

Corresponding Author: Naftali Kiplagat- nkipla@gmail.com; [2]L M Masu masulpm@gmail.com; [3]Patrick Nziu- pnziu@mu.ac.ke

Publication Date: March 2023

ABSTRACT:

In design of pressure vessels, the effect of stress concentration caused by geometric discontinuities because of provision of supports and openings for manholes, gauges, etc., has to be considered. These openings have the geometric features like size, shape, location, obliquity, and shrinkage pressure that affect the Stress Concentration Factor (SCF) in pressure vessels. The purpose of this research work was to establish the radial circular cross bore size in a thick compound cylinder that was optimal and generated the least (SCF). After analyzing 8 different circular cross bore size ratios that ranged from 0.1 up to 0.8, at the radial position, it was established that with increased cross bore size of the compound cylinder, there was a corresponding increase of the magnitude of the hoop stress. Hence, the cross-bore compound cylinder that had the lowest cross bore size ratio of 0.1 generated the smallest hoop stress and gave a minimum SCF of 3.02. Whereas the highest hoop stress was developed at the cross-size ratio of 0.8 with an SCF magnitude of 6.75. The minimum magnitude of SCF translates to a decrease of the pressure carrying ability of the compound cylinder by 67% compared to a similar plain compound cylinder.

Keywords: Compound Cylinder, Cross Bore Size, Stress Concentration Factor, Finite Element Analysis

1.0 INTRODUCTION

Cylinders can be constructed in such a way that they may hold fluids under pressure and are extensively used in nuclear and chemical plants, gas, and high-pressure vessels (Bahoum, Diany, and Mabrouki 2017). With the increased shortage of raw materials and the higher costs in the manufacture of pressure vessels, researchers have not allowed themselves to be confined to traditional elastic techniques. Researchers have however turned their interest to studies related to elastic as well as elasto-plastic techniques that offer greater economical use of materials. Therefore, some elastic-plastic techniques have been developed and designed to improve the pressure carrying capability of thick-walled cylinders (Majzoobi et al. 2004). These techniques involve autofrettage and the use of compound cylinders. This study focuses on compound cylinders which are usually manufactured when two or more cylinders (Bahoum et al. 2017) of different diameters with some interference are shrunk into each other. Therefore, this shrinking process generates residual hoop stresses in the walls of the compound cylinders and subsequently enhances the functioning of the pressure vessels against the working pressure (Kumaresan and Chocklingam 2018).

These pressure vessels can have holes often referred to as cross bores (Makulsawatudom, Mackenzie, and Hamilton 2004) and can be positioned diametrically hence referred to as a radial cross bore. These openings are used to provide for openings that are needed to fit instrumentation accessories for essential operations (P. K. Nziu and Masu 2019). Some of these accessories include temperature meters, safety, and relief valves, bursting discs, flow circuit meters, lubrication provisions (Kihiu and Masu 1995). The cross bore is a critical catalyst of a flaw in a pressure vessel because of the high-stress concentrations that appear in the presence of the cross bore (Masu and Craggs 1992). Therefore, this flaw causes geometric discontinuities that alter the stress distribution and create regions that are considered as areas of stress concentrations. Thus, the intensity of stress concentration initiated by an abrupt change of section can be expressed as a Stress Concentration Factor (SCF)(Kiplagat, Masu, and Nziu 2020). Moreover, the evaluation of this stress distribution in pressure vessels can be determined by experimentally (Kharat and Kulkarni 2013), analytically, or numerically (Dharmin, Khushbu, and Chetan 2012).

Stress concentration of cross-bored compound thick cylinders is dependent on some major design parameters which include and are not limited to cross bore shrinkage pressure, size, shape, location, and obliquity angle(Kiplagat et al. 2020). This study explores the significance of size as a configuration geometry in the design of compound cylinders with cross bores. Hence, to study the consequence of cross bore size on high-pressure vessels, the bore diameter to the side hole diameter (eq. 1) was used.

2.0. METHODOLOGY

2.1 Geometric Section

To analyze and check the influence of size on the stress concentrations on a compound thick cylinder, 8 different radial circular cross bore sizes were studied. The modeling process used a shrinkage pressure of 89.464 MPa and was exposed to an internal pressure of 1 MPa. The configuration of these cross-bores is tabulated in Table 2.1

Table 2.1 Circular cross bore diameters

Cross bore ratio, (K_s)	0.1	0.2	0.3	0.4	0.5	0.6	0.7	0.8
Cross bore diameter (mm)	0.01	0.02	0.03	0.04	0.05	0.06	0.07	0.08

The choice of the vessel is based on a commonly used size for compound cylinder design. The inner and outer sleeves had an inner and outer radius of 0.05 m and 0.075 m respectively. Further, the cross-bore radii were dependent on the cross-bore ratios. The configuration showing a radial cross bore is illustrated in Fig. 2.1.

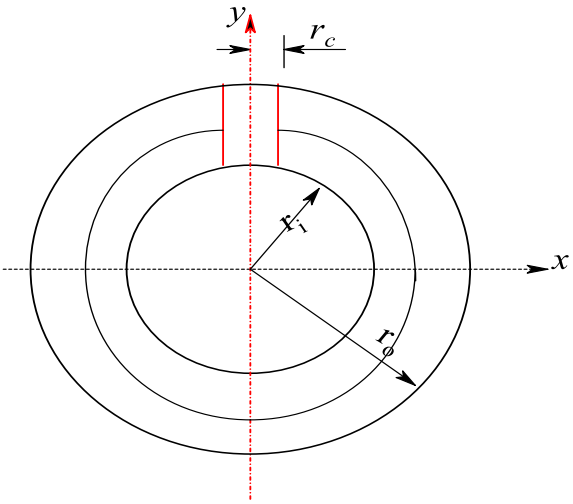

Fig. 2.1 Radial circular cross bore configuration

Where:

r_c cross bore radius (side hole)
r_i main bore inner radius
r_0 main bore outer radius

Using a commercial engineering software program called Abaqus, finite element modeling was done on the thick-compound cylinder having radial circular cross bores. Therefore, a total of 8 separate models were created and analyzed.

2.2 Finite Element Analysis (FEA)

A deformable three-dimensional solid was modeled by sketching and creating a quarter profile of such a compound cylinder. Hence, a solid body comprising of two cylinders i.e., the inner and outer sleeves were created. The depth of the thick-compound cylinder was extruded from the face of the model. Further, the depth of the thick compound cylinder was created to be three times the compound cylinder's outer diameter. Moreover, this was performed in order to limit the closed ends closure-effects of the compound cylinder from being transmitted to the other far part of the cylinder. The cut revolve technique was used and one of the models at this point and the resulting output is displayed in Fig. 2.2.

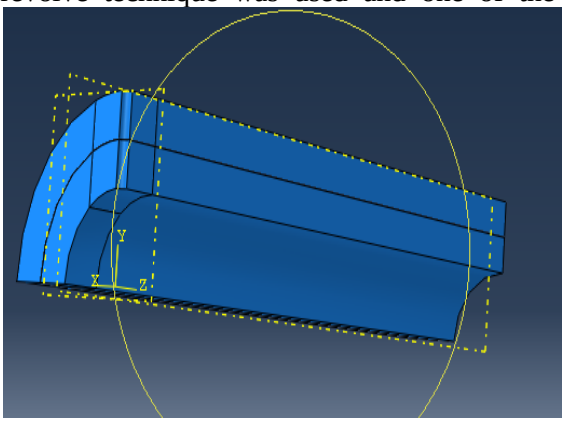

Fig. 2.2 Compound cylinder: Part profile: Cross Bore Ratio; 0.1

During the duration of this entire study, an elastic model made of steel was used, and it had the following material properties: Poisson's ratio of 0.29, Young's modulus of elasticity of 207 GPa, and a density of 7800kg/m^3. Consequently, the material selected was similar to the ones used in industrial compound pressure vessels (Amin, Rahman, and Ali 2014).

Both the inner and outer steel section properties were created and defined as both solid and homogeneous. Further, both the inner and outer sleeves were combined to be one assembly of a thick-walled compound cylinder. Hence, a single assembly of both instances which had independent mesh types of inner and outer sleeves was created. Usually, the single assembly contained each geometry in the created finite element model.

The evaluation used for this modeling was designed by creating two steps i.e., interference and pressure steps. The steps created in this module were useful during the loading module. Hence, the interference step was used during the analysis of the shrinkage pressure of both the inner and outer sleeves. While the pressure step was used for the analysis of the internal pressure of the compound cylinder. Thus, the interference and pressure steps were done separately, and their corresponding results were superimposed.

It is worthy to note that each analysis step was interlinked with the use of various types of boundary conditions (loads) created. Symmetrical boundary conditions were then employed in different planes of the created cylinder during the initial step and propagated through the interference and pressure steps. These boundary conditions were also in regions X, Y, and Z axes for both sleeves, hence stopping any rigid movement.

The model was then subjected to internal pressure to both the cross and main bores, while the shrinkage pressure was introduced at the interference fit of the inner and outer sleeves of the thick-walled compound cylinder. The application of pressure in the loading module was done in two stages, namely, the internal pressure for the whole model and that due to shrinkage (contact pressure). However, it is worth noting that, the internal pressure of 1 MPa was only applied in the pressure step that was created using the step manager module. Further, the shrinkage pressure of 89.464 MPa for both the inner and outer sleeves was only applied in the interference step and was made inactive in the pressure step. During the loading module, three models were subjected to different loads. First, the internal surface of the whole model was subjected to a positive internal pressure, hence causing tensile stresses. Secondly, the outer surface of the inner sleeve was subjected to a negative shrinkage pressure giving rise to compression, therefore, it was considered as negative. Finally, the inner surface of the outer sleeve was subjected to a positive shrinkage pressure as giving rise to tension, therefore, it was considered as positive.

The Abaqus software documentation procedures recommend the use of second-order tetrahedral and hexahedral elements when performing stress analysis. Therefore, second order C3D10 tetrahedral elements having 10 nodes were adopted in this study. Further, the C3D20R, a 20-node quadratic brick element, was used to reduce integration. In this study, cylinders with small cross bores used the hexahedral element while models with larger cross bores used the tetrahedral elements. The mesh density around the model was biased because of increasing the number of elements around specifically targeted zones. In the current study, this was done around the cross bore. Specifically, the meshed density varied between 0.003-0.004 m as used in a previous study by Nziu (2018). A sample of the model with a biased mesh density is shown in Fig.2.2.1. Hence, the capture of localized stress concentration was increased around the cross-bore region.

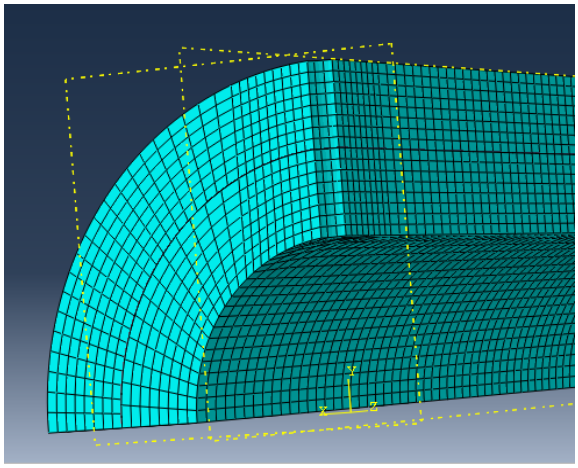

Fig 2.2.1 Biased meshed density

2.3 Model Validation

This study adopted the analytical method to validate the finite element model. Principal stresses generated by plain compound cylinders were analyzed and compared for validation using analytical and Finite Element Analysis (FEA) procedures. By comparing the FEA hoop stresses that were far away from the cross bore with their corresponding theoretical results, this study accomplished verification of the results (Mankar and Khodake 2015). Also, according to the Saint-Venant principle, stresses far-off from the cross bore should give results approximately equal to stresses of compound cylinders without cross bores (plain compound cylinders).

2.4 Hoop Stress Concentration factor

The current study described SCF as the ratio of the localized critical stresses in a cross-bore cylinder to the corresponding stresses in a similar plain cylinder without a cross bore. In the design of strength of materials and the practical application of engineering, it is worthwhile to mention that peak stresses play a key role in establishing the strength of materials. Also, fatigue failure and cracks are most likely initiated from the regions of high-stress concentration (Cole, Craggs, and Ficenec 1976). Therefore, in this study, the stress concentration factor (SCF) was analyzed based on the location with the highest value of hoop stress in the thick-walled compound cylinder for the respective different cross bore ratios (K_S).

3.0 RESULTS AND DISCUSSION

The impacts of radial circular cross-bore size on compound cylinders are discussed under the following subheadings.

3.1 Hoop stress distribution pattern along the transverse edge of radial circular cross bores having different sizes

A comparison was carried out between various thick-walled compound cylinders having distinct cross bore sizes caused by cross bore ratios of 0.1 to 0.8 and with a corresponding plain compound cylinder. Fig. 3.1 shows the effects of hoop stress on the length of the transverse edge of a cross bored thick-walled compound cylinder.

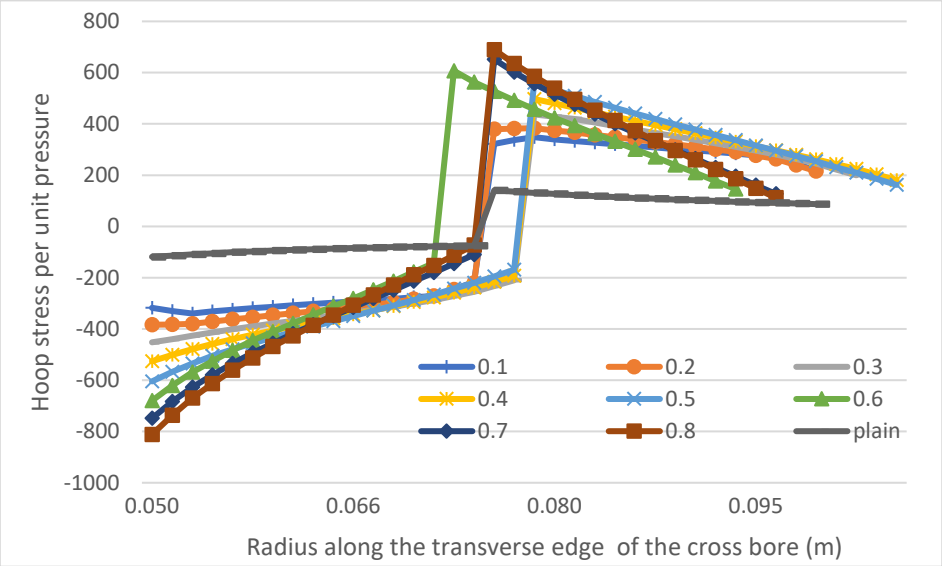

Fig. 3.1 Hoop stress vs cross bore radius

This comparative analysis observed the behavior of variation of the stress of the cross bored thick-walled compound cylinder in reference to the plain cylinder. A cross bore generated higher values of hoop stress when introduced to a cylinder at a specific point. The analysis showed that the maximum hoop stress of the cross bored thick-walled compound cylinders was all higher than the thick-walled plain compound cylinder.

3.2 Optimization of the radial circular cross bore

With the variation of cross bore size, the significance of the highest hoop stress in a thick-walled compound cylinder was noted when a circular radial cross bore was introduced. Therefore, the SCF was calculated based on the location of the maximum hoop stress in the thick-walled compound cylinder with the matching hoop stress of the plain thick-walled compound cylinder at the same location. Equation 1 was used to generate the SCFs, and hoop stresses determined and are analyzed under the following subsections:

3.2.1 Cross-bore size influences on the maximum hoop stress

Fig. 3.2.1 shows the changes in the amount of hoop stress as the cross-bore size increases.

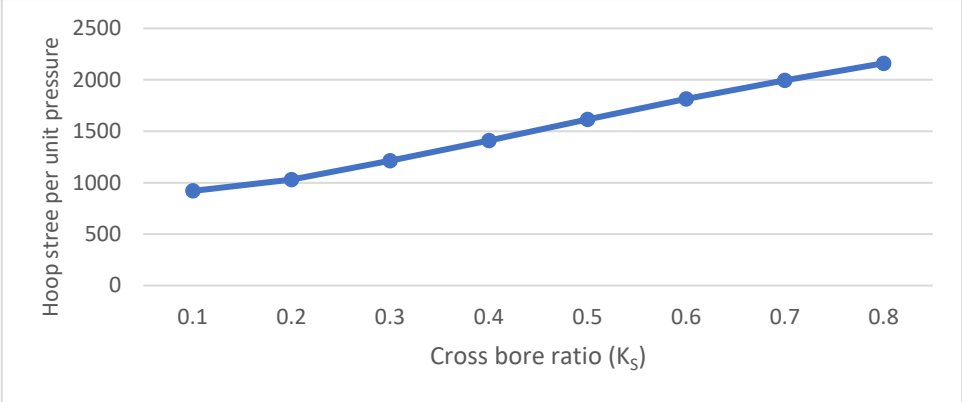

Fig. 3.2.1 Hoop stress vs cross bore size

As indicated in Fig. 5, it was noted that the maximum hoop stress increased as the cross-bore ratio increased. Thus, this translated to mean that as the cross-bore sizes increased the hoop stresses also increased. Therefore, the minimum hoop stress among all maximum hoop stresses of all cross-bore sizes was as a result of the cross-bore ratio of 0.1 with a magnitude of 920. This observation, therefore, means, that the smaller the cross-bore size the lower the hoop stress. The increase of hoop stress is monotonic, from a small cross bore to a large cross bore. For instance, the maximum hoop stresses per unit pressure for a cross bore ratio of 0.1 and 0.8 were 920 and 2161, respectively. This translated to a 135% increase in hoop stress magnitude. This occurrence can be related to the structural stiffness of the cross bore because less material is subjected to stresses as the cross-bore size increases. Thus, the rise in a cross-bore size led to a further reduction of the stiffness of the structure of the thick-walled compound cylinder hence leading to a rise of the hoop stress magnitudes.

3.2.1 Cross bore size effects on hoop stress concentration factor

The behavior of the hoop SCF on the several cross-bore sizes is illustrated in Fig. 3.2.2. The SCFs of the thick-walled compound cylinders with distinct cross bore sizes were computed in relation to the locations with the highest amounts of hoop stress in the compound cylinder.

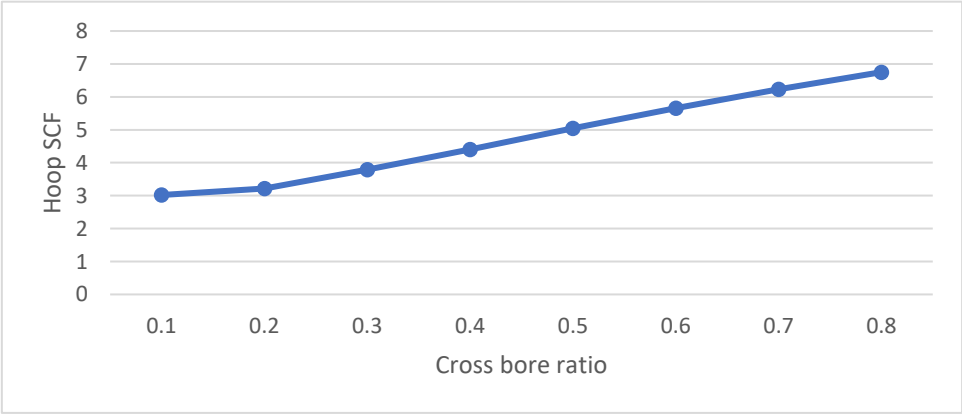

Fig. 3.2.2 Hoop stress concentration factor vs cross bore size

From Fig. 3.2.2, it is established that the increases in a cross-bore size contributed to the increased hoop SCF magnitudes. Noticeably, the cross-bore ratio of 0.1 generated the minimum hoop SCF in comparison to all the other studied cross bore ratios. Whereas a thick-walled compound cylinder having a cross bore ratio of 0.8 generated the highest hoop SCF of 6.74. This observation deduces that a thick-walled compound cylinder having a small cross bore ratio of 0.1 can withstand a pressure of up to twice its counterpart with a cross bore ratio of 0.8. Generally, it was deduced that cross bore ratio which means the cross-bore size influenced the hoop SCF. Thus, the growth in a cross-bore size led to the increase in the magnitude of the hoop stress concentration factor. Thus, this implies that the stiffness of the structure of the compound cylinder decreases with the growth of the cross-bore size hence triggering the creation of high hoop stresses and subsequently higher stress concentration factors.

In summary, an observation can be drawn that, a compound cylinder having a cross bore ratio of 0.1 generated the minimum hoop SCF as well as the lowest hoop stress per unit pressure. Usually, large cross bores involve the process of removing excess materials in the vessel, which results in only little material that will be subjected to load. Hence, when there are large quantities of material removal in a cross bore, there is an increased magnitude of the hoop stress which can lead to the failure of the thick-walled compound cylinder. The results are consistent with studies on the thick-walled cylinder by Nziu and Masu (2019b) where the authors concluded that for thick cylinders, the maximum hoop stress rises with an increase in a cross bore size.

4.0 CONCLUSION

During the entire study period, some conclusions were drawn. Firstly, it was noted that cross bore size affects the magnitude of hoop stress in a thick-walled compound cylinder. Secondly, after analyzing 8 different circular cross bore size ratios from 0.1 to 0.8, a radial position, the minimum cross bore size of 0.1 gave the least hoop stress and the minimum SCF of 3.02. While the highest stress was developed when the cross-size ratio was 0.8 with an SCF magnitude of 6.75. Further, from the 8 studied circular radial cross bores introduced to the thick-walled compound cylinder, the compound cylinder having a cross bore ratio of 0.1 generated the minimum SCF of 3.02 and hence considered as the optimum size. Finally, it can be noted that a thick-walled compound cylinder having a cross bore with a cross-ratio of 0.1 led to a decrease of the pressure carrying ability of the compound cylinder of 67% when compared to a similar plain thick-walled compound cylinder without a cross-bore

Authors' contributions

The manuscript was written through the contribution of all authors. All authors discussed the results, reviewed, and approved the final version of the manuscript.

Acknowledgment

This research work is supported by the Vaal University of Technology. The authors wish to thank the Department of Mechanical Engineering at the Vaal University of Technology for facilitating this work.

Conflict of Interest

The author(s) declare no potential conflicts of interest concerning the research, authorship, and publication of this article.

Funding

The author(s) received no financial support for the research, authorship, and publication of this article.

Data Availability Statements

The datasets generated and/or analyzed during the current study are available from the corresponding author on reasonable request.

Nomenclature

K_S	Cross bore ratio
SCF	Stress Concentration factor
FEA	Finite Element Analysis

REFERENCES

Amin, Md. Tanjin, Aminur Rahman, and Md Ali. 2014. "Optimum Design of Compound Pressure Vessel." *Global Journal Research Inc. (US)* 13:18–23.

Bahoum, Kaoutar, Mohammed Diany, and Mustapha Mabrouki. 2017. "Stress Analysis of Compound Cylinders Subjected to Thermo-Mechanical Loads." *Journal of Mechanical Science and Technology* 31(4):1805–11. doi: 10.1007/s12206-017-0328-5.

Cole, B. N., G. Craggs, and I. Ficenec. 1976. "Strength of Cylinders Containing Radial or Offset Cross-Bores." *J Mech Eng Sci* 18(6):279–86. doi: 10.1243/JMES_JOUR_1976_018_045_02.

Dharmin, Patel, Panchal Khushbu, and Jadav Chetan. 2012. "A Review on Stress Analysis of an Infinite Plate With." *International Journal of Scientific and Research Publications* 2(11):1–7.

Gerdeen, JC. 1971. "Analysis of Stress Concentrations in Thick Cylinders with Sideholes and Crossholes." *ASME Pap 71-WA/PVP-9 for Meeting* 94(3):815.

Hyder, M. Javed, and M. Asif. 2008. "Optimization of Location and Size of Opening in a Pressure Vessel Cylinder Using ANSYS." *Engineering Failure Analysis* 15(1):1–19. doi: https://doi.org/10.1016/j.engfailanal.2007.01.002.

Kharat, Avinash, and VV Kulkarni. 2013. "Stress Concentration at Openings in Pressure Vessels–A Review." *Int. j. Innov. Res. Sci. Eng. Technol.* 2(3):670–78.

Kihiu, JM, and LM Masu. 1995. "The Effect of Chamfer and Size on the Stress Distributions in a Thick-Walled Cylinder with a Cross Bore under Internal Pressure." *Jomo Kenyatta University of Agriculture and Technology. Digital Repository* 2(February):73–78.

Kiplagat, Naftali, Leonard Masu, and Patrick Nziu. 2020. "Effects of Geometric Stress Concentration in the Design of Thick Compound Cylinders- A Review." *International Journal of Engineering Research and Technology* 13:2255. doi: 10.37624/IJERT/13.9.2020.2255-2268.

Kumaresan, M., and Chocklingam. 2018. "Stress Analysis in Compound Cylinder and Autofrettaged Cylinders." *International Journal of Engineering Research and Technology* 7(4).

Majzoobi, G. H., G. H. Farrahi, M. K. Pipelzadeh, and K. Akbari. 2004. "Experimental and Finite Element Prediction of Bursting Pressure in Compound Cylinders." *International Journal of Pressure Vessels and Piping* 81(12):889–96. doi: https://doi.org/10.1016/j.ijpvp.2004.06.011.

Makulsawatudom, P., D. Mackenzie, and R. Hamilton. 2004. "Stress Concentration at Crossholes in Thick Cylindrical Vessels." *The Journal of Strain Analysis for Engineering Design* 39(5):471–81. doi: 10.1243/0309324041896506.

MANKAR, D., and P. KHODAKE. 2015. "Residual Stress Produced After Machining In Mechanical Components And Its Effects On Fatigue Life: A State Of Art." *International Journal of Mechanical and Production Engineering Research and Development (IJMPERD)* 5:1–10.

Masu, L. M. 1997. "Cross Bore Configuration and Size Effects on the Stress Distribution in Thick-Walled Cylinders." *International Journal of Pressure Vessels and Piping* 72(2):171–76. doi: https://doi.org/10.1016/S0308-0161(97)00026-4.

Masu, L. M., and G. Craggs. 1992. "Fatigue Strength of Thick-Walled Cylinders Containing Cross Bores with Blending Features." *Proceedings of the Institution of Mechanical Engineers, Part C: Journal of Mechanical Engineering Science* 206(5):299–309. doi: 10.1243/PIME_PROC_1992_206_132_02.

Nziu, P. K. 2018. "Optimal Geometric Configuration of a Cross Bore in High Pressure Vessels. In Doctorate Thesis." Vaal University of Technology.

Nziu, P. K., and L. M. Masu. 2019. "Cross Bore Size and Wall Thickness Effects on Elastic Pressurised Thick Cylinders." *International Journal of Mechanical and Materials Engineering* 14(1):4. doi: 10.1186/s40712-019-0100-y.

Nziu, P., and L. Masu. 2019. "Elastic Strength of High Pressure Vessels with a Radial Circular Cross Bore." *International Journal of Mechanical and Production Engineering Research and Development* 9:1275–84. doi: 10.24247/ijmperdjun20191

EMISSIONS OF VEHICULAR TRAFFIC ALONG UHURU HIGHWAY CORRIDOR IN NAIROBI

J. K. Kenneth[1], S. K. Mwea[2], George.M[3]

[123]Department of Civil and Construction Engineering, University of Nairobi

Publication Date: March 2023

ABSTRACT:

Rapid urbanization and economic growth has consequently led to steady increase in vehicular traffic in cities and Nairobi is not an exceptional. Vehicular emissions have been extensively reported to correlate strongly with the level of urban air pollution and this research paper basically confirms the fact. Uhuru Highway Corridor is a road segment of the northern corridor (A8) in Nairobi City. It is one of the busiest and congestion-prone highways in Nairobi covering approximately 3.7 kilometers spanning between Lusaka roundabout and the museum hill interchange. The study investigated the urban ambient air pollutants levels correlation with vehicular emissions which included Carbon monoxide, (CO), Nitrogen dioxide (NOx), Sulphur dioxide (SOx), Total volatile organic compounds (TVOC), Hydrocarbons (HCHO) and Particulate matter of diameter 2.5 microns (PM2.5). A systematic study which measured CO, NOx, SOx, PM2.5, HCHO and TVOC in ambient air at two different stations, near Railway Underpass (NRU 01) and University of Nairobi Pedestrian Tunnel (UNPT 02) was done having variations in traffic flows and meteorology. Traffic flow was assessed with prevailing levels of emissions and the association of these air pollutants among each other. PM2.5. HCHO, SOx, CO and TVOC, all decreased with decrease in vehicle Volume. However, NOx which increased with decrease in vehicle. The ambient vehicular pollutions for the corridor were within the limits of World health organization (WHO) standards of ($10mg/m^3$) with an exception on PM2.5 which was found to be $18.39mg/m^3$ and $18.56mg/m^3$ for stations NRU 01 and UNPT 02 respectively, CO values were 3.72ppm for NRU 01 and 3.76ppm for UNPT 02, SOx for the two stations NRU 01 and UNPT 02 were 0.37ppm. Volatile Organic Compounds (TVOC) for the stations were highest at NRU 01 at 0.36ppm and least at UNPT 02 at 0.32ppm. Nitrogen dioxide (NO_2) was least at UNPT 02 at 0.32ppm and highest at NRU 01 at 0.50ppm. Sulphur dioxide (SO_2) was 0.37ppm for the two stations NRU 01 and UNPT 02. To enhance Government of Kenya air quality legislation, the vehicle allowed into the country must comply with the Kenya Bureau of Standards requirements of Legal Notice No. 78 of 15th July 2005 (Verification of Conformity to Kenya Standards Imports Order, 2005) and KS1515:2000 Kenya Standard Code of Practice for Inspection of Road Vehicles. In Particular, the Imported Vehicle; must be less than 8 years old from the year of first registration and should be subjected to roadworthiness inspection by a KEBS appointed inspection agent in the country of export. The Nairobi Express way is a major strategy and innovation that when effectively utilized would reduce vehicular emissions in the City, a study is recommended to verify emissions along the corridor after the commission of the express way.

Keywords: Traffic Emissions, Particulate Matter, Hydrocarbons, Carbon Monoxide, Sulphur Dioxide, Total Volatile Organic Compounds

1.0 INTRODUCTION AND STUDY AREA

The study focused on Uhuru Highway Corridor, a road segment of the northern corridor, one of the most highly travelled and congestion-prone roadway in Nairobi County the capital City of Kenya situated 140 kilometers South of equator and 500 kilometers West of the Indian Ocean at 1°17′S 36°49′E and UTM Northing 9857083.2891357.Nairobi City occupies 696 km^2 at an altitude of 1,661 meters above sea level (Nairobi County website, 2016 www.nairobi.go.ke/home/about-the-county). Plate 1.1 shows the location of Nairobi County and the study area

Plate 1.1: Map of Uhuru Highway corridor the study area

Existing information on data collection techniques and sample size were reviewed. Traffic data survey was conducted at the two identified sites within the study area, the first site was identified as NRU 01 road side near Nairobi Railways underpass and second site as UNPT 02 near the University of Nairobi pedestrian tunnel. The peak and off-peak hours of motorized traffic counts were considered from 11^{th} to 16^{th}, November 2019. Further to enable development of trends on vehicular traffic and emissions over time during the days of the week, a fifteen-minute time interval throughout the survey period (6:00 am to 6:00 am) was adopted. This would give a variability representation across small time interval as the recommended best practice.

2.0 METHODS OF DATA COLLECTION

2.1. Introduction

Existing information on data collection techniques and sample size were reviewed. Traffic data survey was conducted at the two identified sites within the study area, the first site was identified as NRU 01 road side near Nairobi railways underpass and second site as UNPT 02 near the University of Nairobi pedestrian tunnel. The peak (6:00am to 10:00am and 4:00pm to 8:00pm) and off-peak (10:00am to 4:00pm) hours of motorized traffic counts were considered from 11th to 16th, November 2019. Further to enable development of trends on vehicular traffic and emissions over time during the days of the week, a fifteen-minute time interval throughout the survey period (6:00 am to 6:00 am) was adopted. This would give a variability representation across small time interval as the recommended best practice.

2.2. Measurement of Emissions

The data was collected averagely every 15 minutes' using various gas analyzers with meteorological parameters measured by an automated weather observing stations. Three measuring equipment were used at a height of 2 meters away from the road at approximately 2 meters height. They included: Bosean for determination of NOx, SO_2, CO and Dienmaern for determination of PM2.5, HCHO and TVOC.

Wind speed and wind direction were of great importance during the emissions determination taking the readings at every station averaging readings after 15 minutes period. The ambient air emissions were determined for a period of 6 days (from 11th to 16th of November 2019) for 24 hours' period from 6:00 am to 6:00 am alongside vehicle traffic volumes by types. Table 3.1 presents the details of the field measurements and information of the monitoring sites

Table 3.1: Monitoring Sites and Details of the Measurement Program

Measurement Station	Station Code	Station Characteristics	Details of field measurement			
			Air quality	Meteorology	Traffic survey	Duration of study
Near Nairobi railways underpass	NRU 01	Higher traffic volume	CO, NOx, HC, TVOC, PM 2.5, SOx	Wind speed, wind direction	Car, bus, taxi, bike.	11-16 November, 2019
Near the University of Nairobi pedestrian Tunnel	UNPT 02	Higher traffic volume	CO, NOx, HC, TVOC, PM 2.5, SOx	Wind speed, wind direction	Car, bus, taxi, bike.	11-16 November, 2019

Table 3.2: Geometric Characteristics of the Uhuru Highway Corridor

ID	Road section	Road type	Number of lanes	Section length Approximation (m)	Average lane width (m)	Average side walk width (m)
1	Grade separated interchange at the Museum Hill intersection to University Way	Arterial	6	500	3.50	2.0
2	University Way to Kenyatta Avenue	Arterial	6	500	3.50	2.0
3	Kenyatta Avenue to Haile Selassie Avenue	Arterial	6	500	3.50	2.0
4	Haile Selassie Avenue to Bunyala road	Arterial	6	500	3.50	2.0

2.3. Traffic Data Survey

2.3.1 Traffic Classification-Motorized

Motorized Traffic (MT) count was manually done for the study classifying them into Motorcyle Private Cars, Jeeps / 4WD's/utility vehicle, pickup/vans, Matatus (9 - 25 seats), Small buses, Large Bus (>27 passengers), Light Trucks 2 axles (single rear wheel), Medium Trucks (2 axles, Double rear wheels), Heavy Trucks (3, 4 axle), Artics/Draw - bar Trucks (>4 axles) and other (Agricultural tractors, grader).

2.3.2 Volume of Traffic Recorded by Vehicle Classification

Traffic was first categorized into eleven types for convenience of the study according to their respective Passenger car units (PCU) factor. Traffic counting was done using the tally sheets which was found to be simplest and least expensive data collection tool. For easy analysis, data was collected for the desired 15 minutes time intervals for 24 hours and converted into PCU, a method in which various vehicle characteristics and types in equivalent standard unit where one car was considered one unit, multiplying the traffic data with respective PCU factor for the individual vehicle type.

3.0 RESULTS, ANALYSIS AND DISCUSSION

3.1 Introduction

Traffic characterization (volume by time) and traffic emissions level (significant parameters and variation by time) relationship are illustrated in this section.

3.1.1 Traffic Composition

Traffic composition along Uhuru Highway Corridor at Station NRU 01 was presented in Figure 4.1 Typically, cars, pick-ups and vans comprise the largest type of vehicles with an average of 57%, Matatus at 15%, small and large buses at 17%, trucks at 4% and motorcycle 7%.

The traffic composition seen from the two survey stations NRU 01 and UNPT 02 in Figures 4.1 and 4.2 gives an indication that government should have a policy to reduce the number of small vehicle which comprises 51% to 57% of the vehicle volume along the corridor from accessing the CBD and to encourage public transportation, introduction of Bus Rapid Transport (BRT) system, staggering working hours, and restraining parking spaces.

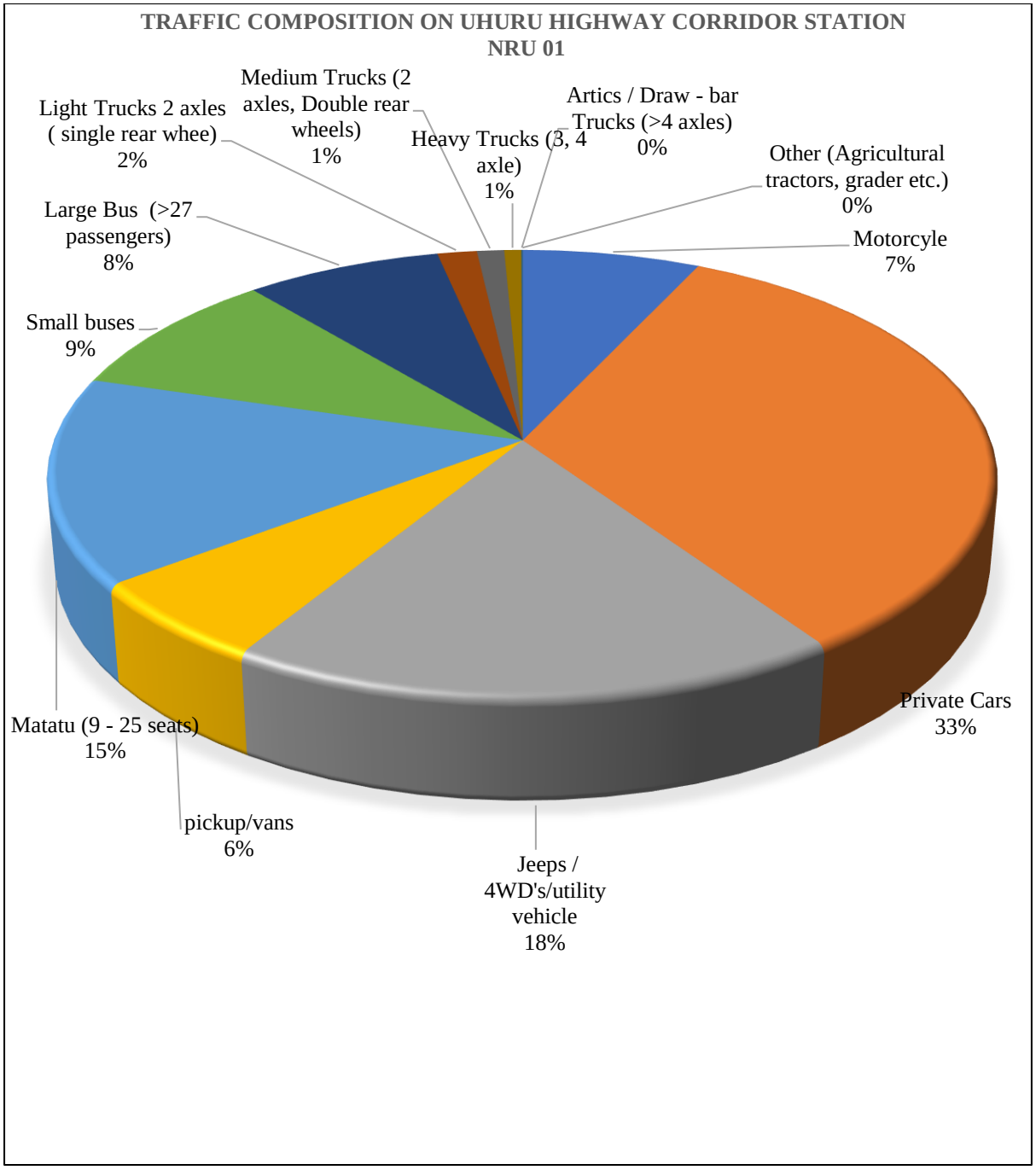

Figure 4.1: Traffic Composition on Uhuru Highway Corridor Station - NRU 01

Traffic composition along Uhuru Highway Corridor at station UNPT 02 was also presented in Figure 4.2. Cars had 48%, pick-ups and vans comprised 20%, motorcycle 15%, Matatus, trucks small and large buses at 17%.

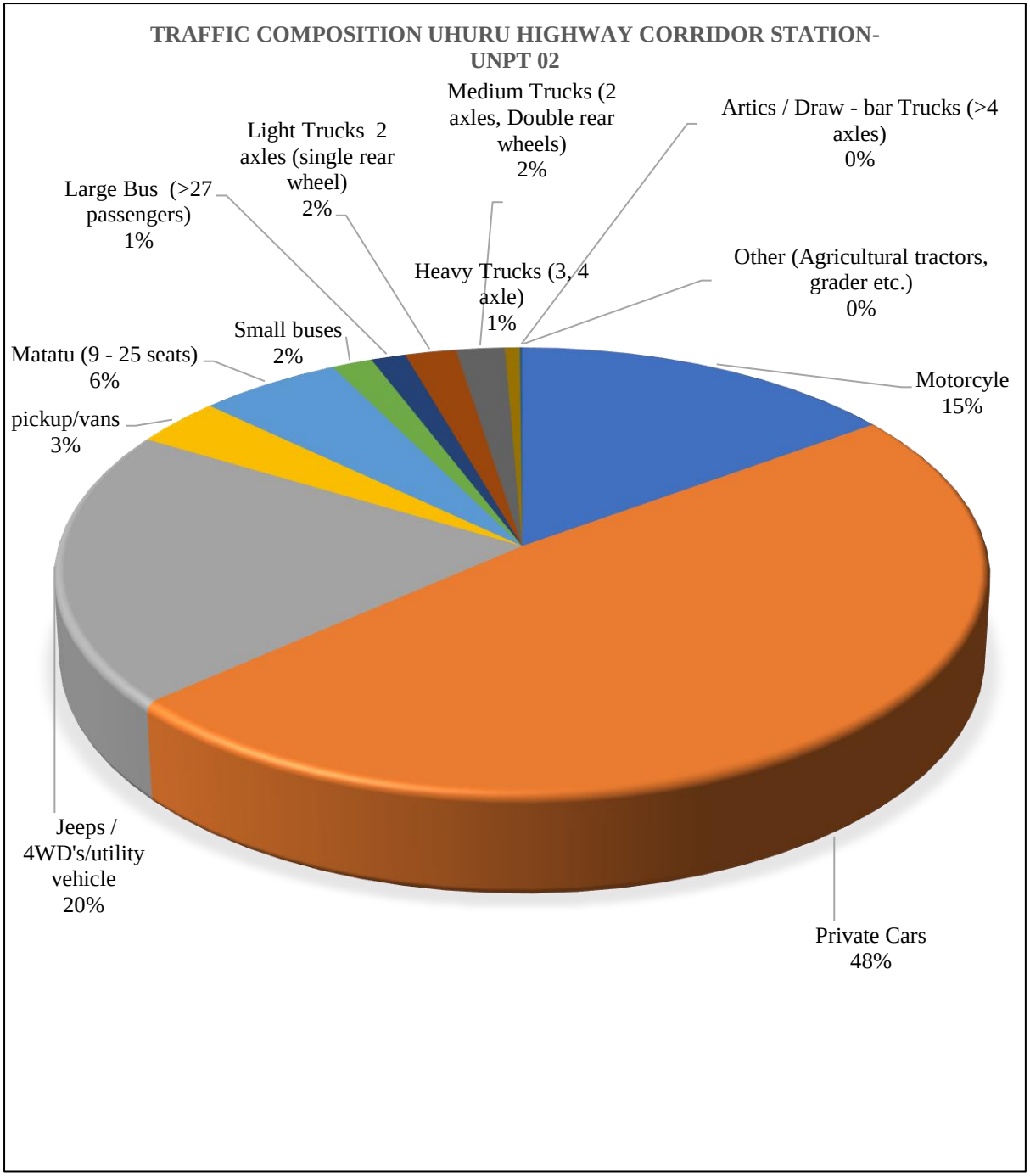

Figure 4.2: Traffic Composition on Uhuru Highway Corridor Station UNPT 02

The Figures 4.3 to 4.14 show the 24 hours' Traffic Volumes Variations while Figures 4.15 and 4.16 show the one-week traffic volume variations for the two stations NRU 01 and UNPT 02 respectively.

The 24 Hours' Traffic Volume Variations sampled are presented in Figures 4.3 to Figure 4.14

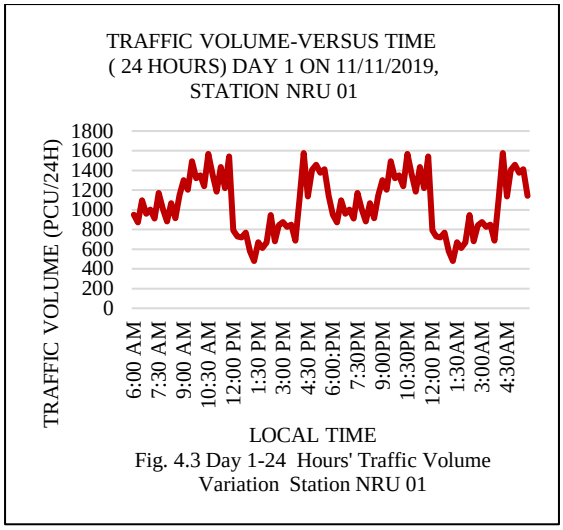

Fig. 4.3 Day 1-24 Hours' Traffic Volume Variation Station NRU 01

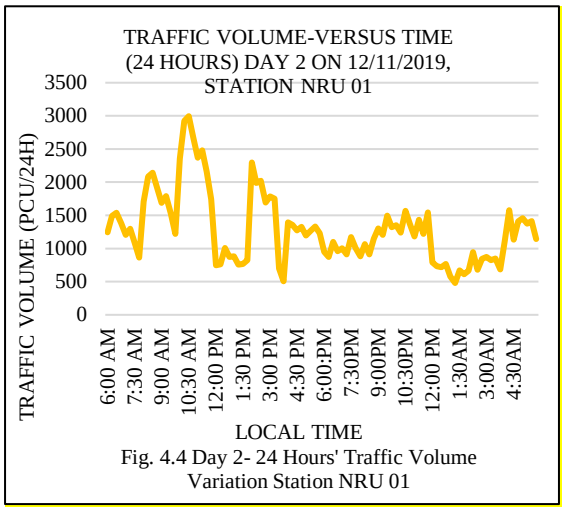

Fig. 4.4 Day 2- 24 Hours' Traffic Volume Variation Station NRU 01

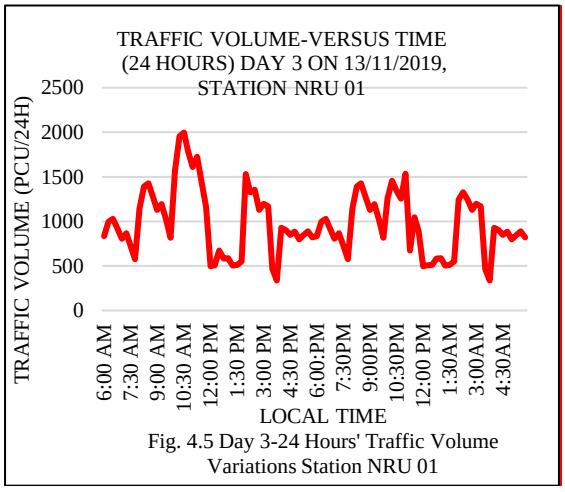

Fig. 4.5 Day 3-24 Hours' Traffic Volume Variations Station NRU 01

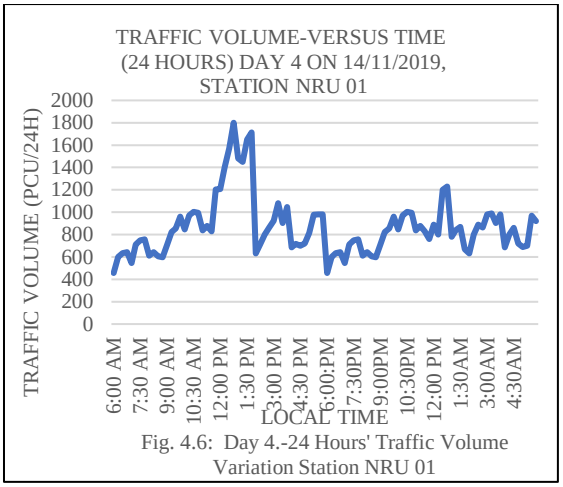

Fig. 4.6: Day 4.-24 Hours' Traffic Volume Variation Station NRU 01

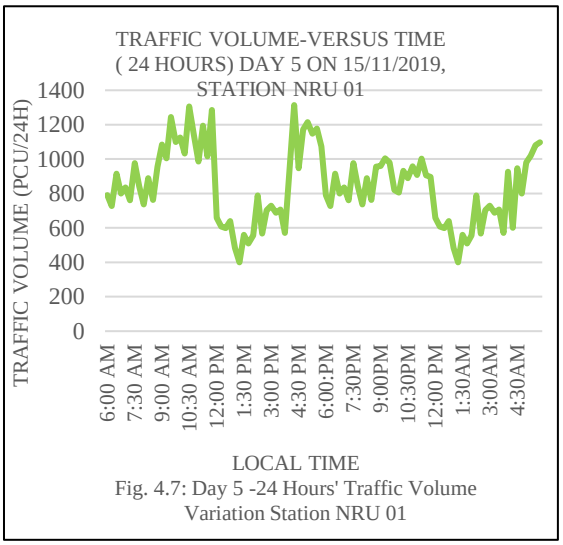

Fig. 4.7: Day 5 -24 Hours' Traffic Volume Variation Station NRU 01

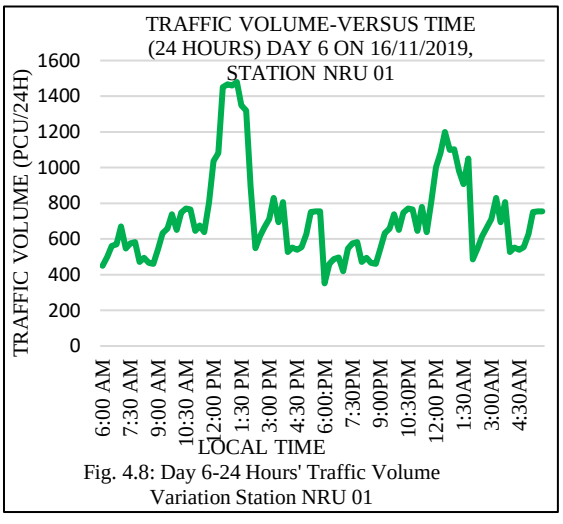

Fig. 4.8: Day 6-24 Hours' Traffic Volume Variation Station NRU 01

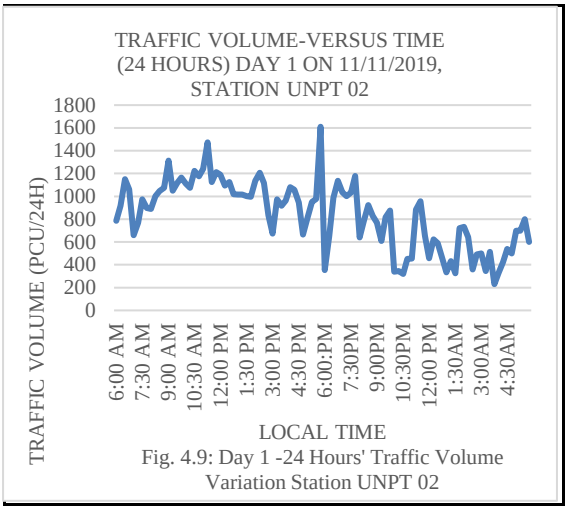

Fig. 4.9: Day 1 -24 Hours' Traffic Volume Variation Station UNPT 02

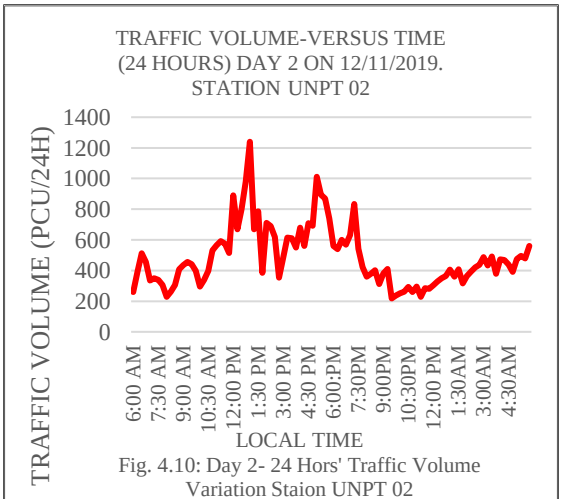

Fig. 4.10: Day 2- 24 Hors' Traffic Volume Variation Staion UNPT 02

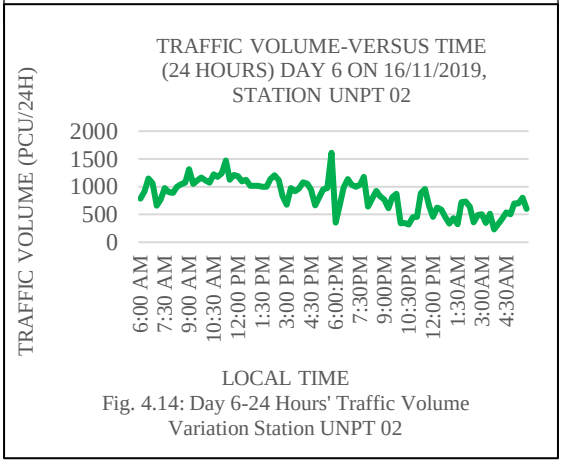

Fig. 4.14: Day 6-24 Hours' Traffic Volume Variation Station UNPT 02

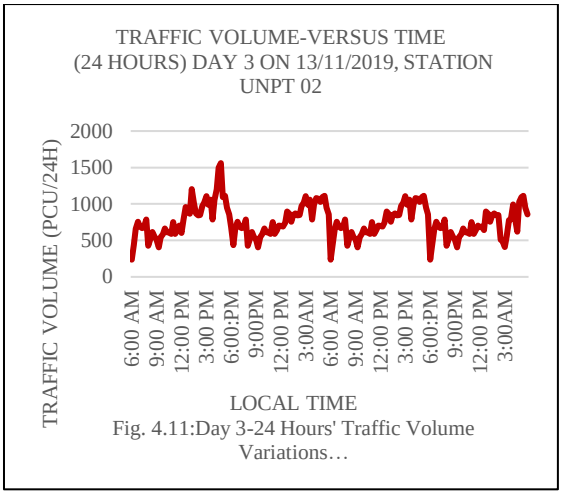

Fig. 4.11:Day 3-24 Hours' Traffic Volume Variations…

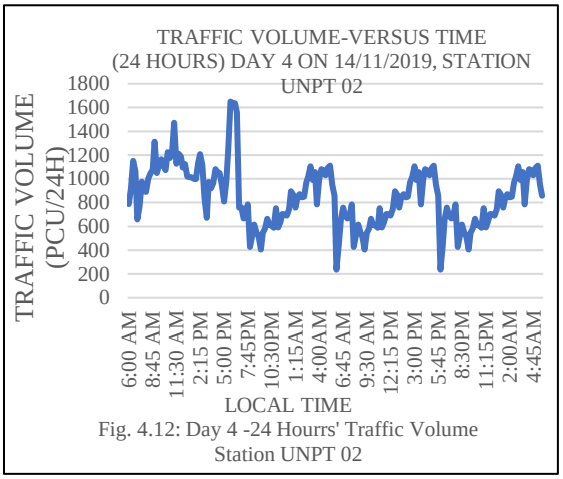

Fig. 4.12: Day 4 -24 Hourrs' Traffic Volume Station UNPT 02

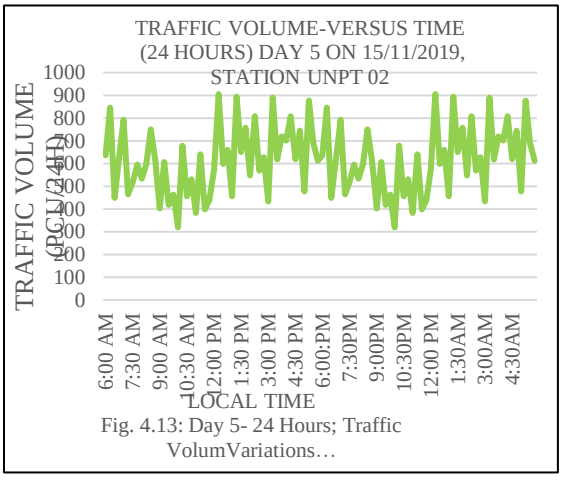

Fig. 4.13: Day 5- 24 Hours; Traffic VolumVariations…

The Figures 4.17 to 4.32 show the 24 hours' diurnal variations of emissions and particulate matter PM2.5 for the two stations NRU 01 and UNPT 02 respectively

3.1.2 Diurnal Variations of Emissions and Particulate Matter PM2.5

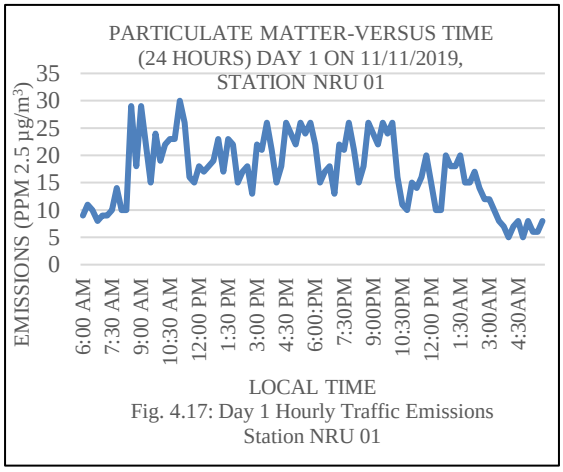

Fig. 4.17: Day 1 Hourly Traffic Emissions Station NRU 01

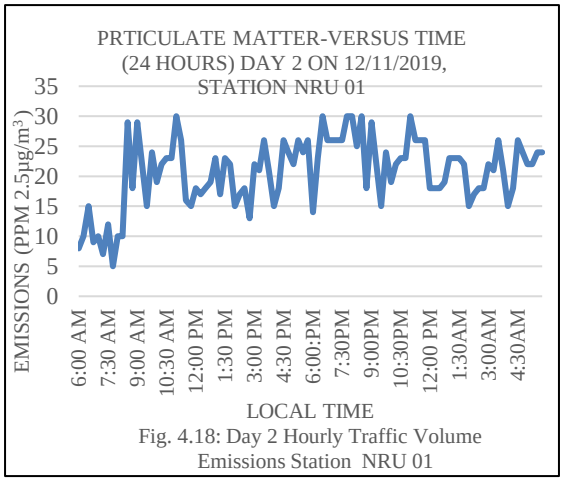

Fig. 4.18: Day 2 Hourly Traffic Volume Emissions Station NRU 01

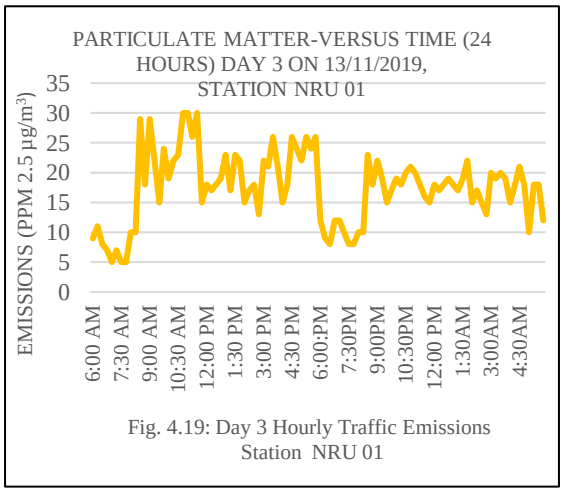

Fig. 4.19: Day 3 Hourly Traffic Emissions Station NRU 01

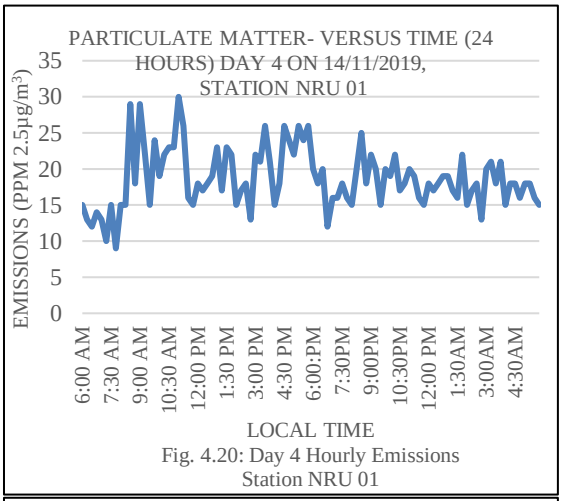

Fig. 4.20: Day 4 Hourly Emissions Station NRU 01

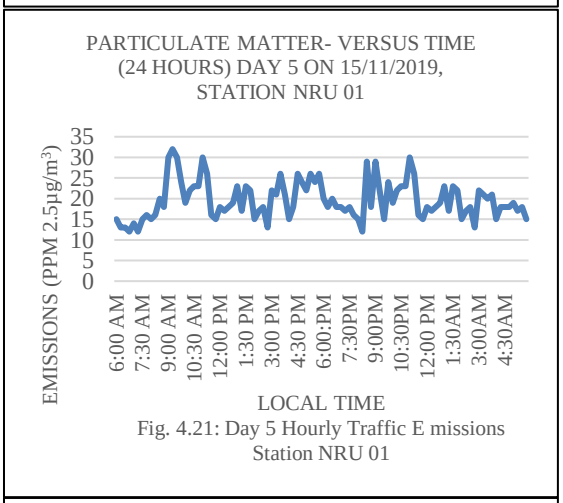

Fig. 4.21: Day 5 Hourly Traffic E missions Station NRU 01

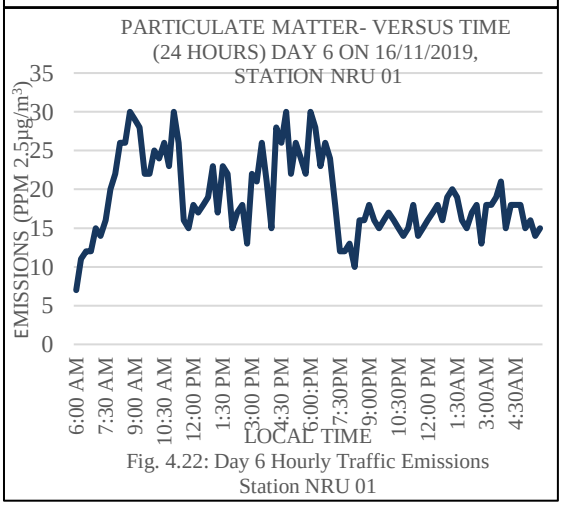

Fig. 4.22: Day 6 Hourly Traffic Emissions Station NRU 01

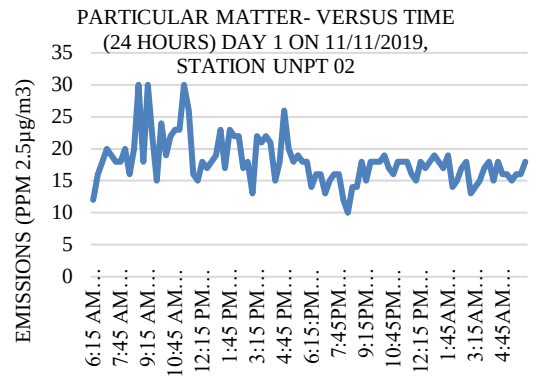

Fig. 4.23: Day 1 Hourly Traffic Emissions
Station UNPT 02

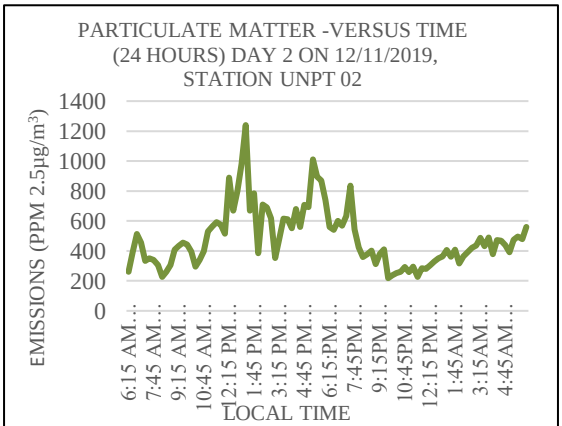

Fig. 4.24; Day 2 Hourly Traffic Emissions
Station UNPT 02

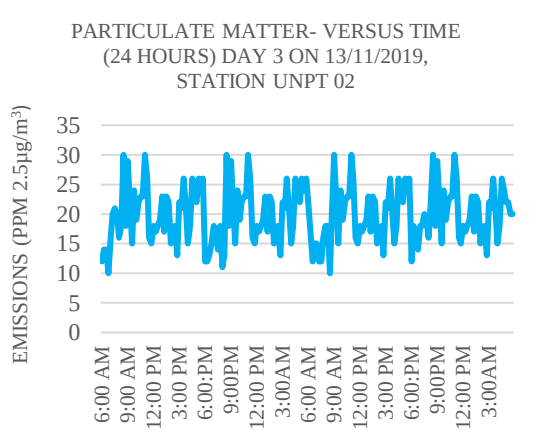

Fig. 4.25 Day 3 Hourly Emission
Station UNPT 02

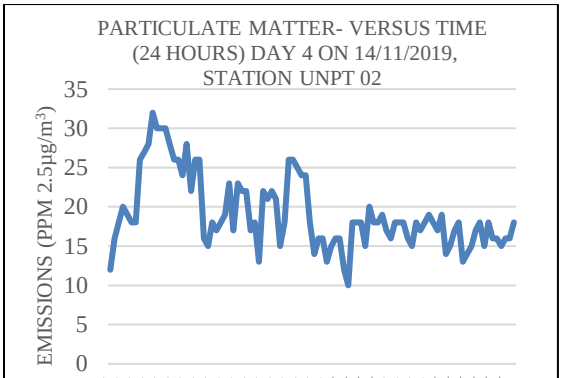

Fig. 4.26: Day 4 Hourly Traffic Emissions
Station UNTP 02

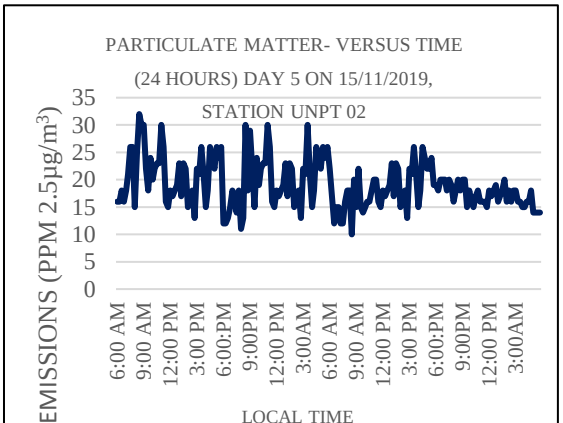

Fig. 4.27: Day 5 Hourly Traffic E missions
Station UNPT 02

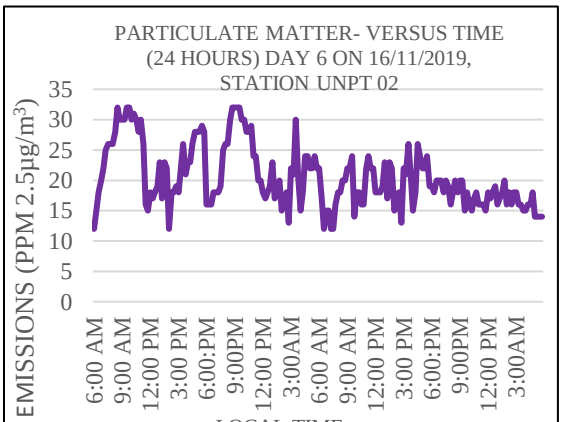

Fig. 4.28 ;Day 6 Hourly Emissions
Station UNPT 02

3.2 Analysis of Trends of Daily Traffic Volumes-Versus Emissions

Traffic volume data for both direction of travel for the two stations NRU 01 and UNPT 02 were plotted against Emissions to obtain trends for comparison.

3.2.1 A summary of Traffic Emissions for Nairobi Uhuru Highway Corridor for the two stations NRU 01 and UNPT 02

Table 4.5 and 4.6 presents in summary the results of ambient emissions of CO, SO_2, NOx, HCHO, TVOC, and PM2.5 at two measuring sites namely road side near Nairobi railways underpass NRU 01 and near the University of Nairobi pedestrian tunnel UNPT 02. On the basis of 15 minutes measured observations the lowest value of PM2.5 at NRU 01 site was at 18.39µg/m^3 and the highest being UNPT 02 site at 18.56µg/m^3 which were found to be above the tolerable level of 10mg/$m^3$of WHO. It was additionally found that CO values were 3.72ppm for NRU 01 and 3.76ppm for UNPT 02. SOx for the two sites NRU 01 and UNPT 02 was 0.37ppm. Volatile Organic Compounds (TVOC) for the sites were highest at NRU 01 at 0.36ppm and least at UNPT 02 at 0.32ppm. Nitrogen dioxide (NO_2) was least at UNPT 02 at 0.32ppm and highest at NRU 01 at 0.50 ppm.Sulfur dioxide (SO_2) was 0.37ppm for the two sites NRU 01 and UNPT 02

Table 4.5: Peaks of Air Quality PM2.5 (Particulate Matter Levels)

Sampling Location	**Dust Concentration Levels PM2.5 (Mg/m^3)**	**Tolerable Levels PM2.5 (Mg/m^3)**	**Remarks**
Near railways underpass Station NRU 01	18.39	10	Above the Limit
University of Nairobi pedestrian tunnel Station UNPT 02	18.56	10	Above the Limit

Table 4.6: Peaks of Air Quality (Emission Level)

Location	**Carbon Monoxide (CO)**	**Sulphur Dioxide (SO_2)ppm**	**Volatile Organic Compounds (TVOC)**	**Nitrogen Dioxide (NO_2)ppm**
Station NRU 01	3.72	0.37	0.36	0.50
Station UNPT 02	3.76	0.37	0.32	0.32
TLV	10ppm	0.125mg/m^3	70ppm	0.150mg/m^3
Comments	Within the limit	Above the limit	Within the limit	Above the limit

3.3 Discussions

From the obtained results at the two sites of data collection, there was an indication of an average values of pollution. It can be deduced that the site NRU 01, had the lowest value of ADT 69783 followed by, UNPT 02 with ADT 60479. The high levels of PM2.5, NOx and SOx measured for the NRU 01 and UNPT 02 could

be attributed to the high traffic volume with reduced speeds of 26 Kph leading to high ambient air pollutants. PM10 and PM2.5 often derive from different emissions sources, and also have different chemical compositions. Emissions from combustion of gasoline, oil and diesel fuel produce much of the PM2.5 pollution found in outdoor air while PM10 includes dust from construction sites, landfills, and wind-blown dust from open lands. It is therefore clear that the PM2.5 was from vehicle emissions considered in this research paper and not PM10 from heavy construction and reduced green spaces within the corridor.

Higher values of SOx and NOx emissions occurs only by the Sulphur burning compounds, which could be identified as diesel-driven vehicles and thus, the overall amounts of SOx and NOx emission were relatively less as compared to Carbon Monoxide although above the tolerable WHO guideline limits.

3.3.1 Comparison of Emissions with WHO Guidelines

The results analyzed for stations NRU 01 and UNPT 02 were within the limits of WHO standards for ambient emissions for CO 10ppm, TVOC 70ppm but above the limits for SOx 0.125mg/m^3, NOx 0.150mg/m^3 and PM2.5ppm of 10mg/m^3. · (WHO 2012) Diesel Engine Exhausted Carcigenic in Cancer IAIRO (Ed), World Health Organization). Tables 4.5 and 4.6 shown that CO values for the two stations were 3.72ppm and 3.76ppm for stations NRU 01 and UNPT 02 respectively, SOx 0,37ppm, TVOC 0.36ppm and 0.32ppm and NOx 0.50ppm and 0.32ppm. Particulate matter PM2.5 were 18.39ppm and 18.56ppm respectively.

3.3.2 Recommendations for adoption by the industry

The government should develop measures to reduce emissions such as pollution control from source by improving vehicle design and maintenance, patronage of public transportation system, alternatives means of transportation, staggering working hours to reduce the number of vehicles and traffic congestions, restraining parking areas within the central business districts, stopping engines from running during traffic congestions, construction of ring roads and by-passes to reduce traffic congestion in towns and legislative enactment of pollutant emissions.

3.3.3 Effect of Wind Speed and Wind Direction on Pollutants

Generally, the variability of pollutant concentration levels strongly depends on the origin of the air masses arriving at the sampling site and the concentration of pollutants in the ambient air influenced by the direction from which wind blows. During this study, the wind direction was predominantly from east to west with an average speed of 3m/s, a control survey station was set away from the road side with same wind speed of 3m/s which gave very low values of emission, this was a clear indication that the readings taken 2m away from the carriage way and approximately 2 meters above the ground levels were predominantly vehicular emissions. The Table 4.7 shows the average weather parameters in 24 hours during the data collection period for the stations NRU 01 and UNPT 02 sampling stations.

Table 4.7: Average Weather Parameters in 24 Hours

Parameters	Wind speed (m/s)	Temperature (°C)
Station NRU 01	3.566	18.3
Station UNPT 02	2.365	22.21

4.5 Correlation of Traffic Volume with CO, NO_X. SO_X, PM2.5, HCHO and TVOC for Stations NRU 01 and UNPT 02

As described in section 3 the traffic flow showed a significant influence on the emissions and particulate matter. The observations were made in ambient air at the two stations NRU 01 and UNPT 02. In the correlation analysis, all the six pollutants concentrations and their corresponding traffic numbers were considered. The Table 4.8 and Figures 4.35 to

4.47 show the Correlation Matrix for NRU 01 and UNPT 02 Sites. These Correlations were significant for all parameters analyzed for the two Sites raging between R^2(0.766-0.861) for Linear Trend Lines and R^2(0.817-0.984) for Curvilinear Trend Line. Linear Correlations (R^2) were less than the Curvilinear (R^2) Correlations as illustrated on Table 4.8 and therefore the Curvilinear Trend lines had the best values.

Table 4.8: Comparison of Traffic Volume and Emissions Correlation Matrix-Linear and Curvilinear Tread Lines for the Stations NRU 01 and UNPT 02

	Linear Trend Lines (R^2) Station NRU 01	**Linear Trend Lines (R^2) Station UNPT 02**	**Curvilinear Trend Lines (R^2) Station NRU 01**	**Curvilinear Trend Lines (R^2) Station UNPT 02**
CO	0.850	0.835	0.851	0.855
NOx	0.766	0.823	0.837	0.823
SOx	0.817	0.836	0.817	0.836
PM2.5	0.843	0.851	0.946	0.851
HCHO	0.803	0.836	0.916	0.836
TVOC	0.827	0.841	0.870	0.851

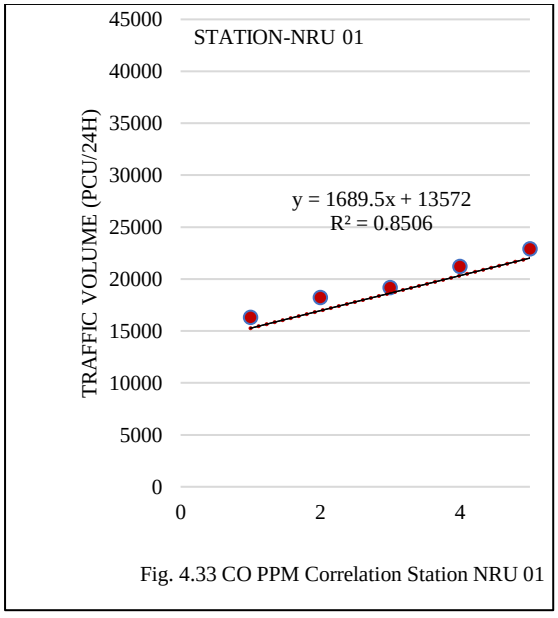

Fig. 4.33 CO PPM Correlation Station NRU 01

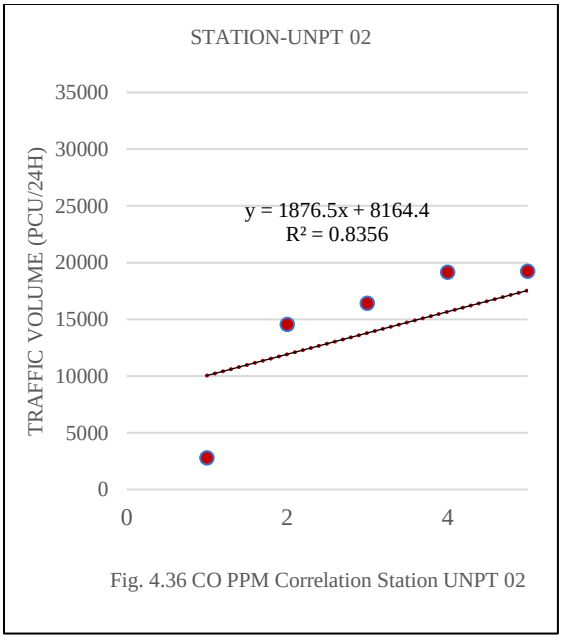

Fig. 4.36 CO PPM Correlation Station UNPT 02

Analysis of Carbon Monoxide (CO)

For Carbon monoxide in Figures 4.35 and 4.36, both equations showed positive constant values which are nearly parallel. The reasons could be CO was emitted mainly by the petrol run vehicle, as a form of unburnt fuel. The number of light vehicles, which were the leading emitter of CO, were more than heavy vehicles and hence CO values were higher, in comparison to others

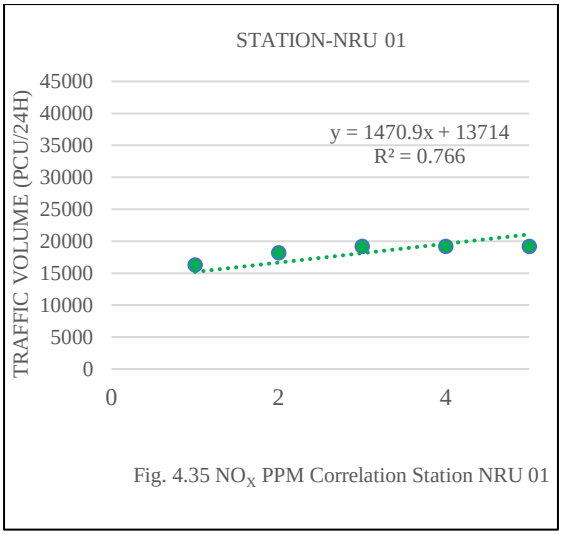

Fig. 4.35 NO_X PPM Correlation Station NRU 01

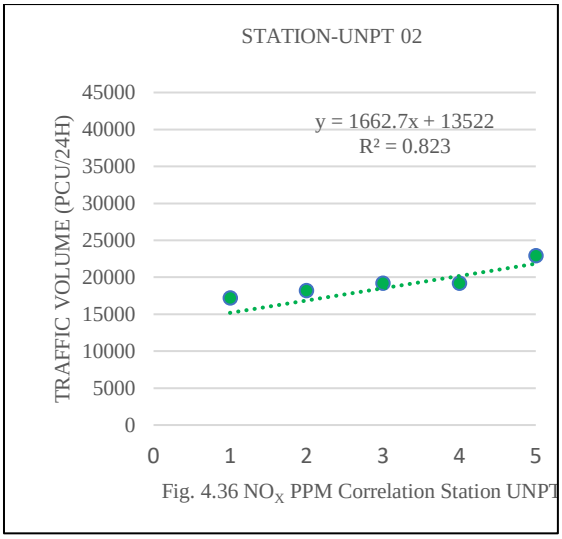

Fig. 4.36 NO_X PPM Correlation Station UNPT

Analysis of Nitrogen Oxide (NOx)

For Carbon Nitrogen Oxide Figures 4.37 and 4.38, both equations showed positive constant values which are nearly parallel. Only heavy vehicles, which could be identified as diesel-driven vehicles, emit NOx, and thus, the overall amounts of NOx emission were relatively less as compared to Carbon Monoxide

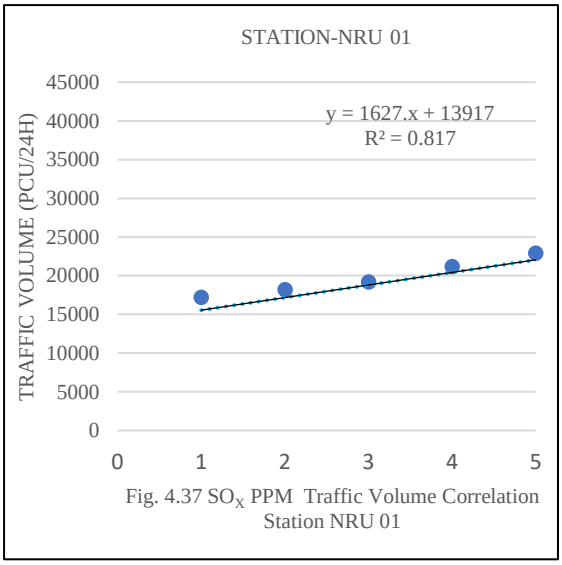

Fig. 4.37 SO_X PPM Traffic Volume Correlation Station NRU 01

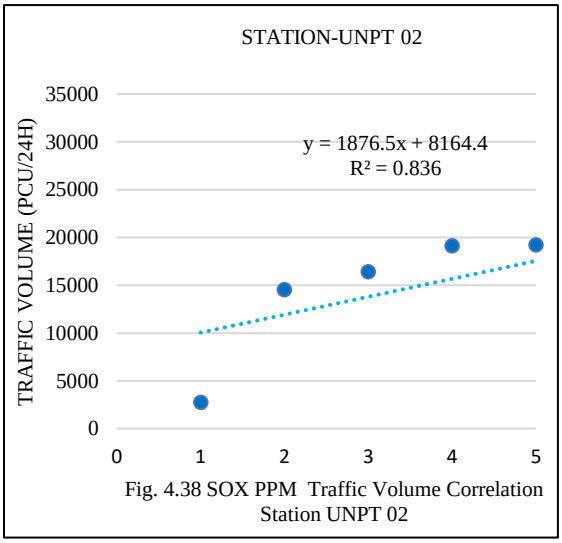

Fig. 4.38 SOX PPM Traffic Volume Correlation Station UNPT 02

Analysis of Sulphur Oxide (SOx)

For Sulphur Oxide Figures 4.39 and 4.40, both equations showed positive constant higher values, the reason could be SOx Emissions occurs only by the Sulphur burning compounds, which could be identified as diesel-driven vehicles.

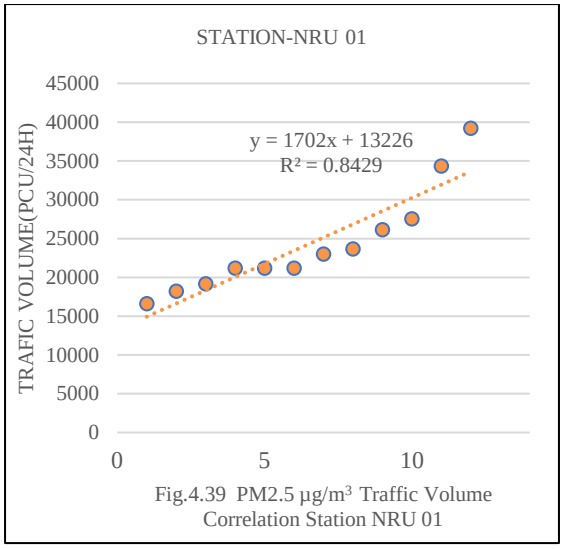

Fig.4.39 PM2.5 µg/m³ Traffic Volume Correlation Station NRU 01

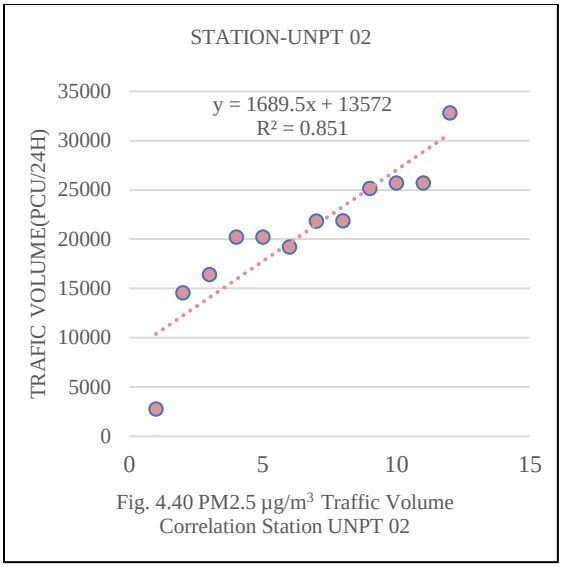

Fig. 4.40 PM2.5 µg/m³ Traffic Volume Correlation Station UNPT 02

Analysis of Particulate Matter (PM2.5)

For Particulate Matter (PM2.5) Figures 4.41 and 4.42, both equations showed positive constant higher values which are nearly parallel. Correlations between (PM2.5) were strong, positive, and significant.

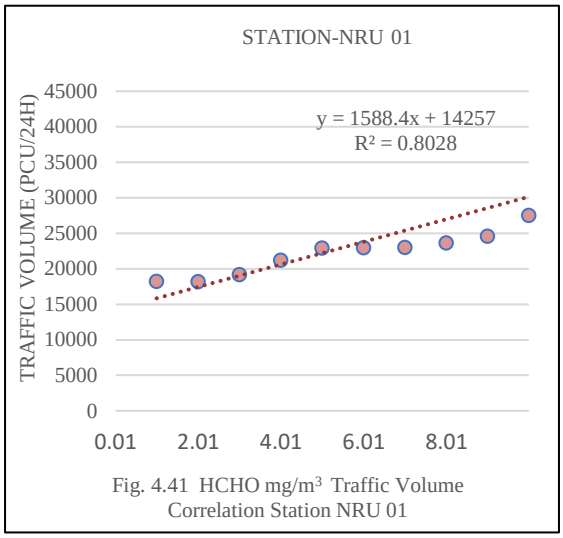

Fig. 4.41 HCHO mg/m³ Traffic Volume Correlation Station NRU 01

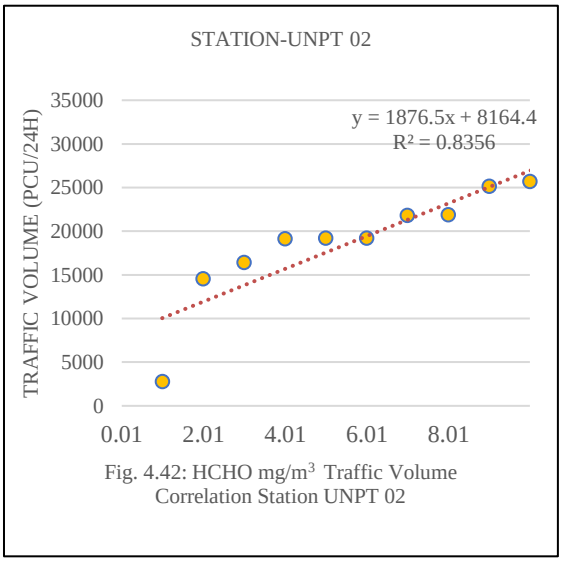

Fig. 4.42: HCHO mg/m³ Traffic Volume Correlation Station UNPT 02

Analysis of Hydrocarbons (HCHO)

For Hydrocarbons (HCHO) Figures 4.43 and 4.44, both equations showed positive constant higher values which were nearly parallel, HCHO is mostly emitted by petrol driven vehicles than diesel driven vehicles which were more dominant, however **(**HCHO) remained almost the same as CO emissions.

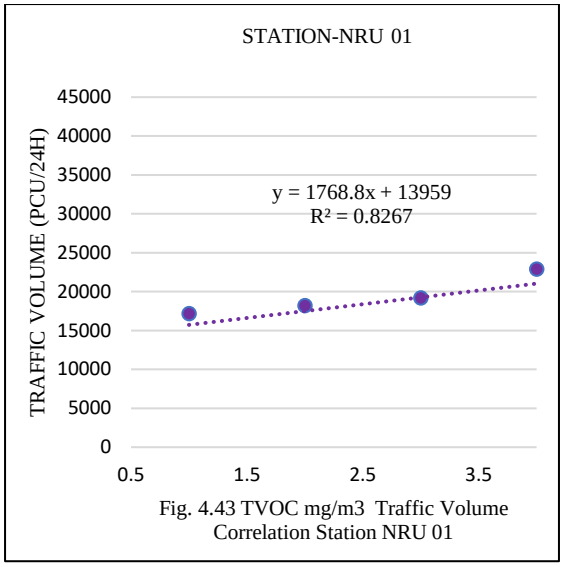

Fig. 4.43 TVOC mg/m3 Traffic Volume Correlation Station NRU 01

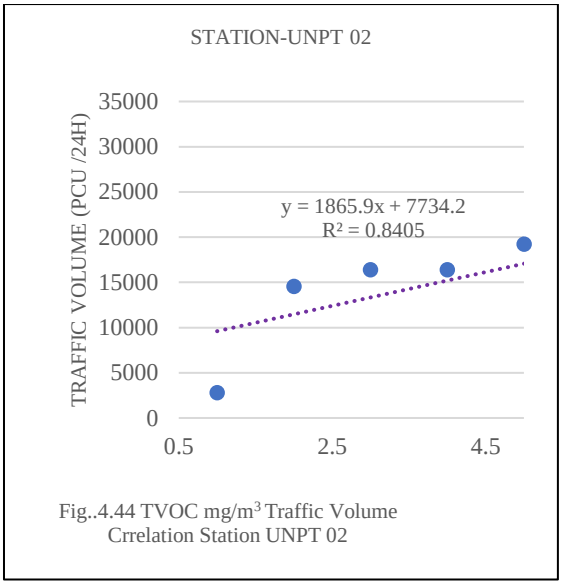

Fig..4.44 TVOC mg/m^3 Traffic Volume Crrelation Station UNPT 02

Analysis of Total Volatile Organic Compounds (TVOC)

For particulate matter (TVOC) Figures 4.45 and 4.46, both equations showed positive higher constant values, the reason could be that Total Volatile Organic Compounds (TVOC). Emissions occur only by the Sulfur burning compounds, which could be identified as diesel-driven vehicles; these were less in comparison to light vehicles.

4.0 CONCLUSIONS AND RECOMMENDATIONS

4.1 Conclusions

The concentrations of pollutants and emissions were attributed to vehicular volumes, sharp graphs were recorded during morning and evening rush high volumes and spread graphs during reduced traffic volumes, mostly afternoons and late hours during the nights.

The trends determined that, the ambient vehicular pollutions within Uhuru Highway Corridor (A8) (NRU 01 and UNPT 02) depended on the vehicle Volume. PM2.5. HCHO, SOx, NOx. CO and TVOC, all decreased with decrease in vehicle volume.

These Correlations were significant suggesting the strong association between vehicular volumes and emissions for all parameters analyzed for the two Sites raging between R^2(0.766-0.861) for Linear Trend Lines and R^2(0.817-0.984) for Curvilinear Trend Line.

The ambient vehicular pollutions for the corridor were within the limits of WHO standards of (10mg/m^3) with an exception on PM2.5 which was found to be 18.39mg/m^3 and 18.56mg/m^3 for stations NRU 01 and UNPT 02 respectively. The diurnal mean of SOx over the two sites were above the WHO limit with the highest amount recorded at 0.37ppm for NRU 01 and UNPT 02 respectively. The mean 24-hour amount of CO in all the sites was above the background concentration of between 0.05-0.12ppm NRU 01 recording the highest amount at 1.73ppm.

The concentrations of pollutants and emissions were attributed to vehicular volumes, sharp graphs were recorded during morning and evening rush high volumes and spread graphs during reduced traffic volumes, mostly afternoons and late hours during the nights.

Nairobi City in Kenya just like Atlanta the capital and most populous City in U.S. state of Georgia, serves as the cultural and economic center of the Nairobi metropolitan area, traffic volume within the corridor increased with reduction in speed which lead to further traffic

air pollutions, the National government and the County government of Nairobi should develop measures to reduce emissions such as pollution control from source by improving vehicle design and maintenance, patronage of public transportation system, alternative means of transportation, staggering working hours to reduce the number of vehicles and traffic congestions, restraining parking areas within the central business districts, stopping engines from running during traffic congestions, construction of ring roads and by-passes to reduce traffic congestion in towns and legislative enactment of pollutant emissions

.

5.0 REFERENCES

Australian Road Research Board (2002) *"Road & transport Research"* Volume11. Published by Australian Road Research Board, Limited University of Michigan.

Behera S. N. and Balasubramanian R., (2016), "*The Air Quality Influences of Vehicular Traffic Emissions."* DOI: 10.5772/64692.

Bennett C. and Paterson B. (2019*), "A Guide to Calibration and Adaptation" HDM-MM 4 Manual,* Volume-5. HDM Global publications.

Bickel, P., and R. Friedrich (eds.) (2005), "*ExternE-Externalities of Energy*: *Methodology 2005 Update."* Directorate-General for Research Sustainable Energy Systems. Published by European Communities, Luxemburg. ISBN: 92-79-00423-9.

Carslaw D. C., & Glyn Rhys Tyler (2013), "*New insights from comprehensive on-road measurements of NOx, NO_2 and NH_3 from vehicle emission remote sensing in London, UK.*" Published Atmospheric Environment Volume 81, Pages 339-347 https://doi.org/10.1016/j.atmosenv.2013.09.026

Chapman, L., (2007) "*Transport and climate change:"* a review. Journal of Transport Geography, 15(5), Pages 354 - 367. https://doi.org/10.1016/j.jtrangeo.2006.11.008

COWI A/S, Otieno Odongo & Partners Consulting Engineers, & QUTEP Limited (2012) "*Traffic Volume along Uhuru Highway Corridor*".

Walsh M. P., (2001) European Conference of Ministers of Transport, *"Vehicle Emission Reductions, Volume 425"* Published by OECD Publishing, the University of Michigan. Page 2-132. ISBN 9282113639, 978928211363.

Faiz A., Sinha K., Walsh M. & Varma A., (1990), "*Automotive Air Pollution: Issues and Options for Developing Countries*." Policy Research Working Paper Series 492. Published by The World Bank.

Friedrich R. and Bickel P. (2001), "*Environmental External Costs of Transport*." Springer Science & Business Media. Springer-Verlag, Berlin Heidelberg, Germany. Pages 11-30; 35-85.

Friedrich, R. and Bickel, P. (2005) "*PM2.5 has been proved to cause mortality and morbidity, both acute (short-term) and chronic (long-term)."*

Government of Kenya (1987), "Kenya: *National State of the Environment Report Vol 2,"* Kenya Ministry of Environment and National Resources supported by the United Nations Environment Programme. Pages 17-73 https://wedocs.unep.org/handle/20.500.11822/29794

Government of Kenya (2022), "*Design Manual for Urban Roads and Streets (DMRURS) 2019 (Low Res)"* Ministry of Transport, Infrastructure, Housing, Urban Development and Public Works. Revised Edition. https://africa.itdp.org/wp-content/uploads/2020/06/Street-Design-

Manual-for-Urban-Areas-in-Kenya-220225.pdf

Haneen K., Mark N., Zietsman J., Ramani T., (2020) "Traffic-Related Air Pollution" Published by

Elsevier Science, pages 45-325. ISBN 0128181222, 9780128181225

Mensink C., Kallos G., (2018) "Air Pollution Modeling and its Application XXV" Springer International

Publishing, Pages 114-501; ISBN 978-3-319-57644-2. DOI 10.1007/978-3-31957645-9.

Mock P., (2019) "*On the finishing line - The German automobile manufacturers in the context of the*

European CO_2 specifications for 2017" International Council *on* Clean Transportation.

Mortier R. Y., Fox M. F., Orszulik S. T., (2011), "*Chemistry and Technology of Lubricants*" Published by

Springer Dordrecht Heidelberg, 3rd Edition Page 295. ISBN 978-1-4020-8661-8. DOI 10.1023/b105569.

Mukaria S.M., Thenya T., Raphael G., Wahome and Karatu K., (2017) *"Analysis and Perception of Health*

Impact of Motor Vehicle Emissions on Traffic Police in Nairobi, Kenya." Journal of Environment Pollution and Human Health*;* Volume 5 (3): Pages 104-110. DOI: 10.12691/jephh5-3-5.

Nairobi City County Government - NCCG, (2014). "*Integrated Urban Development Master Plan for the*

City of Nairobi." https://www.kpda.or.ke/nairobi-integrated-urban-development-master-plan

Nairobi City County Government –NCCG, (2018), "*Air Quality Action Plan (2019-2023)*" Supported by

United National Environment Programme in partnership with Environmental Compliance Institute.

Nippon Koei Co., Ltd, (2014). *"The Project on Integrated Development Master Plan for City of Nairobi*

Republic of Kenya," Technical Support from Japan International Cooperation Agency (JICA).

Pan Chan, (2010*), "Performance Rating System of Sustainable Transport."* University of Waterloo.

Puckett, S.M., Noel, G.J., Jackson, L., Marjoncu, E., Razo, M., & Reed, E.M. (2015). "*Congestion Mitigation and Air Quality (CMAQ) Improvement Program: Cost-Effectiveness Tables Development and Methodology*" Published by Environmental Science for Transportation Research Board

Richardson A. J., Ampt E. S. and Meyburg A. H. (1995), "*Survey Methods for Transport Planning*",

Eucalyptus Press: Melbourne. Pages 271-388; 407-489 ISBN 064621439X, 9780646214399.

Robert K., Fred T., Schroeder J. (2015) "*Assessing Roadway Traffic Count Duration and Frequency*

Impacts on Annual Average Daily Traffic Estimation: Assessing Accuracy Issues Related to Short-Term Count Durations" U.S. Department of Transportation Federal Highway Administration. Pages 2-45

https://www.fhwa.dot.gov/policyinformation/travel_monitoring/pubs/aadt/aadt_task_3_final_report_nov_2015.pdf

Samson M.M, Thuita T, Raphael G.W.Kiemo K, Michael G.Analysis and Perception of Health Impact of

Motor Vehicle Emissions on Traffic Police in Nairobi, Kenya. *Journal of Environment Pollution and Human Health*, 2017, Vol 5, No3, 104-110.

Schindlbacher S., Tista M., Gager M., Haider S., Moosmann L., Kampel E. and European Environment

Agency (2013), "*European Union (EU) emission inventory report 1990-2011 under the UNECE Convention on Long - range Trans-Boundary Air Pollution (LRTAP)".* Published by the European Environment Agency, ISBN 9292134000, 9789292134006. Pages 14-96; 110-125.

Sehlstedt M., Annelie F., Behndig, Christoffer B., Blomberg A., Sandström T., & Pourazar J., (2010)

"*Airway inflammatory response to diesel exhaust generated at urban cycle running conditions, Inhalation Toxicology,"*

Volume 22:14, Pages 1144-1150. DOI:10.3109/08958378.2010.529181.

Selin E. N. et al (2005), "*Global health and economic impacts of future ozone pollution"* Environmental

Research. Published under license by IOP Publishing Limited.

Suleman M., Gaylard M., Tshaka S. and Snyman C. (2015) "*Accelerating the Transition to Green*

Transport: Towards a South African Cities Network Green Transport Programme. Green Economy Research Report No. 1," Green Fund, Development Bank of Southern Africa, Midrand. Page 3 - 42.

Transportation Research Board (2010) "Highway *Capacity Manual*" Transportation Research Board,

National Research Council, Washington D.C. Volume 1, Page 782–793.

Vollmer D., (2011), "*Pathways to Urban Sustainability: The Atlanta Metropolitan Region: Summary*" by

National Research Council, Policy and Global Affairs, Science and Technology for Sustainability Program, Committee on Regional Approaches to Urban Sustainability.

World Health Organization (2012) "*Diesel Engine Exhaused Carcigenic in Cancer IAIRO (Ed)*" Published

by World Health Organization.

World Health Organization (2018) "*Ambient outdoor Air quality and Health Facts*"

https://web.archive.org/web/20180425044313/https://www.who.int/en/news-room/fact-sheets/detail/ambient-(outdoor)-air-quality-and-health

World Health Organization, (2021*), "WHO global air quality guidelines: particulate matter (PM2.5 and*

PM10), ozone, nitrogen dioxide, sulfur dioxide and carbon monoxide" Contributors Organización Mundial de la Salud, European Centre for Environment and Health, Published by World Health Organization Page 23-45; 56-153. ISBN 9240034226, 9789240034228.

MODELLING SIMULATION OF TEMPERATURE FLUCTUATIONS IN NATURALLY STORED IRISH POTATOES USING FINITE ELEMENT METHODS

D.M. Nyaanga[1*] V. K. Ngelechei[1], J. G. Nyaanga[2]

[1]Department of Agricultural Engineering, Egerton University, P.O. Box 536-20115, EGERTON
[2]Department of Crops, Soils and Horticulture, Egerton University, P.O. Box 536-20115, EGERTON

**** Corresponding author:*** ***dmnyaanga@egerton.ac.ke*** ***or*** ***dmnyaanga@gmail.com***

Publication Date: March 2023

ABSTRACT:

The paper outlines the modification and development of empirical and semi-theoretical models to simulate and experimental validate bulk potato temperatures at various locations and at different times of storage in boxes under free natural ventilation in stores where the temperature and relative humidity were controlled and uncontrolled. The potato temperature simulations were done using Burton (1989) and Nyaanga (1991) empirical and static models after the necessary modifications. A semi-dynamic and theoretical model named Computational Thermal Prediction (CTP). The temperature simulations were validated using experimental data for specific points was logged using thermocouple sensors. and compared with those simulated. In each case, the finite element method was used to determine the temperature at various locations within the bulk and at various time intervals. The empirical model predictions were fairly accurate (within 5% error) as compared to the observed temperatures and exhibited same trends with the time of storage. The modified Burton (1989) model gave significantly higher temperatures (…) than the observed at the centre of the box. The Nyaanga (1991) model simulations were not significantly different at the bottom, centre and top of the bulk. The CTP simulations were more accurate than the empirical models at a probability of 1% using general linear model. Generally, all the simulations and temperature measurements showed that the bulk potato temperature varied with store specifications and storage and ambient temperatures as expected in naturally ventilated bulk piles of potatoes.

Keywords: *Models: Empirical, Computational Thermal Prediction (CTP); Natural ventilation store; Temperature; Potatoes*

1.0 INTRODUCTION AND STUDY AREA

Potatoes is an important staple food crop in a number of countries in the world and is often stored to ensure availability for long periods and during transportation to far places. Temperature monitoring in stored potatoes is important since it directly influences tuber respiration, sprouting, water loss, relative humidity, chemical composition and the development of diseases, dormancy (Yachuan and Zhen-Xiang, 2021; Alamar *et al*., 2017). Optimization of the design and operational monitoring of potato storage systems, using modelling and simulation is vital for improved efficiency in the maintenance of quality and extension of their shelf life have been reported by a number of researchers including Grubben and Keesman (2015), Wang *et al*. (2019) Akdemir and Bartzanas (2015), Nyaanga (2000), Xu and Burfoot (2000), Xu *et al*. (2002), among others.

Modelling can be viewed as a simplified mathematic depiction of a specific portion of an actuality that comprises physical interrelated elements, while simulation refers to the use of high computing devices to solve models as they mimic a condition or process (Hick *et al.*, 2019) often within specific boundary conditions and conceptual assumptions. Among the different models, a mathematical model provides a description of the behaviour of real-world systems in mathematical concepts, terms, and languages such as equations, inequalities, functions, variables and constraints (Chaturvedi, 2017) being used to make predictions under specific prevailing conditions. Chourasia and Goswami (2007) modelled airflow, heat and mass transfer in partially impermeable enclosure storing potatoes as porous medium assuming a Darcy-Forccheimer steady and transient conditions without turbulence and finite volume numerical technique to compute and produce a time–temperature history and weight loss of potatoes. They reported good relationship between the predicted and observed temperatures. Similar mathematical models using Standard and Modified Arrhenius equations for transient temperature, relative humidity, air flow and transpiration rate distribution in stored products have been used and solved using the finite element method by a number of researchers including Jia *et al.* (2001), Lukasse *et al*. (2007); Plumier and Maier (2021), Crouch and Haines (2004), and Kedia *et al*. (2020).

A number of appropriate assumptions are often used to reduce the numerous independent variables that result in the existence of independent variables with very little significance on the dependent variable that reduces the prediction accuracy (Wang *et al*. 2019) in line with Yin *et al*. (2021) who recommend that mathematical models should to use suitable techniques, principles and predictors and hence must be simplified to reduce the data required to calibrate, verify and validate models as suggested by De Swaef *et al.* (2019), while avoiding clumsy and excessive modelling protocols with the aid of sensitivity functions and collinearity (Omlin *et al*., 2001) but minimising uncertainty (Chapagain *et al*., 2020). All these underscores the need for the expert developing a model to be judicious in manipulating the variables and values within acceptable levels of precision as per the perceived risks and levels of accuracy. Verification is done to evaluate whether the model complies with the conceptual specifications.

The need to intensify research on the temperature regimes in potatoes using experimental observations and mathematical modelling and simulation can be a basis of improving the design, management and hence quality and longevity of such systems as a contribution to food security.

2.0 MATERIALS AND METHODS

2.1 Physical formulations and temperature measurements

A box/crate (see Plate 1 and Fig 1) with a false floor raised at least 150mm above the ground, filled with potatoes, represents a pile or stack or bulk of product under conditions of natural convection in controlled and uncontrolled storage conditions of temperature at Silsoe Research Institute (England) and Egerton University (Kenya), respectively

(a) (b)

Plate 1 (a) Empty Potato Crates (b) Loaded Crate/box

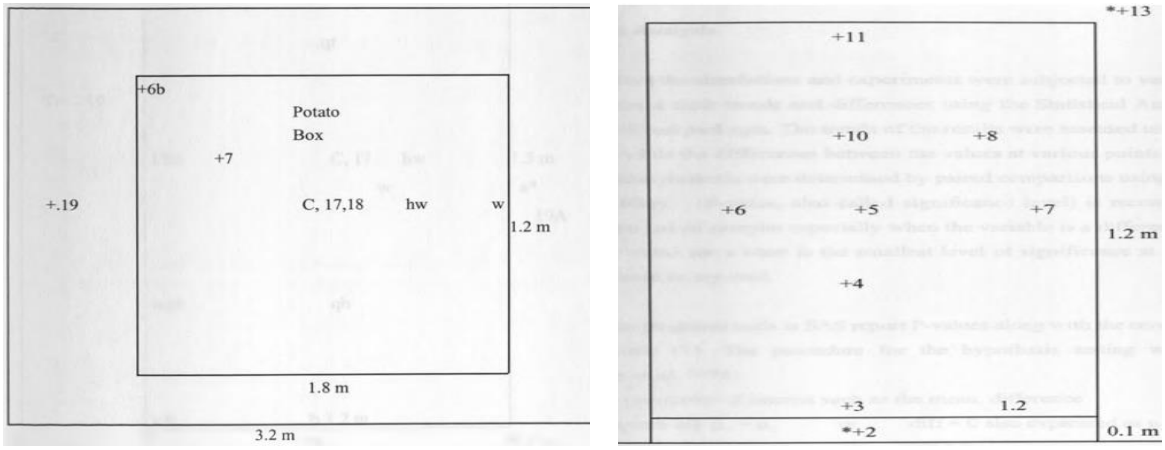

(a) (b)

Figure 1 Thermocouple Sensor Points in (a) Silose and (b)Egerton Boxes

The temperatures monitored at the bottom, quarter from the bottom, at centre, at the three-quarters from the bottom and at the top where thermocouple temperature sensors were placed). The potato boxes used measured 1.83mx1.22mx1.44m and 1.2mx1.2mx1.2m for the SRI and Egerton experiments, respectively. The height of storage was increased by stacking box/es on top of each other. The absolute and differential temperatures (between any two points), and relative humidity were measured and logged using a Delta-T Logger, Version 2.0, Delta-T Devices (1992) Ltd, Cambridge) at specified time intervals of every 2 minutes in the first week of storage thereafter every 3 hours for different storage periods up to 100 days. The temperature sensors were placed in all the three dimensions while the modelling and simulation assumed one dimensional (vertical) variation

2.2 Empirical and semi-theoretical simulations

The temperature of potatoes can be predicted using simple statistical correlations or complex differential and integral mathematical methods. Nyaanga (2000) has expressed the potato temperature empirically as

$(\Delta T)^{2.8} = 4.4\ x\ 10^{-3}(q_r H)^{1.8}$ …….. (1)

where $\Delta T = T_p - T_a$ *with* T_p *being bulk potato temperature and Ta being the ambient temperature,* q_r *= respiration rate and H = height of potato bulk (increasing with number of boxes stack on top of each other).*

Substituting, simplifying and rearranging the equation (1) becomes

$T_p = 0.144(q_r H)^{0.643} + T_a$ …… (2)

The average respiration rates (qr) from a number of researchers has been expressed by Nyaanga (2000) by linear regression equation (with $R^2 = 0.992$), in $kJt^{-1}h^{-1}$ as:

$q_r = 7.195T_p - 24.84$ ……. (3)

Or, as a power function (with $R^2 = 0.994$) as:

$q_r = 3.096{T_p}^{1.2175}$……... (4)

where q_r is the rate of respiration in $kJt^{-1}h^{-1}$, T_p is temperature in ^0C

If q_r is W kg^{-1} equation (4) becomes

$q_r = 1.998T_p * 10^{-3}$…….. (5)

Using equation (2) for q_r, and H (values of 0.01Z, 0.25Z, 0.50Z, 0.75Z and 0.99Z for different height positions from the bottom of the potato stack with a total height of Z) and the ambient/ room temperature it can be shown that:

$T_p = k\ T_r$ …….. (6)

where *k is a constant (equal to 1.094 on average for a box of potatoes measuring 1.2 by 1.2 by 1.2m experimental box) and taking the measuring points at the bottom, centre and top of the bulk, the k constants are 1.090, 1.094 and 1.095, respectively.*

Using the above empirical relationships, at finite distinct vertical points of the bulk of potatoes, the air-potato temperatures were computed and compared with those observed.

2.2.1 *Computational Thermal Prediction (CTP) formulation and simulations*

Using semi-theoretical relationships, finite difference approximation and a computer program, simulations of the temperatures at various points and boxes of different dimensions named Computational Thermal Prediction (CTP) was developed and tested for a free naturally ventilated potato storage using the potato boxes described above. The factors considered to affect the potato temperature during natural convective ventilation storage include (i) bulk size especially the height of the pile (crate or box) and its influence on rate and amount of respiration (hence metabolic heat release) and rate and amount of heat loss from the bulk mainly by free convection; (ii) room and ambient temperature, hence locality and season (time of year and day); (iii) storage duration and time (season) and their influence on the physiological characteristics of the potatoes that affect heat release such field heat, dormancy and sprouting; and (iv) specific pile physical properties of the air-potato medium such as bulk dimensions, tuber sizes, void ratio, and point at which temperature is measured. This necessitates the need for salient assumptions to enable the mathematical formulations (modelling) and their solutions (simulations).

The following assumptions as including those recommended by Burton *et al.* (1955), Hunter (1978), Lerew (1978), Brugger, (1979), Lee (1986) and Nyaanga (2000) were used in the development and use of the models:

1. There is no heat gain or loss through walls;
2. The amount of heat transfer between the bulk of potatoes and its surroundings by radiation and conduction are negligible compared to convection due to the dull surfaces and low thermal conductivities and condensation and evaporation do not occur in free natural ventilation storage where the environmental conditions between the bulk and its surrounding (store/room) are not different in terms of temperatures and relative humidity.
3. There exists a uniform bulk temperature with finite convective heat transfer between vertical potato layers. Therefore, heat energy (Q) can be expressed in terms that contain temperature.
4. The region modelled was assumed to be uniform in spatial characteristics, that is, without settling, deformation or volumetric shrinkage while the bed void volume is uniformly distributed for fairly clean and same grade (size) of potatoes which are stored for short periods especially before sprouting sets in.
5. The physical and thermal properties of potato-air such as specific heat, density, convective heat transfer coefficient, thermal conductivity and latent heat of evaporation do not vary significantly and are therefore assumed constant.
6. The potato-air (bulk) layer temperature, is assumed to be same potato-air temperature and only affected by the overall evaporation surface

area of the layer of potatoes rather than individual tubers.

Further, it was assumed that there was:

1. No variation in tuber characteristics (variety, diameter, age, rate of respiration, voids ratio among others)
2. Same storage environmental conditions of temperature, air flow, evaporation, relative humidity, etc. for model validation
3. Same vents/perforations on all sides of the boxes used for validation
4. The major direction of heat and mass low (due to thermal buoyancy) is upwards hence wall are adiabatic and horizontal gradients are negligible

2.2.3 CPT Mathematical Formulations

Theoretically, temperature can be computed from the heat energy balance between the room/store and the bulk of potatoes such as:

$$Q_s + Q_r = Q_v + Q_e + Q_c + Q_R \quad \ldots\ldots \quad (7)$$

where; Qs is the heat stored, Q_r is the heat generated by respiration, Q_v is the heat lost by ventilation, Q_e is the heat lost to evaporation, Q_c is the heat lost by conduction, Q_R is the heat lost by radiation. Neglecting all forms of heat exchange modes in line of assumption 2, equation (49) becomes:

$$Q_r = Q_v \quad \ldots\ldots\ldots\ldots\ldots\ldots\ldots\ldots\ldots\ldots.. (8)$$

Hence this enthalpy balance when taken over a differential layer during the time interval and put in differential form yields:

$$\frac{\partial Q_r}{\partial t}\Big|_z = \frac{\partial Q_v}{\partial t} \quad \ldots\ldots\ldots\ldots\ldots\ldots\ldots\ldots (9)$$

where *subscript z indicates the thickness of the bed layer*

Equation (6) was then discretised using the backward difference procedure so that it is of the form:

$$\frac{Q_{r\,z_2} - Q_{r\,z_1}}{\Delta t} = \frac{Q_{v\,z_2} - Q_{v\,z_1}}{\Delta t} \quad \ldots\ldots\ldots\ldots(10)$$

Taking the time interval to be constant, thus computing the heat energy balance within a given layer of a bed/ bulk of potatoes and equating the amount of heat of respiration (Qr) to the amount of heat removed by infiltration (Qv) yields:

$$Q_r = cpNv\Delta T \quad \ldots\ldots\ldots\ldots\ldots\ldots\ldots\ldots\ldots (11)$$

Substituting for specific heat (c) as 1.01 $kJkg^{-1}\ K^{-1}$, air density (ρ) with 1.21 kg m^{-3}, temperature difference (ΔT) with $Tp_i - Tp_{i-1}$, (N as air changes per hour and *v* as the layer volume) as recommended by Nyaanga (2000), on rearranging yields:

$$Tp_i = Tp_{i-1} + \frac{Q_r}{0.3395Nv} \quad \ldots\ldots\ldots\ldots\ldots\ldots.. (12)$$

The total heat produced by each layer (Q_{ri}) of potatoes is found by multiplying the rate of metabolic heat production (q_r) using equation (4) with the mass of potatoes which is the product of the layer volume (v) and density of potatoes (ρ_t) which yields:

$$Q_{ri} = 10^{-3}\rho_t(1-\varepsilon)(1.998Tp - 6.9)v \quad \ldots\ldots(13)$$

Substituting for Qr in equation 12 yields:

$$Tp_i = Tp_{i-1} + \frac{10^{-3}\rho_t(1-\varepsilon)(1.998Tp-6.9)}{0.3395N} \quad \ldots\ldots (14)$$

Letting:

$$C_i = \frac{10^{-3}\rho_t(1-\varepsilon)(1.998Tp-6.9)}{0.3395N_l} \ldots\ldots\ldots\ldots\ldots\ldots\ldots(15)$$

equation (13) reduces to:

$$Tp_i = Tp_{i-1} + C_i \quad \ldots\ldots\ldots\ldots\ldots\ldots\ldots(16)$$

with the initial condition that

$$Tp_1 = Tr + C_0 \quad \ldots\ldots\ldots\ldots\ldots\ldots\ldots\ldots\ldots\ldots (17)$$

where

$$C_0 = \frac{10^{-3}\rho_t(1-\varepsilon)(1.998Tr-6.9)}{0.3395N_b} \ldots\ldots\ldots\ldots\ldots\ldots (18)$$

where *Tp_i is the potato temperature at a given position with 1 being at the bottom of the bulk (°C), Tr is the room/store temperature, C_i is a constant that caters for evaporative, respiration, ventilation and conduction heat exchange between the layer, C_0 is a constant that caters for difference between the room and bottom (layer 1) potato temperature, and can be computed, Q_{ri} is the total heat produced by the mass of potatoes in the layer, v is the volume of layer of potatoes, N_b is the number of air changes in and out of the box of potatoes, N_1 is the number of air changes in each layer of potatoes.*

The constant c_0 and c_i vary with ambient conditions, thickness of potato layer (and to some extent the lateral dimensions in that these will determine the surface area over which air enters). These constants vary with locality (prevailing ambient conditions), size of bulk/box, time of storage among other factors. In general, C_0 expresses the structure's effect on the store/room temperature (Tr) and the resulting initial or boundary (first layer) bulk potato temperature (Tp1). The number of air changes through the slatted half-open floor of the potato box (N_b) is much higher than that reported and recommended for stores. This N_b increases from the centre of the bulk (the remotest point) to the periphery of the bulk, that is, the bottom and top of the box of potatoes as in equation 19

$$N_b = \frac{V_s}{\varepsilon V_b} N_s \quad \ldots\ldots\ldots\ldots\ldots\ldots\ldots\ldots\ldots\ldots (19)$$

where; *N is the number of air changes; V is the volume; s is the store; b is the box*

Taking the recommended value of N_s as 1 (Porges, 1995), can be used for the air changes for every computational layer as per the equation below:

$$N_l = \frac{V_s}{\varepsilon z V_b} \quad \ldots\ldots\ldots\ldots\ldots\ldots\ldots\ldots\ldots\ldots (20)$$

where N_l *is the number of air changes through given layer; z is the depth of the layer of potatoes;* ε *is the voids ratio of the potatoes;* V_b *is the box volume;* V_s *is the store volume.*

The assumption leading to above equations are based on the fact that a storage box is a number of times smaller than a conventional room/store and has intended openings at the bottom while the top is fully open. N is also affected by resistance to air movement up the porous medium varying with the voids ratio (ε) which in turn is a function of the size of the potatoes.

The CPT algorithms were coded yielding a computer program to calculate the constants C_0 and C_i by prompting the user to supply the required variables. The equations are solved for each layer using the previous results as input for the next, thus constituting a finite element approach hence giving a steady state profile. The program also gives the option of generating random values for the constants based on the experience and statistical data from similar storage systems. However, this option is only applicable for specified conditions and systems and the program cautions the user accordingly. The ambient (Ta) or weather station (Taw) and room/store temperature (Tr) have to be supplied from temperature measurements. The store temperature can be estimated using a model developed for the given locality and season using the weather station temperatures (Taw).

The rate of respiration heat release and a default value of 0.033W/kg was used assuming the room temperature of 20°C and a bulk density of 634 kgm^{-3} based on the Dutch Robjin potato variety used in the experimental for the research. The random c_0 and c_i values were determined by using the minimum and maximum differential temperatures between the store/room and first layer potato temperature and the lowest bulk potato temperatures respectively. The variables used in the computation of c_0 and c_i include the number of air changes in each layer per hour (N), the bulk density of the potatoes (ρ_b) and voids fraction (ε), volume of the layer (V_1) and total bulk/box (V_b) and the rate of metabolic heat release (qr). The program prompts the user to supply the variables or use one of the three options for supplying or computing the same. The number of potato layers are specified as the number of temperatures to be simulated.

The program determines and displays a numerical summary of the key temperatures and recommendations of what should be done in case the limits are exceeded. The analysis and summary from the output file include (i) minimum store/room (Tr) and potato (Tp) temperatures for each time reading (day), (ii) whether ambient temperature exceeds 30°C or the storage room and potato temperature exceeds 25°C, (ii) maximum differential potato temperature of 1.5°C is reached (iv) whether the maximum difference between potato and store temperatures exceeds 2°C, and the time when this occurs (v) give recommendations in event of exceeding the limits, including terminate the storage process or redesign the box or stack by reducing the dimensions especially the height, bottom clearance, floor and side openings or institute some management practice such as forced ventilation and cooling or passive humidification.

Using modified Burton (1989) Nyaanga (1991) and CTP program with the required inputs, the layer potato temperatures were computed and compared with the measured values at different points in the storage systems. The results from the simulations and experiments were subjected to various statistical tests to determine their trends and differences using the Statistical Analysis Systems (SAS).

3.0 RESULTS AND DISCUSSIONS

3.1 Experimental and Empirical Simulated Potato Temperatures

Tables 1 gives the experimental (observed) Burton (1989) Modified and Nyaanga (1991) empirically simulated bulk potato temperatures during the first 4 days of holding/storage freshly harvested clean potatoes at the Silsoe Research Institute

Temperature Controlled but naturally ventilated Laboratory/Store.

Table 1: Experimental (observed) Burton (1989) Modified and Nyaanga (1991), Ambient, Room and Simulated Potato Temperature for the Silsoe Trials

TIME	Ambient	Room	Experimental (Measured)		Burton (1989) Sim		Nyaanga (1991) Sim	
[Days]	Ta	Tr	Centre	Top	Centre	Top	Centre	Top
0	21.5	18.9	13.8	14.4	16.4	17.7	17.9	17.9
0.5	21.8	16.6	14.1	15.3	16.7	18.7	18.3	18.3
1	21.8	16.5	14.6	15.8	17.3	19.4	18.9	18.9
1.5	22	16.7	15	16.1	17.7	19.7	19.4	19.4
2	22.1	16.4	15.4	16.3	18.2	19.9	19.9	19.9
2.5	21.8	16.7	15.7	16.4	18.5	20	20.2	20.2
3	22.3	16.4	15.8	16.5	18.7	20.1	20.4	20.4
3.5	21.8	15.3	15.3	14.9	18.1	18.2	19.3	19.3
4	22.3	15.1	14.4	14.7	17	18	18.6	18.6
Mean	***21.9***	***16.5***	***14.9***	***15.6***	***17.6***	***19.1***	***19.2***	***19.2***

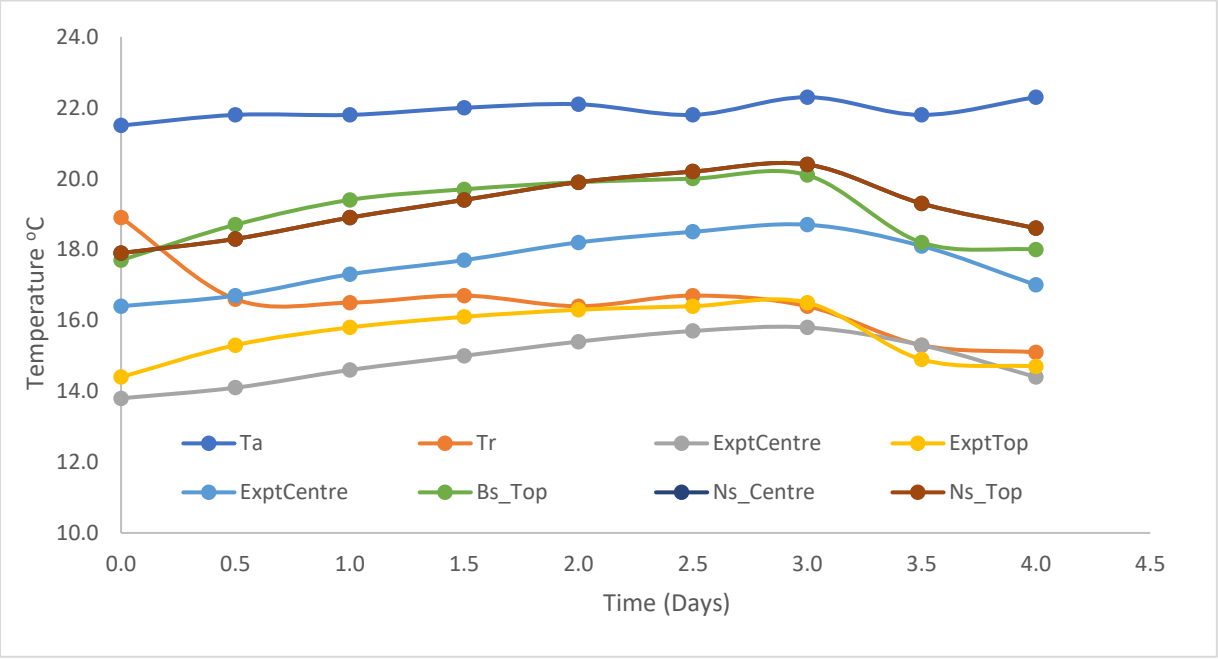

Key: T = Temperature, w = Weather station, a = Ambient, r = store/room P = potato, b = bottom of bulk of potatoes (box), c = centre of bulk, t = Top of box, B = Burton sim = simulated, N = Nyaanga

Fig 1: Observed and Burton (Bs) and Nyaanga (1991) (Ns) simulated potato temperatures during the first 4 days of holding freshly harvested clean potatoes in crates in a store maintained at 16 °C at Silsoe Research Institute.

Both experimental and simulated temperatures increased although the store temperatures remained nearly constant confirming that there was internal warming up which can be attributed to the metabolic heat release.

The temperature at the top of the bulk is higher than that at the centre by both methods. This is in agreement with the effects of buoyancy in free ventilation such that cool air enters through the bottom of the stack/box of potatoes and leaves at the top carrying the heat of respiration. The observed temperatures are lower than the simulated temperatures. The average measured centre and top temperatures are 14.94 ℃ and 15.66 ℃, respectively, while those predicted by the Modified Burton (1989) expression are 17.66 ℃ and 19.16 ℃, respectively; giving an overall average difference of the potato temperature of about 3.1 ℃.

Generally, the Burton prediction overestimates the temperatures by 2.72 and 3.5℃ for the centre and top temperatures, respectively. The difference between the observed and calculated temperature is a bit smaller for centre prediction maybe because the expression may have been developed using centre temperatures. Statistically, the difference between the experimental and the Burton predicted temperatures are significant (P<5%). This implies that the Burton expression may not be accurate although for this SRI data reducing the simulated values by an average of about 3.11℃ could suffice in the absence of any better prediction model. However, this is slightly more than twice the maximum difference of 1.4 ℃ reported by Xu *et al.* (2002) using CFD which may be contributed by the difference at room or low temperature storage.

The Nyaanga (1991) model prediction gives 19.33 ℃ and 19.32 ℃ for the centre and top temperatures, respectively. It overestimates the centre and top temperatures by 4.39 and 3.66℃ respectively. These are much bigger margins than those by Burton model for the same data. This could be attributed to the fact that Burton expression was developed using temperate temperature ranges as those of the SRI data while Nyaanga model was developed using tropical temperature ranges.

The Egerton experimental data and empirically simulated temperatures (Tables 2 and A1 and Fig 1 and 2) using the modified Burton (1989) (TpB) and Nyaanga (1991) (TpN) were also analysed for the first 44 days (7 weeks) of storage under free ventilation in an uncontrolled temperature room. The observed bulk temperature at the centre was higher than the ambient temperature throughout the 33 days of storage. The simulated temperature has the same trend as the ambient temperature, rising and falling at nearly the same time. The simulated temperature is higher averaging 21.49 ℃ with a higher variation (3.28℃) unlike the measured temperature (average 20.51℃ with a smaller variation of 1.02 ℃.

Table 2: Weather station, Experimentally Observed, Burton (1989) and Nyaanga (1991) simulated Potato Temperatures for Egerton Uncontrolled storage

	Experimental Observed Temperatures						**Simulated Potato Temperatures**					
Time (days)	**Environmental Temperatures**			**Measured Potato Temperatures**			**Burton (1989) Sim (TpB)**			**Nyaanga (1991) Sim (TpN)**		
	Taw	**Tae**	**Tre**	**P_b**	**P_c**	**P_t**	**PB_b**	**PB_c**	**PB_t**	**TN_b**	**TN_c**	**TN_t**
1	19.9	20.3	20.8	20.7	20.8	21.0	21.1	21.1	22.6	23.8	22.7	22.7
3	19.5	19.7	20.6	20.6	21.0	21.4	21.1	20.5	22.1	23.2	22.6	22.7
6	19.3	19.9	20.7	20.2	20.7	21.2	20.9	20.7	22.2	23.4	22.1	22.1
9	19.2	19.7	20.7	20.3	20.7	21.4	20.9	20.4	22.0	23.1	22.1	22.1
12	19.0	18.5	20.0	20.1	20.5	21.1	20.4	19.2	20.8	21.9	22.0	22.0
15	18.0	18.2	20.1	19.7	20.2	20.7	20.3	19.7	21.2	22.4	21.6	21.6
18	18.3	19.7	20.7	20.1	20.4	21.0	20.7	20.4	23.1	22.0	22.1	22.1
21	17.7	19.1	20.4	20.1	20.4	20.9	20.6	19.8	21.4	22.5	22.0	22.0
24	18.1	19.0	20.4	20.1	20.5	20.9	20.5	19.8	21.4	22.5	22.0	22.0

Time (days)	Experimental Observed Temperatures						Simulated Potato Temperatures					
	Environmental Temperatures			Measured Potato Temperatures			Burton (1989) Sim (TpB)			Nyaanga (1991) Sim (TpN)		
	Taw	Tae	Tre	P_b	P_c	P_t	PB_b	PB_c	PB_t	TN_b	TN_c	TN_t
27	19.0	17.8	20.2	20.0	20.4	20.8	20.4	18.5	20.0	21.1	21.9	21.9
30	17.0	18.0	19.9	19.9	20.1	20.3	20.1	18.9	20.3	21.4	21.7	21.7
33	18.4	19.0	20.1	19.8	20.1	20.4	20.2	19.7	21.6	22.4	21.7	21.7
Mean	**18.6**	**19.1**	**20.4**	**20.1**	**20.5**	**20.9**	**20.6**	**19.9**	**21.6**	**22.5**	**22.0**	**22.1**

Key: T = Temperature, w = Weather station, a = Ambient, r = store/room P = potato, b = bottom of bulk of potatoes (box), c = centre of bulk, t = Top of box, B = Burton sim = simulated, N = Nyaanga

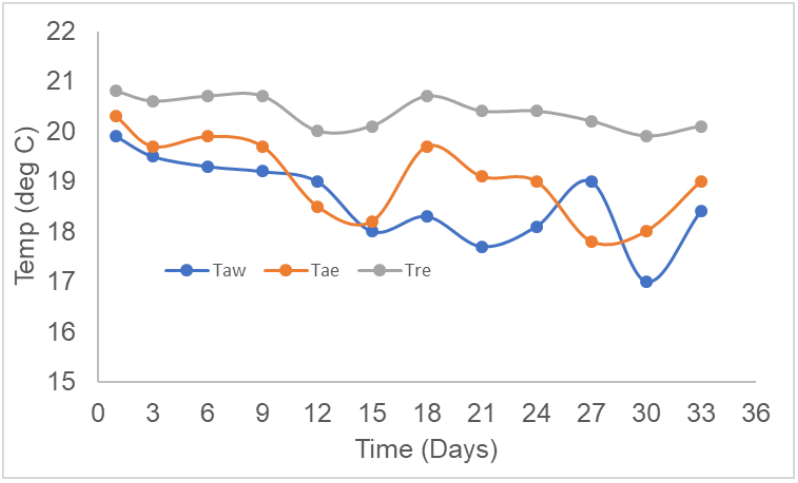

Fig 1: Weather station, ambient and room (store) temperature during the first 33 days of potato storage at Egerton

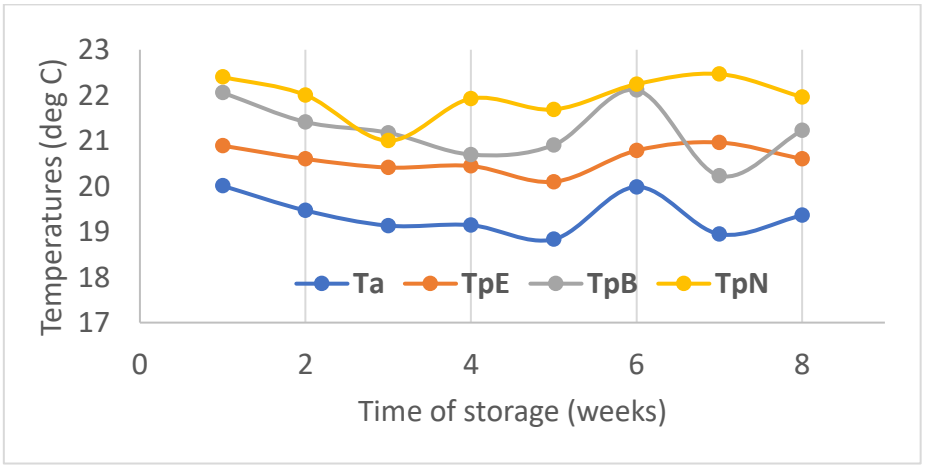

Fig 2: Average ambient and experimental bulk potato, Burton (1989) and Nyaanga (1991) simulated temperatures during the first 8 weeks of potato storage at Egerton

The SAS output of simulated Modified Burton (1989), observed (expt) temperature differences between different points of the bulk of the stored potatoes are given in Table 3 for Silsoe Research Institute (SRI) data. The paired differences are analysed and compared.

Table 3: ANOVA for paired temperature differences (variable) for SRI* trials

Data	Variable	N	Mean (^{0}C)	Std Error	T	Prob>|T|
Burton sim*	Centre- top	102	-1.506	0.061	-24.823	0.01%
Expt	Lab-store	19	5.395	0.301	17.901	0.01%
Expt	Lab-bulk centre	19	7.085	0.136	52.261	0.01%
Expt	Lab-bulk top	19	6.376	0.174	36.584	0.01%
Expt	Store-bulk centre	19	1.690	0.329	5.128	0.01%
Expt	Store-bulk top	19	0.981	0.310	3.163	0.01%
Expt	Bulk centre-bulk top	19	-0.709	0.109	-6.514	0.01%

**SRI=Silsoe research Institute, N= number of data, Burton sim=Burton (1989) simulated, Expt=experimental data, lab=laboratory temperature, bulkcent=temperature at the centre of bulk of potatoes,*

Statistically there are no differences between the various temperature differences except at probabilities of 0.01%. The store and bulk dewpoint temperatures were about 14°C and 13.5°C, respectively at the start, both rising to 14. 2°C. The increase was greater in the bulk indicating some moisture input in the bulk from the potatoes' respiration process. The average bulk potato temperature was about 3°C lower than its surroundings (the store) at the start of free natural ventilation storage. This difference reduced to about 1.2°C in less than 3 days with the store temperature remaining fairly constant at about 16.8°C, an indication that heat is generated by the potatoes. The ambient and hence store temperature has influence of the potato temperature. It was also observed that the relative humidity at the centre of the box of potatoes was higher than that in the store due to the moisture being released as a by-product of the respiration process, increasing from 90% and 80% to 99% and 91% for the bulk and store, respectively within 3 days.

The mean difference between the mean potato and mean observed ambient (Tpm-Tam) temperature was 1.44°C which is within the range (1-2°C) reported by Burton et al. (1955), Burton (1989) and Nyaanga (1991) for a free natural storage system. The average of the various bulk temperatures was taken as a mean potato temperature and was found to be nearly equal to the centre bulk temperature as has been suggested by Nyaanga (1991). The small overall (over the 44 days of storage) mean difference between the potato and room temperature (Tpm-Trm) of 0.16°C supports Burton et al. (1955) conclusions that the potato temperature during naturally ventilated storage settles down to the average ambient /store temperature. Both theoretically predicted and physically/experimentally measured bulk potato temperatures at various locations during the 44 of the 100 days of storage in perforated boxes (crates) of different heights under free natural ventilation. The overall mean ambient and experimentally observed and simulated temperatures during the first 8 weeks of potato storage at Egerton are presented in Fig 3 confirming that the differences among them are not significant.

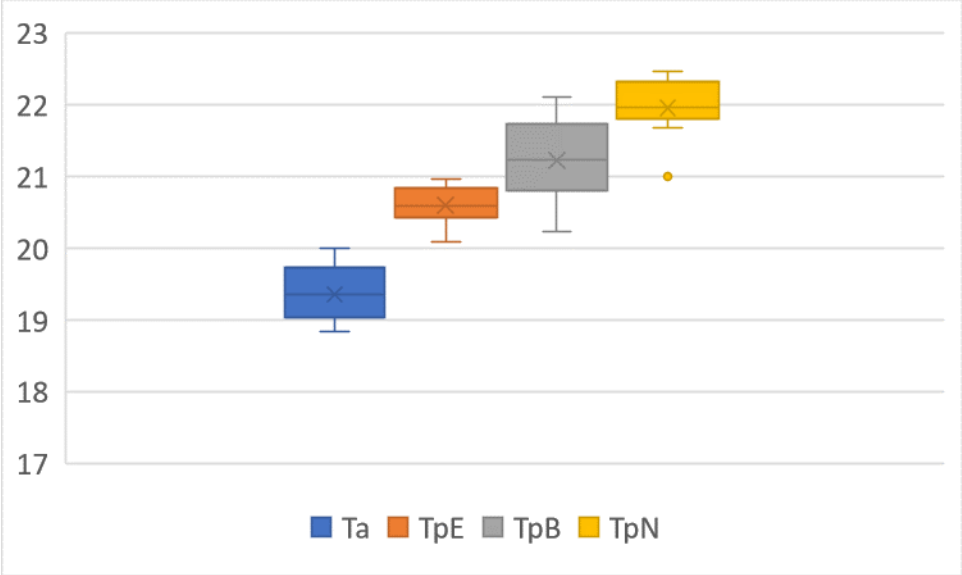

Fig 3: Average ambient and experimental bulk potato, Burton (1989) and Nyaanga (1991) simulated temperatures during the first 8 weeks of potato storage at Egerton

Available empirical models were modified and a semi-theoretical Computational Thermal Prediction (CTP) developed have been validated with experimental temperature data.

There was no significant temperature variation in the y and x axes (It was assumed that the major direction of heat and mass flow (induced by the temperature gradient or thermal buoyancy) in a box of potatoes is upwards (one dimensional airflow of the plug-flow type) system.

The Burton (1989) simulated with the Egerton measured temperatures at the top and bottom of the bulk, show that the simulated potato temperature varies and fluctuates with the same trend as that of the ambient temperature, but the potato (particularly centre) temperature is fairly stable throughout the storage period. The measured top and bottom temperatures are fairly uniform though not equal. The top temperature is consistently higher than the bottom temperature as expected due to self-warming of the bulk due to the heat of respiration. The maximum temperature gradient is about 0.85℃ between the top and bottom of the bulk from the observed values. On average, the bottom Burton simulated temperatures are slightly lower by about 0.25℃, than the actual bottom observed temperatures. However, the simulated Burton top potato temperature (average 21.0 ℃) are consistently higher by an average of 1.64℃ agreeing fairly with that reported by Xu et al (2002) than the actual observed temperature (averaging 22.6℃).

The observed and Nyaanga (1991) simulated bulk potato temperatures were the same at the bottom, centre and top but consistently higher than the measured temperature although with exactly the same trend. This similarly could be attributed to the fact that the model just increases the room temperature by a multiplying factor of 1.094. This also confirms that the potato temperature is a function of the storage/room temperature. Nyaanga (1991) potato simulated temperature averages about 22.06 ℃ with a variation of 1.15 ℃ thus predicting an average top, centre and bottom temperatures of 1.06 ℃, 1.55 ℃ and 1.90 ℃ above the observed, respectively. The inability of the model to predict the temperature differential gradient through the bulk vertically, is a major limitation. In this respect, the Burton model prediction is better.

The most important observation in the two empirical prediction equations and simulations

is that the potato temperature is directly related to the room and ambient temperatures and therefore the prediction of the bulk potato temperature is mainly determined by the prevailing room or ambient temperature. With appropriate factors the equations could be used to predict the bulk potato temperature to some accuracy. These results generally agree with Xu et al. (2002), Jia et al. (2001), Plumier and Maier (2021), Mazima et al. (2016) and Akdemir and Bartzanas (2015) although with slightly different magnitudes. The variations are due to differences of potato varieties, sizes, type of cooling even if the average major diameter is 75mm as has been reported by Tabatabaeefar (2002) and Ebrahem, et al. (2011) as generally adopted in this research.

3.2 Computational Thermal Prediction (CTP) Simulation

The Computational Thermal Prediction (CTP) simulation (for storage bulk of 1.2x1.2x1.2m and a period of 44 days of storage at an average daily temperature of 19℃) indicated safe storage with respect to the criteria specified (different options of the code in the CTP program) based on the Egerton experimental box, setup, conditions and data. The CTP simulated and measured top bulk temperature including the room and ambient temperatures. The CTP simulated and observed top temperatures closely follow each other in trend and magnitude although the simulated temperature (averaging 21.15℃) curve has daily deviation of about 0.5℃ from the mean trend. The observed overall mean bulk top temperatures were 21.0 ℃. the average room temperature (21.7 ℃) is lower than both the potato temperatures (21.0 ℃) throughout the 44 days of storage and data collection. This can be attributed to the heating effect due to release of metabolic heat by the potatoes. The average store/room temperature (20.47℃) was higher than the ambient (weather station) temperature (19.21℃) due to the near-greenhouse effect of the structure housing the storage room.

The top temperatures, the CTP simulated and observed centre temperatures do not have exactly the same trend and their magnitudes are slightly different. The simulated temperature (averaging 21.05℃) is slightly higher than the observed temperature (averaging 20.51℃) with the simulated (similar to the room) trend exhibiting a slightly a wider variation of 0.3℃. The similarity between the CTP simulated and room temperature can be attributed to the use of the room temperature in the CTP formulation. The CTP simulation underestimates the temperature by an average of 0.8℃ but has a trend which resembles that of the observed (averaging 21℃ during the whole storage period). There is a general similarity between the observed and simulated temperature trend, implying that the model is valid. The measured potato temperatures do not fluctuate as much as the simulated ones. This is true at all the vertical monitoring positions in the bulk, although it is more pronounced in the lower layers. The lower positions (near the inlet of the convective air flow) are more prone to the wider room or store temperature changes while the centre and upper layers are cushioned against this by the poor conducting air -potato medium. The effect of the surrounding room temperature on the bulk temperature is equivalent in that the simulated temperature trend is exactly the same as that of the room temperature.

Other simulation options including the use of weather station temperatures, different bulk sizes and comparing different potato temperatures are possible. The results from the model will depend on the input parameters such as the prevailing environmental temperature, storage period and conditions of the potatoes. The program is only valid for medium grade, mature clean ware potatoes held or stored under natural convective ventilation. The quadratic equation gave values that are far outside the range of study implying that the regression equation from the Tr and Ta (Egerton data) is not reliable; this was indicated by the equation's low coefficient of regression. Table 2 gives paired comparisons of some temperatures and CTP simulation options with the null hypothesis that H_o: $diff_i = 0$ with the alternative HA: $diff_i \neq 0$.

Table 2: ANOVA for paired temperature differences

Variable	N	Mean	Std Error	T	Prob>|T|
Ta-Tr	1	1.50	0.061	-24.823	0.01%
Ta-Tec	2	5.395	0.301	17.901	0.01%
Ta-Tfsc	3	7.085	0.136	52.261	0.01%
Ta-Trsc	4	6.376	0.174	36.584	0.01%
Tr-Tec	5	1.690	0.329	5.128	0.01%
Teb -Tec	6	0.981	0.310	3.163	0.01%
Teb-Tfsb	7	-0.709	0.109	-6.514	0.01%

Statistically, there are significant differences between all the experimental, CTP simulated (with the two options) at all points of determination (bottom, centre, top of bulk, room, and ambient). All the differences are significant at a probability of 0.01%. the same pattern of relationship s exists between the variedly CTP simulated temperatures among themselves and when compared to the observed values. This implies the assumptions and procedures in the model are accurate.

Generally, the predicted values are higher than the observed. The differences could result from assumptions and constants used in the mathematical model in relation to the major modes of heat exchange and the quantification of the constants. The assumptions that infiltration convection heat loss is equal to the respiration rate may not be absolutely correct due to the presence of other forms of heat exchange and restrictions to free natural air flow may have not been accurately quantified through the use of N. These two are therefore taken to be major sources of error in the CTP simulation.

4.0 CONCLUSIONS

The results of the research indicate that it's possible to predict the bulk potato temperature using empirical mathematical expressions such as the modified Burton (1989) and Nyaanga (1991) models; develop and validate a more generalizable computational Thermal Prediction (CTP) model for the simulation of potato temperatures in free naturally ventilated potato storage stacks.

The empirical models are not as accurate as the experiments but they gave accurate trends (history) of the bulk potato temperatures with the time of storage. The modified Burton (1989) model shows the temperature gradients in a bulk of potatoes although with slightly higher magnitudes and variations. The Nyaanga (1991) model simulations gave nearly the same values for all the major temperatures within a bulk of potatoes (that is, the temperature at the bottom, centre and top were the same).

The computational thermal prediction (CTP) simulations were more accurate than the empirical models and the program gave a wide range of options. The individual temperature trends, by various CTP options and at the different points of monitoring were same at probability of 1% using SAS general linear model.

Author Contributions

DNM conceived the study design and CTP model development. VKN led the revalidation data collection. JGN supported data analysis. All contributed to the overall quality of the draft manuscript and its revisions. All authors have read and approved the final manuscript.

5.0 REFERENCES

Akdemir, S. and Bartzanas, T. (2015). Numerical Modelling and Experimental Validation of a Cold Store Ambient Factors. Journal Of Agricultural Sciences 21 (2015) 606-619 https://doi.org/10.1501/Tarimbil_0000001361

Alamar, M. C., R. Tosetti, Landahl, S., Bermejo, B. and Terry, L. A. (2017) (2017). Assuring Potato Tuber Quality during Storage: A Future Perspective; Front Plant Sci.. 8: 2034. doi: 10.3389/fpls.2017.02034. PMCID: PMC5712419, PMID: 29234341

Brugger, M.F. (1979). A Two-dimensional finite difference model of the transient environment within a potato pile. Unpublished PhD Thesis. University of Wisconsin- Madison.

Burton, W.G. (1989). The Potato. 3rd Ed. Longman Scientific & Technical. Harlow, England, London. Pp: 1, 547-598.

Burton, W.G.; Mann, G. and Wager, H.G. (1955). The storage of ware potatoes in permanent buildings ii. The temperature of unventilated stacks of potatoes, J. agr. Sci. Camb. 46:439-42.

Chapagain R., Ojeda J., Mohammed C., Brown J., Remenyi T. and Harris R. (2020). Historical and current approaches to decompose uncertainty in crop model predictions. Paper presented at the Second International Crop Modelling Symposium (iCROPM 2020), Le Corum Montpellier France.

Chaturvedi, D.K. (2017). Modeling and Simulation of Systems Using MATLAB® and Simulink®. Boca Raton, FL: CRC press.

Chourasia, M.K. and Goswami T.K. (2007). Three dimensional modeling on airflow, heat and mass transfer in partially impermeable enclosure containing agricultural produce during natural convective cooling. Energy Conversion and Management, 48(7):2136-2149. DOI: 10.1016/j.enconman.2006.12.018

Crouch R and Haines C (2004) Mathematical modelling: transitions between the real world and the mathematical model. International Journal of Mathematical Education in Science and Technology 35, 197–206.

De Swaef T, Bellocchi G, Aper J, Lootens P and Roldán-Ruiz I. (2019). Use of identifiability analysis in designing phenotyping experiments for model- The Journal of Agricultural Science 163 https://doi.org/10.1017/S0021859622000259

Delta-T Devices Ltd. (1992). Delta-T Logger; User Manual. Version 2.0. Cambridge

Ebrahem, I. Z., Ayman, A. E. and Guidetti, R. (2011). A New Small Potato Planter for Egyptian Agriculture. J. of Ag. Eng. - Riv. di Ing. Agr. 3:7-13

Grubben, N. L. M., and K. J. Keesman. (2015). Modelling ventilated bulk storage of agromaterials: A review. Computers and Electronics in Agriculture, 114:285-295

Hick, H., Bajzek, M. & Faustmann, C. Definition of a system model for model-based development. SN Appl. Sci. 1, 1074 (2019). https://doi.org/10.1007/s42452-019-1069-0

Hunter, J.H. (1978). A simulation model for potato storage ventilation. ASAE Paper No. 78-4061

Iguaz, A., Arroqui, C. Esnoz, A. Vírseda P. (2004). Modelling and Simulation of Heat Transfer in Stored Rough Rice with Aeration. *Biosystems Engineering*. Vol 89(1) 69-77

Jia, C., Sun, D., Cao, C. (2001). Computer simulation of temperature changes in a wheat storage bin. Journal of Stored Products Research 37(2):165-177. https://doi.org/10.1016/S0022-474X(00)00017-5

Kedia, P., Shankar, B.K., Rai B. (2020). Temperature and humidity based models for the prediction of transpiration rate in potatoes during storage. Journal of Food Process Engineering. 44(10). https://doi.org/10.1111/jfpe.13626

Lee, K. (1986). Heat and mass transfer in highly porous media. PhD Thesis. The University of Texas at Austin. University Microfilms International. USA

Lerew, L. E. (1978). Development of a temperature-weight loss model for bulk stored potatoes. Phd Thesis. Michigan State University. University microfilms international. Ann Arbor. Michigan. USA.

Lukasse, L.J.S., de Kramer-Cuppen, J.E. and van der Voort, A.J. (2007). A physical model to predict climate dynamics in ventilated bulk-storage of agricultural produce. International Journal of Refrigeration 30(1):195-204. DOI: 10.1016/j.ijrefrig.2006.03.011

Mazima, J. K., Agbinya, J., Manasseh, E. and Kaijage, S. (2016). Stochastic Modeling Technology for Grain Crops Storage Application: Review. International Journal of Artificial Intelligence and Applications (IJAIA), Vol. 7(6) 27-42. DOI: 10.5121/ijaia.2016.7603 27

Nyaanga, D. M. (2000). Prediction of potato bulk temperature during free natural convection storage. PhD Thesis, Agricultural Engineering Department, University of Nairobi.

Nyaanga, D.M. (1991). Factors affecting the Bulk size of stored potatoes. Unpublished Msc. Thesis University of Nairobi Kenya.

Omlin, M. Brun, R. and Reichert, P. (2001). Biogeochemical model of Lake Zürich: sensitivity, identifiability and uncertainty analysis. Ecological Modelling, Vol (141)1–3:105-123. https://doi.org/10.1016/S0304-3800(01)00257-5.

Plumier, B. and Maier, D. (2021). Effect of Temperature Sensor Numbers and Placement on Aeration Cooling of a Stored Grain Mass Using a 3D Finite Element Model. *Agriculture*, 11(3), 231; https://doi.org/10.3390/agriculture11030231\

Porges, F. (1995) HVAC Engineers Handbook, pp90-93. 10th ed. Butterworth -Heismann ltd. Oxford.

Tabatabaeefar A. (2002). Size and shape of potato tubers. International Agrophysics 16(4) 16, 301–305:

Wang, D., Lai, Y., Zhao, Hongxia, J., Binguang, Wang, Q. and Yang, X. (2019). Numerical and Experimental Investigation on Forced-Air Cooling of Commercial Packaged Strawberries. *International Journal of Food Engineering*, vol. 15, no. 7, 2019, pp. 20180384. https://doi.org/10.1515/ijfe-2018-0384

Xu, Y. and Burfoot, D. (2000), Modelling the application of chemicals in box potato stores, Pest Management Science, Vol 56, pp 111-119

Xu, Y., Burfoot, D. and Huxtable, P. (2002). Improving quality of stored potatoes using computer Modelling. Computers & Electronics in Agric., 34, 159-171

Yachuan Z. and Zhen-Xiang L. (2021). Effects of Storage Temperature and Duration on Carbohydrate Metabolism and Physicochemical Properties of Potato Tubers. J Food Nutr 7: 1-8.

Yin, X., Struik, P.C. and Goudriaan, J. (2021). On the needs for combining physiological principles and mathematics to improve crop models. *Field Crops Research*. https://doi.org/10.1016/j.fcr.2021.108254

Appendix

Table A1: Forty-four (of the 100) days of daily temperatures during the naturally potato storage at Egerton University Lab

Day	Taw	Tae	Tre	Tpce	Tpte	TpbB	TpcB	TptB	TbN	TcN	TtN
1	19.9	20.3	20.8	20.8	21.0	21.1	22.6	23.8	22.7	22.7	22.7
2	19.8	19.7	20.7	21.1	21.4	20.4	22.0	23.3	22.8	22.8	22.8
3	19.5	19.7	20.6	21.0	21.4	20.5	22.1	23.2	22.6	22.6	22.6
4	19.9	19.4	20.5	20.9	21.4	20.2	21.8	22.9	22.4	22.4	22.4
5	19.0	19.9	20.5	20.8	21.3	20.6	22.2	23.3	22.2	22.1	22.2
6	19.3	19.9	20.7	20.9	21.2	20.7	22.2	23.4	22.1	22.1	22.1
7	18.9	20.2	20.7	20.9	21.3	21.0	22.6	23.7	22.2	22.2	22.2
8	19.2	20.2	20.1	20.7	21.3	21.0	22.6	23.7	22.2	22.2	22.2
9	19.2	19.7	20.7	20.7	21.4	20.4	22.0	23.2	22.2	22.2	22.2
10	19.7	19.7	20.5	20.7	21.4	20.4	22.0	23.2	22.2	22.2	22.2
11	19.1	18.4	20.4	20.7	21.3	19.1	20.7	21.9	22.1	22.1	22.1
12	19.0	18.5	20.0	20.5	21.1	19.2	20.8	21.9	22.0	22.0	22.0
13	17.7	19.0	20.1	20.4	20.8	19.7	21.3	22.4	21.7	21.7	21.7
14	18.2	19.4	20.1	20.3	20.7	20.1	21.6	22.8	21.7	21.6	21.6
15	18.0	19.0	20.1	20.2	20.7	19.7	21.2	22.4	21.6	21.6	2.6
16	17.4	19.9	20.3	20.2	20.6	19.6	21.1	22.2	21.7	21.7	21.7
17	17.3	19.9	20.6	20.2	20.7	20.6	22.2	23.3	21.8	21.8	21.8
18	18.3	19.7	20.7	20.4	21.0	20.4	22.0	23.1	22.1	22.1	22.0
19	18.3	18.5	20.4	20.6	21.1	19.2	20.8	22.0	22.2	22.2	22.2
20	17.6	18.3	20.4	20.5	21.0	19.0	20.6	21.7	22.1	22.1	22.1
21	17.7	19.1	20.5	20.4	20.9	19.8	21.4	22.5	22.0	22.0	22.0
22	19.3	19.3	20.5	20.5	20.9	20.0	21.6	22.8	22.0	22.0	21.0
23	18.8	18.9	20.5	20.5	20.9	19.6	21.1	22.3	22.1	22.1	22.1
24	18.1	19.1	20.4	20.5	20.9	19.8	21.4	22.5	22.1	22.0	22.0
25	18.2	18.6	20.3	20.4	20.8	19.3	20.8	22.0	22.0	22.0	22.0
26	19.2	18.0	20.4	20.3	20.8	18.7	20.3	21.4	21.9	21.9	21.9
27	19.0	17.8	20.2	20.4	20.8	18.5	20.0	21.2	21.9	21.9	21.9
28	17.3	18.3	20.0	20.3	20.7	19.0	20.6	21.7	21.9	21.9	21.9
29	16.9	17.9	19.9	20.2	20.5	18.6	20.2	21.3	21.8	21.8	21.8

30	17.0	18.1	19.9	20.1	20.3	18.8	20.3	21.4	21.7	21.7	21.7
31	17.1	18.6	20.0	20.1	20.3	19.3	20.9	22.0	21.7	21.6	21.6
32	18.0	18.5	20.1	20.0	20.3	19.2	20.7	21.8	21.7	21.7	21.7
33	18.4	19.0	20.1	20.1	20.2	19.7	21.3	22.4	21.7	21.7	21.7
34	17.4	19.5	20.2	20.1	20.4	20.2	21.8	22.9	21.7	21.7	21.7
35	18.5	20.0	20.5	20.1	20.6	20.7	22.2	23.4	21.7	21.7	21.7
36	18.9	19.6	20.8	20.3	20.8	20.3	21.9	23.0	21.9	21.9	21.8
37	20.0	20.9	21.0	20.5	21.2	21.6	23.2	24.3	22.1	22.1	22.1
38	19.1	20.4	20.9	20.7	21.4	21.1	22.7	23.8	22.3	22.3	22.3
39	18.5	20.1	20.8	20.8	21.5	20.8	22.4	23.6	22.4	22.4	22.4
40	19.1	20.5	21.1	20.7	21.4	21.2	22.8	24.0	22.3	22.2	22.2
41	19.1	19.7	21.2	20.8	21.6	20.4	22.0	23.2	22.4	22.3	22.3
42	18.5	18.5	21.0	21.0	21.7	19.2	20.9	22.0	22.5	22.5	22.5
43	17.2	19.0	20.8	21.0	21.6	21.1	19.8	21.4	22.5	22.5	22.5
44	18.6	17.6	20.5	21.5	20.6	18.3	19.9	21.1	22.4	22.4	22.4
Mean	18.5	19.2	20.5	20.5	21.0	19.9	21.5	22.6	22.1	22.1	21.6

Key: T = Temperature, w = Weather station, a = Ambient, r = store/room P = potato, b = bottom of bulk of potatoes (box), c = centre of bulk, t = Top of box, B = Burton sim = simulated, N = Nyaanga

NUMERICAL AND EXPERIMENTAL TECHNIQUES OF FLEXURE PROPERTIES OF MONO AND HYBRID NANOCELLULOSIC COMPOSITES

W. W.Webo [1*], L. M. Masu [2], P.K Nziu [3]

[12]Technical University of Kenya, Faculty of Engineering and Built Engineering, School of Mechanical and Manufacturing Engineering, Nairobi, Kenya.
[3]Moi University, School of Engineering, Department of Manufacturing, Industrial and Textile Engineering, Eldoret, Kenya

Corresponding author*: *wilsonw@vut.ac.za*

Publication Date: March 2023

ABSTRACT:

This study aimed to focus on the state of knowledge and practice on natural fibres, extract cellulose, and subsequent formation of nanocellulosic fibres and particles from selected natural fibres. Moreover, both mono and hybrid composites were fabricated. Sisal and rice husk were selected for this purpose due to their ease of availability.

An experimental solution was used to extract cellulose, and, subsequently, nanofibres and nanoparticles were formed. These were then used to fabricate composites. Finite Element Analysis (FEA) using ABAQUS/CAE software version 2018 was used to develop novel models of mono and hybrid nanocomposites and to determine their flexural properties. The finite element analysis method incorporates the effects of nonlinearities which are very common in composite fabrication. Moreover, analysis of variance was done for each property under study. This study found that the hybrid composites had higher performance than the monocomposites. Moreover, there was evidence of the flexural properties increasing with fibre volume fractions up to an optimum point. Beyond this optimum point, there was evidence of the flexural properties reducing with further fibre additions.

Keywords: *Numerical, Experimental, Flexure, Nanofibre, Abaqus, Cellulose*

1.0 INTRODUCTION

Numerical methods like finite element analysis are used to obtain solutions for problems where the boundary conditions are defined. The solutions are obtained using either the boundary element method or the mesh free method, depending on the problem at hand (Dharmin *et al*., 2012). They are mostly used in applications where stresses change rapidly (Kharat and Kulkarni, 2013).

While using the finite element analysis, the structural body has to be divided into small pieces with simple shapes. Equations will then be automatically generated using the software that helps describe the elements and the connectivity between the elements at the nodes. The equations generated from the software will help to relate different parameters. For example, if we have a known parameter such as a load, it can be related to an unknown parameter such as displacement.

Finite Element Analysis software normally solves a large set of simultaneous equations in order to obtain the values of stress in the whole model. Computer software programming softwares that use the Finite Element analysis method and have been developed include: COSMOL, ADINA, NASTRAN, ABAQUS and LUSAS. These softwares are commonly used to perform stress analysis.

The benefits of using numerical techniques include convenience, high speed and accuracy (Nziu, 2018; Zhang *et al.*, 2012). The factors that are considered during modeling in order to obtain accurate results include boundary conditions and material definition (Qadir *et al.*, 2009). It is also possible to perform finite element analysis using a small part of the whole model (Masu, 1991), with the benefit that the memory required will be small, and the time required to perform the analysis will be reduced (Kihiu and Masu, 1995).

The outstanding biodegradability characteristic of cellulose nanofibrils makes them to be a keen focus of research. Hybrid nanocomposites have the advantage of resulting into high strength (Börjesson *et al.*, 2018; Liimatainen *et al.*, 2013; Oksman *et al.*, 2016).

Ismail *et al*. (2019), used two fillers namely cellulose nanofibrils and nanosilica, in conjunction with chitosan matrix to form a hybrid nanocomposite. The authors noted that the nanocomposites had high strength and stiffness.

El-Feky *et al*. (2019) used various contents of nanocellulose fibres and nanosilica as fillers to reinforce cement composites. The authors noted that the increase in strength was about 2 times higher than that for the control mix.

Nia *et al*. (2020), studied a novel type of hybrid nanocomposite made using silica cellulose and aerogel fillers. The authors found out that the nanocomposite was very efficient in adsorption of dyes from water.

Farooq *et al*. (2020), did an excellent review on the sources of cellulose, the extraction of nanocellulose from cellulose, and also the properties of nanocomposites fabricated from nanocellulose and zinc oxide. The authors noted that the nanocellulose and zinc oxide complement each other resulting in excellent mechanical properties.

Bay *et al*. (2021), used nanofibrillated cellulose (NFC) combined with nanosilicon dioxide as fillers, and polyvinyl alcohol as matrix to fabricate nanocomposites. The casting method was used to prepare the nanocomposites at different filler loadings. The authors noted an increase in strength and stiffness of the fabricated composites.

Jaafar *et al*. (2021), used silica kenaf as fillers on toughened epoxy matrix to fabricate composites. The authors investigated the morphological and mechanical properties of the resulting composites. The authors noted that there was increase in the flexural strength. The SEM analysis revealed that optimum mechanical properties had been achieved.

Suhot *et al*. (2021) carried out extensive research on the works that had been done between 2017 and 2021. The authors noted a gap in the use of finite element analysis, and they recommended the development of the same.

The low mechanical strength of natural fibres are usually attributed to the incompatibility between the hydrophilic fibres and the hydrophobic matrices (Manral and Bajpai, 2020). Many strategies have been advanced to try and solve this problem including the use of chemical treatments (Akbar and Emami, 2018) and compatibilizers (Moradi *et al.*, 2019) in order to improve the mechanical properties. This study, therefore, sought to stretch the boundaries of the aforementioned body of knowledge with regards to improving the mechanical properties, by producing nanocellulosic fibres which are expected to increase the flexural properties of the resulting mono and hybrid nanocellulosic composites. Furthermore, the use of finite element analysis is a novel idea that has been considered in this study to model the flexural properties. This coincides with the recommendations of Suhot *et al*. (2021). The experimental results were used to validate the numerical results.

2.0 MATERIALS AND METHOD

2.1 Experimental Method

2.1.1 Materials

In this study, epoxy resin, (LR-20) with LH-281 hardener, were used. Epoxy resin was used in this study because of its excellent resistance to

environmental degradation. The fillers and particles which were used in this study were sisal nanofibres and rice husk nanosilica particles, which were extracted from the sisal fibres and rice husks, respectively. The standard acid hydrolysis procedure was adopted to obtain sisal nanofibres. The rice husk nanosilica particles were obtained by acid hydrolysis and subsequently, calcinating the rice husks in a furnace followed by dry grinding in a ball mill in order to obtain the nanosilica particles.

2.1.2 Composite Fabrication

The standard hand layup technique was adopted in the fabrication of mono and hybrid composite specimens. At least five specimens were prepared per volume fraction. The volume fractions were determined scientifically using the Minitab software. A 3-point bending test was, thereafter, performed according to ASTM D 790 - 2 test standard specifications.

2.2 Finite Element Analysis of Flexural Properties of Composites

A finite element analysis was formulated for modeling the mono and hybrid nanocomposites, and also to obtain their flexural properties using ABAQUS software. The quad-dominated element shape was employed as it not only uses quadrilateral elements but also allows triangles in transition regions. ABAQUS software was preferred as it allows the computation of accurate eigenvalues and eigenvectors at the nodes.

The following values shown in Table 1, which were obtained experimentally, were used to create the material definition.

Table 1: Material definition for composite constituents (Source: experimental data)

Property/Material	Sisal Nanofibre	Rice husk nanoparticle	Epoxy Resin
E1 (MPa)	18000	15000	3800
E2 (MPa)	17500	14500	3700
Poisson's ratio	0.1	0.3	0.4
G12 (MPa)	17000	14000	3500
G13 (MPa)	17000	14000	3500
G23 (MPa)	17000	14000	3500

Figures 1 and 2 show the composite models in Abaqus software.

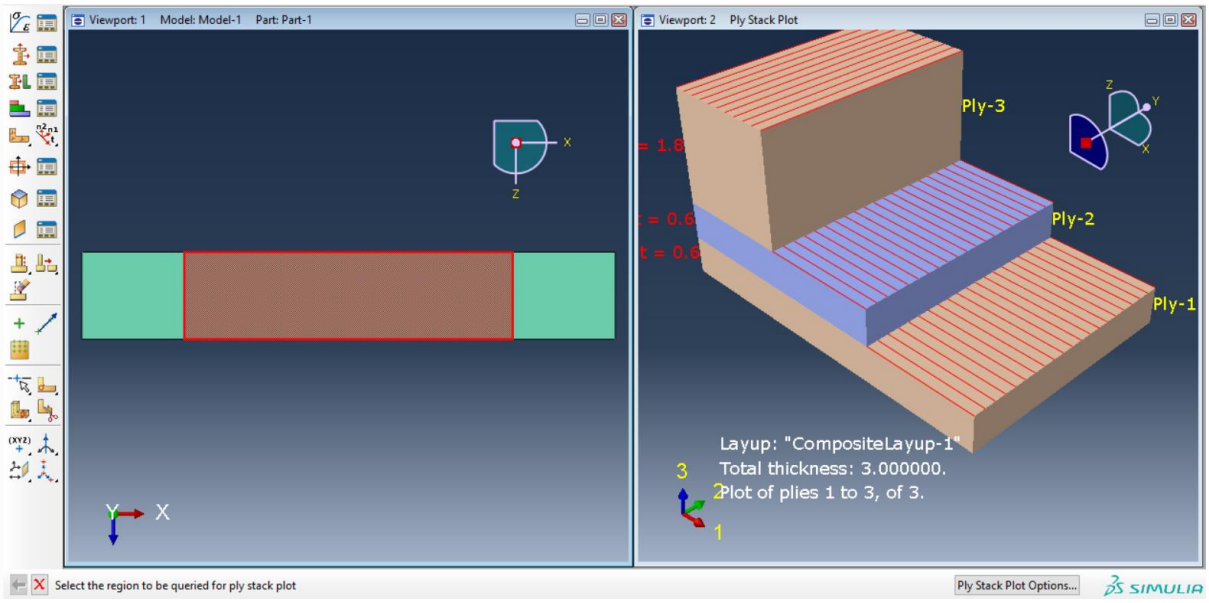

Figure 1: Plystack plot of the composite

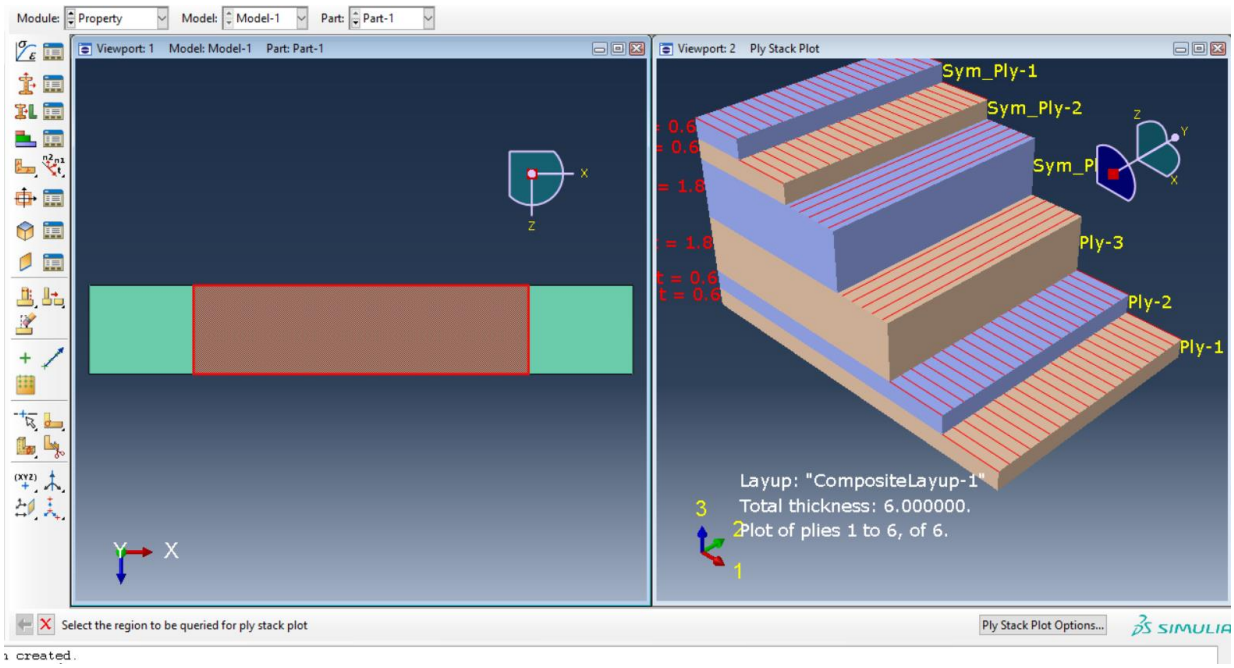

Figure 2: Creation of calculated sections symmetric

As an example of a stress contour plot showing the position and magnitude of flexural strength of 40% sisal/rice husk hybrid reinforced epoxy resin nanocomposites is shown in Figure 3. The maximum principal stress was used for the analysis of the flexural strength. The results were read at a 75% average default setting.

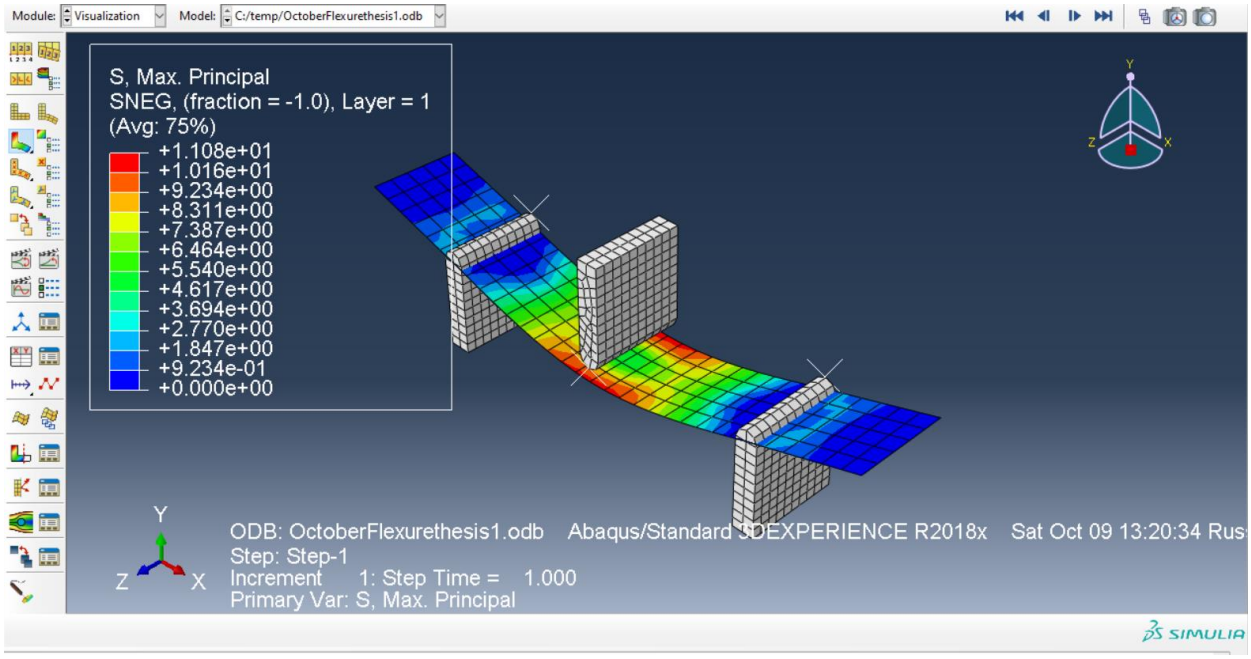

Figure 3: Display of results

3.0 FLEXURAL STRENGTH RESULTS

The flexural strength values were obtained from the peak loads recorded from the 3 point bending tests. The flexural strength for both the mono and hybrid composites are presented hereunder. These results were determined using both the numerical and experimental approaches.

3.1 Results of Flexural Strength for Sisal Nanofibre Reinforced Epoxy Resin Composites

The flexural strength results for sisal nanofibre reinforced epoxy resin composites, which were obtained using the methods presented in section 2.0, are shown in Table 2.

Table 2: Flexural strength values for sisal nanofibre reinforced epoxy resin Composites

Fibre Volume Fraction (υf %)	FEA Results (MPa)	Experimental Results Average value (MPa)
0.000	2.543	2.646±0.251
1.672	4.405	3.924±0.455
2.691	5.299	4.962±0.549
3.355	6.210	5.346±0.532
4.711	7.696	6.444±0.613
5.754	8.046	7.189±0.522
6.750	8.345	7.524±0.550
7.783	8.549	8.285±0.525
8.516	9.702	8.494±0.714
9.505	9.017	8.610±0.988
11.200	7.991	7.810±0.540

The experimental results show that the flexural strength increased with the reinforcement volume fraction starting from a value of 2.646 MPa for unreinforced specimens to a maximum flexural strength of 8.610 MPa at a reinforcement volume fraction of 9.505%. The finite element analysis results show that the highest and lowest values of flexural strength were obtained as 9.702 MPa and 2.543 MPa, respectively.

The increments of experimental results of flexural strengths over the values obtained for the unreinforced matrix were 48.30%, 87.53%, 143.54%, 171.69% and 195.16% at fibre contents of 1.67 υ_f%, 2.69 υ_f%, 4.71 υ_f%, 5.75 υ_f%, and 11.2 υ_f%, respectively.

The increments in finite element analysis results over the values obtained for the unreinforced matrix were 73.22%, 108.38%, 202.63%, 216.40% and 214.24%, respectively, at the same fibre volume fractions as those for the experimental results.

The standard deviations recorded in Table 2 at all fibre fractions for the experimental results were found to be very low, ranging from 0.251 to 0.714. However, the variations between specimens at a given fibre volume fraction was found to be larger for fibre reinforced specimens than in unreinforced test pieces. This can be attributed to the difficulty in achieving the same uniform distribution and orientation of fibres.

3.1.1 Comparison of Finite Element Analysis and Experimental Results of Flexural Strength for Sisal Nanofibre Reinforced Epoxy Resin Composites

Figure 4 shows a comparison of the results obtained from both the finite element analysis (FEA) and experimental approaches.

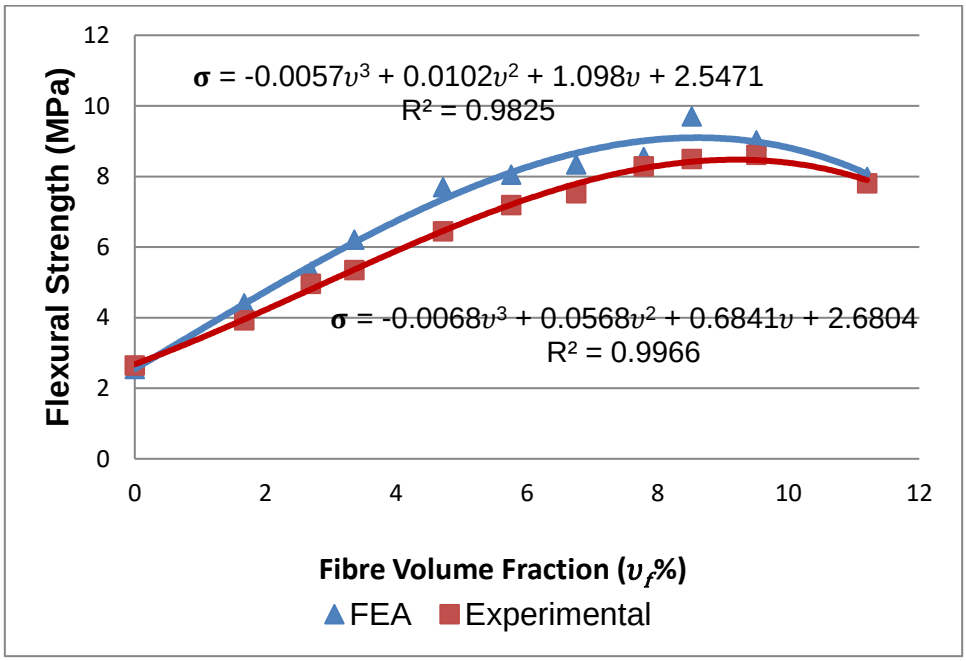

Figure 4: A graph of fibre volume fraction versus flexural strength for sisal nanofibre-reinforced epoxy resin composite

It can be seen from Figure 4 that for the experimental results, the rate of increase of flexural strength with fibre volume fraction is fairly rapid initially up to fibre content of about 6.8 υf%, thereafter, the rate of increase reduces with fibre additions up to the maximum strength, corresponding to 9.5 υ_f% fibre content. For the FEA results, a steady increase in flexural strength was observed up to the optimal point. The FEA results gave the optimal flexural strength at around 9 υ_f% fibre volume fraction, corresponding to around 9.8

MPa. The coefficient of correlation shown in the graphs (0.9825 and 0.9966) for both the FEA and experimental results were found to be closer to 1, implying a perfect fit of the data set.

3.1.2 Validation of Finite Element Analysis Results of Flexural Strength for Sisal Nanofibre Reinforced Epoxy Resin Composites

The FEA results of sisal nanofibre reinforced epoxy resin composites were validated by computing the percentage errors between them and the experimental results, as shown in Table 3.

Table 3: Error margin of experimental and FEA results

Fibre Volume Fraction (%)	FEA	EXPERIMENTAL	%ERROR
0.000	2.543	2.646	-3.893
1.672	4.405	3.924	12.258
2.691	5.299	4.962	6.792
3.355	6.210	5.346	16.162
4.711	7.696	6.444	19.429
5.754	8.046	7.189	11.921
6.750	8.345	7.524	10.912
7.783	8.549	8.285	3.186
8.516	9.702	8.494	14.222
9.505	9.017	8.610	4.727
11.200	7.991	7.810	2.318

It can be seen from Table 3 that the deviation between experimental and FEA results is insignificant and in close agreement for 36.36% of the results since the margin of error is within the acceptable engineering percentage error limit of ±5%.

3.2 Results of Flexural Strength for Rice Husk Nanoparticle Reinforced Epoxy Resin Composites

The results of flexural strength for rice husk nanoparticles reinforced epoxy resin composite specimens are shown in Table 4.

Table 4 Flexural strength values for rice husk nanoparticle reinforced epoxy resin composites

Fibre volume fraction (υf%)	FEA (MPa)	Experimental (MPa)
0.000	2.543	2.646±0.251
1.672	3.145	2.939±0.247
2.691	3.955	3.849±0.141
3.355	4.226	4.079±0.212
4.711	4.106	4.317±0.190
5.754	3.894	4.568±0.232
6.750	3.799	4.762±0.222
7.783	3.689	4.898±0.210
8.516	3.581	4.923±0.155
9.505	3.436	4.156±0.225
11.200	3.391	3.572±0.241

A Maximum value of 4.923 MPa was obtained for the flexural strength at the fibre content of 8.516 υ_f%. The flexural strength of unreinforced epoxy specimens was obtained as 2.646 MPa. Furthermore, results from Table 4 show that the increments of experimental flexural strength values for rice husk nanoparticle reinforced-epoxy resin composites over the values obtained for the unreinforced specimens were: 11.07%, 5.83%, 4.25% and 0.51% at fibre contents of 1.672 υ_f%, 4.711 υ_f%, 6.750 υ_f%, and 8.516 υ_f%, respectively. Standard deviations for all fibre volume fractions were found to be very low, with the lowest value being recorded at 2.691 υ_f%. This low standard deviation implies that there was no much scatter in the data set. However, the variations between specimens at a given fibre volume fraction was found to be larger for fibre reinforced specimens than in unreinforced test pieces. This can be attributed to the difficulty in achieving the same uniform distribution and orientation of fibres.

3.2.1 Comparison of Finite Element Analysis and Experimental Results of Flexural Strength for Rice Husk Nanoparticle Reinforced Epoxy Resin Composites

Figure 5 shows the results obtained from both the experimental and finite element analysis approach for rice husk nanoparticle reinforced epoxy resin composites

.

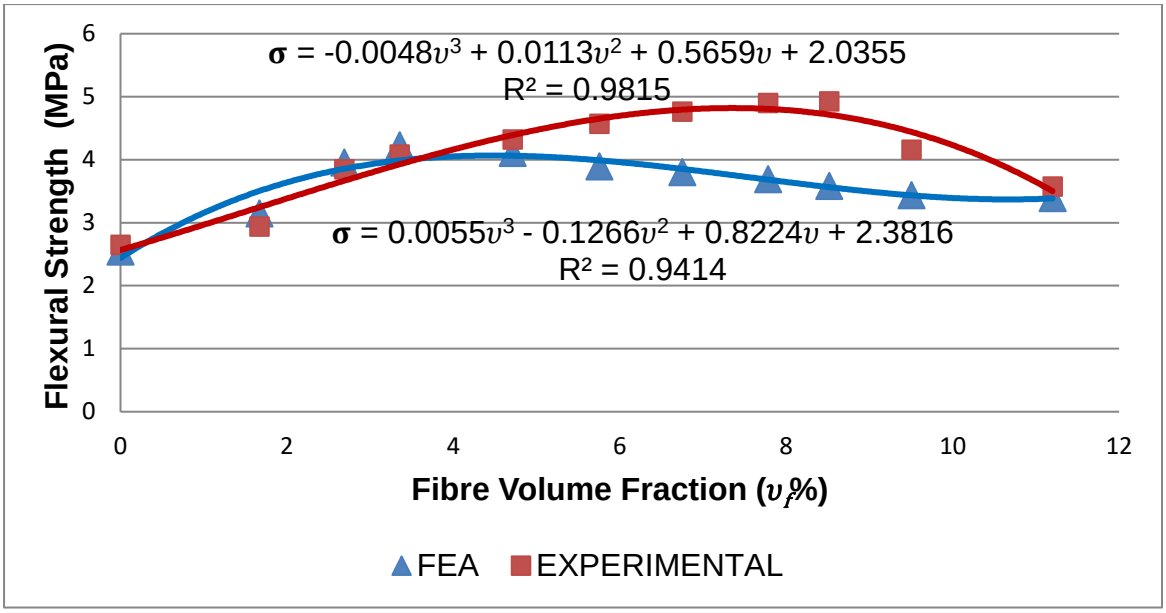

Figure 5: A graph of fibre volume fraction versus flexural strength for rice husk nanoparticle reinforced epoxy resin composites

It can be seen from Figure 5 that for the experimental results, the rate of increase of flexural strength with fibre volume fraction is fairly rapid initially up to fibre content of about 7.8 υ_f%, then the rate of increase reduces with fibre additions. For the FEA results, a steady increase in flexural strength was observed up to fibre content of about 3.5 υ_f%, beyond which there was a reduction in flexural strength. It is also evident that the FEA plot and the experimental plot intersect at around 3.6 υ_f%, with the corresponding flexural strength being 4 MPa. The coefficients of correlation shown in the graphs (0.9815 and 0.9414) are closer to 1, implying a perfect data set fit.

3.2.2 Validation of Finite Element Analysis Results of Flexural Strength for Rice Husk Nanoparticle Reinforced Epoxy Resin Composites

The experimental results of rice husk nanoparticle reinforced epoxy resin composites were used as the reference in order to validate the FEA results. This was done by computing

the percentage errors between them and the FEA results, as shown in Table 5.

Table 5: Error Margin between FEA and Experimental Results

Fibre volume fraction (*υ*f%)	FEA (MPa)	Experimental (MPa)	Error (%)
0.000	2.543	2.646	-3.893
1.672	3.145	2.939	7.009
2.691	3.955	3.849	2.754
3.355	4.226	4.079	3.604
4.711	4.106	4.317	-4.888
5.754	3.894	4.568	-14.755
6.750	3.799	4.762	-20.223
7.783	3.689	4.898	-24.684
8.516	3.581	4.923	-27.260
9.505	3.436	4.156	-17.324
11.200	3.391	3.572	-5.067

It is evident from Table 6 that the deviation between experimental and FEA results are in close agreement for 45.45% of the values recorded since their error values are within the acceptable engineering percentage of errors of ±5%. The other 54.55% of the experimental results have errors which are significant since their margin of error is outside the acceptable engineering percentage of error of ±5%. These deviations can be attributed to fibre bunching in some instances. Similar observations were noted by Bisanda (2000).

3.2.3 Results of Flexural Strength for Sisal/Rice Husk Hybrid Reinforced Epoxy Resin Nanocomposites.

Table 6 shows flexural strength results which were obtained from sisal/rice husk hybrid reinforced epoxy resin nanocomposites.

Table 6: Flexural strength values for sisal/rice husk hybrid reinforced epoxy resin nanocomposite

Fibre volume fraction (*υ*f%)	FEA (MPa)	Flexural Strength (MPa)
0.000	2.543	2.646±0.050
1.672	10.790	9.603±0.075
2.691	11.930	10.392±0.065
3.355	12.610	12.237±0.040
4.711	13.490	12.951±0.035
5.754	15.090	13.704±0.045
6.750	14.620	14.286±0.035
7.783	14.080	14.694±0.065
8.516	13.550	14.769±0.050
9.505	12.840	12.468±0.050
11.200	12.620	10.716±0.035

A Maximum value of 14.769 MPa was obtained for the flexural strength at 8.516 υ_f%. It was also evident that in the FEA results, the increase in flexural strength over the values for the unreinforced specimens were 369.13%, 493.39%, 404.92% and 396.26% at 2.691 υ_f%, 5.754 υ_f%, 9.505 υ_f% and 11.200 υ_f%, respectively. The corresponding increments for the experimental results at the same fibre

volume fractions were 292.74%, 417.91%, 371.20% and 304.99%, respectively.

3.2.4 Comparison of Experimental and Finite Element Analysis Results of Flexural Strength for Sisal/Rice Husk Hybrid Reinforced Nanocomposites

A graph of flexural strength versus fibre volume fraction of sisal/rice husk hybrid reinforced epoxy resin nanocomposites showing both experimental and finite element analysis (FEA) results is presented in Figure 6 hereunder.

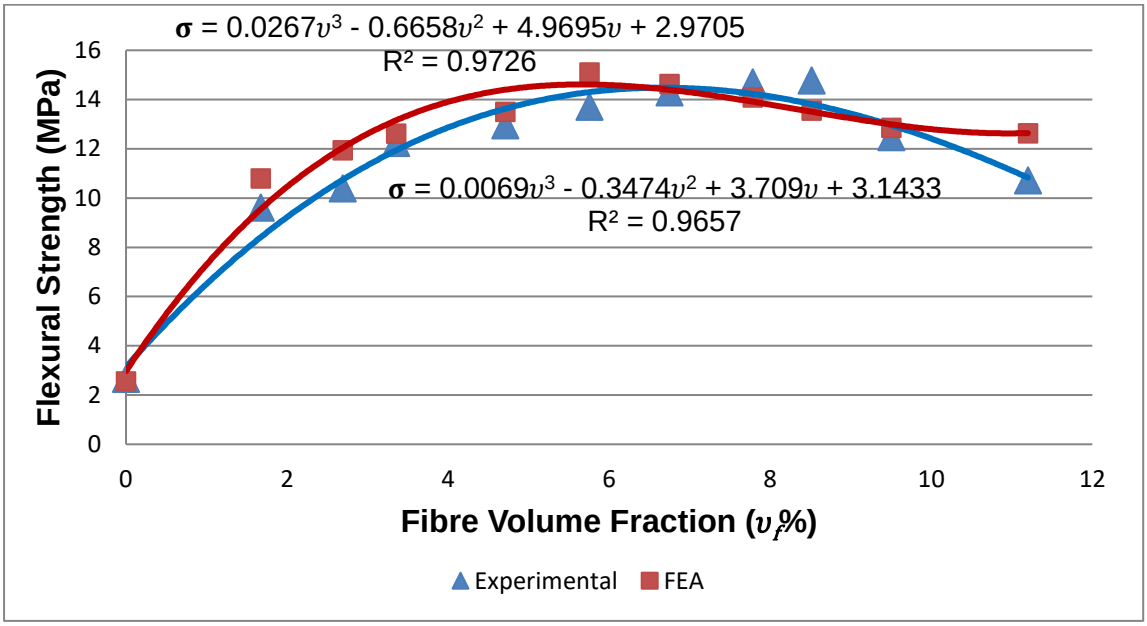

Figure 6: A graph of fibre volume fraction versus flexural strength for sisal/rice husk hybrid reinforced epoxy resin nanocomposites

experimental and FEA approaches. In the experimental approach, it is evident that the optimum flexural strength of sisal/rice husk hybrid reinforced-epoxy resin nanocomposites was realized at around 7 υ_f%. Beyond these optimum values of reinforcement volume fraction, the flexural strength began to fall gradually with fibre additions. The rate of increase of flexural strength with fibre contents decreased at higher fibre volume fractions, as can be depicted in Figure 6.

In the FEA approach, it is evident that there is a steady increase in the flexural strength up to the optimum point. The optimum point is at around 5.8 υ_f%. Beyond this optimum point, the flexural strength begins to reduce with an increase in fibre additions.

It is also evident that both the FEA and the experimental plots intersect at around 6.5 υ_f% and 9.6υ_f%. The coefficient correlation of both the FEA and the experimental plot (0.9726 and 0.9657), as seen in Figure 6, is closer to 1, implying a perfect fit of the data set.

3.2.5 Validation of Finite Element Analysis Results of Flexural Strength for Sisal/Rice Husk

Hybrid Reinforced Epoxy Resin Nanocomposites

The FEA results of sisal/rice husk hybrid reinforced epoxy resin nanocomposites were validated by computing the percentage errors between them and the experimental results, as shown in Table 7.

Table 7: Error Margin of FEA and Experimental Results

Fibre volume fraction (%)	FEA (MPa)	Experimental (MPa)	% Error
0.000	2.543	2.646	-3.893
1.672	10.79	9.603	12.361
2.691	11.93	10.392	14.800
3.355	12.61	12.237	3.048
4.711	13.49	12.951	4.162
5.754	15.09	13.704	10.114
6.750	14.62	14.286	2.338
7.783	14.08	14.694	-4.179
8.516	13.55	14.769	-8.254
9.505	12.84	12.468	2.984
11.200	12.62	10.716	17.768

It can be seen from Table 7 that the deviation between FEA and experimental results is insignificant and are in close agreement for 54.55% of the results since the margin of error is within the acceptable engineering percentage of error of ±5%.

3.2.6 Comparison of Flexural Strength of Mono and Hybrid Nanocomposites

Figure 7 compares the flexural strength of sisal nanofibre reinforced epoxy resin composites, rice husk nanoparticle reinforced epoxy resin composites and sisal/rice husk hybrid reinforced epoxy resin nanocomposite.

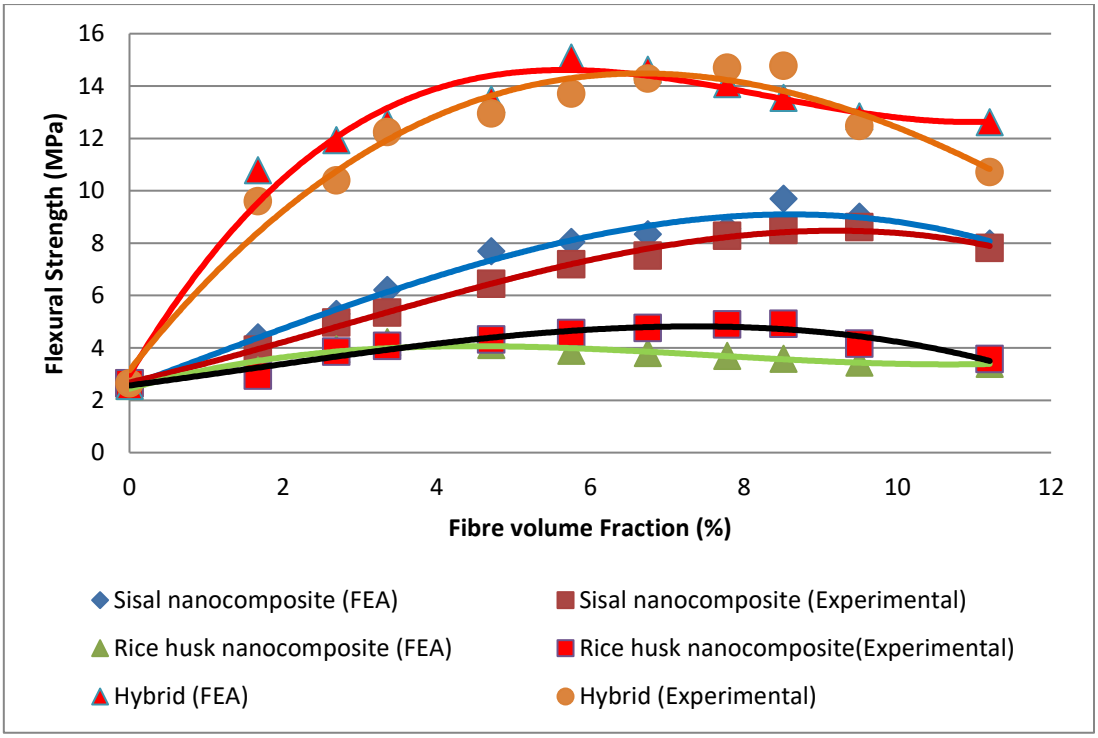

Figure 7: Comparison of flexural strength of mono and hybrid composition

From the graph in Figure 7, it is clear that sisal/rice husk hybrid reinforced epoxy resin nanocomposite had the highest values of flexural strength. This was followed by sisal nanofibre reinforced epoxy resin composites and, finally, rice husk nanoparticle reinforced epoxy resin composites. It is also evident that the Flexural strength of sisal/ rice husk hybrid reinforced epoxy resin nanocomposite is almost twice as much as the flexural strength of sisal nanofibre reinforced epoxy resin composites and rice husk nanoparticle reinforced epoxy resin composites. The better performance of hybrid composites than the monocomposites can be attributed to a bigger increase in the fibre loading in the hybrid composites than in the monocomposites.

3.2.7 Analysis of Variance for Flexural Strength

Table 8 shows a summary of variances of the mono and hybrid composites under experimental and the FEA approaches, whereas Table 9 shows the analysis of variance between and within groups.

Table 8: Summary of Variances within the Mono and Hybrid Groups

SUMMARY				
Groups	Count	Sum	Average	Variance
Sisal nanofibre reinforced epoxy resin composites(Experimental))	11	77.803	7.073	4.820
Sisal nanoparticle reinforced epoxy resin composites (FEA)	11	71.234	6.476	4.004
Rice husk nanoparticle reinforced epoxy resin composites(Experimental)	11	39.765	3.615	0.231

Rice husk nanoparticle reinforced epoxy resin composites (FEA)	11	44.709	4.064	0.581
Hybrid(Experimental)	11	134.163	12.197	11.730
Hybrid(FEA)	11	128.466	11.679	12.058

Table 9: Analysis of Variance between Groups and within Groups

ANOVA						
Source of Variation	SS	df	MS	F	P-value	F crit
Between Groups	744.104	5	148.820	26.7164	4.22E-14	2.368
Within Groups	334.223	60	5.571			
Total	1078.327	65				

It is evident from the results presented in Table 8, that the sisal/rice husk hybrid reinforced epoxy resin nanocomposite done using the FEA approach had the highest variance of 12.058 while the rice husk nanoparticle reinforced epoxy resin composites done using the experimental approach had the lowest value of the variance of 0.231. Furthermore, it is evident from Table 9 that the variability between the groups was 744.104, while the variability within the groups was 334.223. Moreover, The F statistic test and p statistic test indicate that these tests are significant. It is also evident that the difference between the means of the six groups is deemed significant since $F_{stat.} > F_{critical}$

4.0 DISCUSSION

4.1 Fibre Volume Fraction Effects on Flexural Strength

The general trend in both the FEA and experimental approach is shown in Figures 4, 5 and 6, which shows that there is a steady increase in the rate of flexural strength between 0 υ_f% and the optimal points. After the optimal points, there was a reduction in the rate of increase of flexural strength with fibre additions.

During the flexural strength testing, the specimens were seen to fail with a single crack traversing through the neutral axis. After the crack appeared, the load started decreasing progressively, with more fibres pulling out of the matrix. As loading continued, the crack widened, exposing more fibres.

An increase in flexural strength with increasing fibre contents was observed as shown in Figures 4, 5 and 6 for both the FEA and the experimental results.

When sisal nanofibres, rice husk nanoparticles and sisal/rice husk hybrid were used as reinforcement, it was found that there was a limit beyond which fibre additions did not improve the strength of the composites. This limit occurred at 9 5 υ_f%, and 8.5 υ_f% in the experimental and FEA approaches, respectively, in sisal nanofibres. In rice husk nanoparticles, this limit occurred at around 7.8 υ_f%, and 3.4 υ_f% in experimental and FEA approaches, respectively. In sisal/rice husk hybrid reinforced epoxy resin nanocomposites, these limits occurred at around 7 υ_f% in both the experimental and FEA approaches. This apparent loss in strength beyond a certain volume fraction can be ascribed to a number of factors such as:

- Poor compaction at high fibre volume fractions is a result of an increase in the number of voids in the composites, especially as the mixture becomes

more and more unworkable. This results in lowering the fibre/matrix adhesion and, consequently, the composite strength (Bisanda, 2000;)

- In the case of hybrid composites, the balling-up and curling of fibres increased with an increase in fibre contents.

These two phenomena could have resulted in the formation of more voids and eventually decreased the fibre/matrix adhesion.

The increase in flexural strength with increasing volume fractions points out that fibre lengths used are greater than the optimal fibre length 'lc'. This aspect of optimal fibre length was deduced from the work of Kelly (2016), which explained that if the fibre length is the same or more than the optimal fibre length, then complete stress transfer between the fibre and matrix takes place. However, for fibres shorter than the optimal fibre length, failure is by pull-out and the full potential of fibres as a reinforcement is not realised.

The initial low flexural strength recorded at low fibre volume fractions (between 0 υ_f, and 1 υ_f%) can be explained from the concept of critical fibre volume fraction concluded by Argon and Shack (2012), where it was pointed out that in order to obtain any benefit from the reinforcing fibres, the critical fibre volume fraction must be exceeded. It is only after this condition has been met that fibre strengthening of the composite can occur. Majumdar (2008), established the critical fibre volume fractions of some common fibres as follows: glass (0.1-0.2 υ_f%), graphite (0.2-0.3 υ_f%), steel (0.2-0.5 υ_f%), polypropylene (1 υ_f%) and polycrystalline alumina (0.8 υ_f%). Above 1 υ_f%, there is a steady increase in flexural strength property, which suggests a stronger fibre/matrix bond strength due to a greater length of embedment.

It was observed that the hybrid nanocomposites produced higher flexural strengths than the monocomposite specimens in both the experimental and FEA approaches. The higher flexural strength of hybrid composites can be attributed to the fact that the hybrid composite (sisal/rice husk hybrid reinforced-epoxy resin nanocomposite) had higher aspect ratios than the monocomposites (sisal nanofibre reinforced epoxy resin composites), and that the rice husk nanoparticle reinforced the epoxy resin composite. The present results also agree well with the predictions of Swift and Smith (1979), who pointed out that a substantial increase in flexural strengths of composites can only be achieved by suitable choices of fibre length, mix ratio and incorporation techniques.

Upon comparing the FEA results with experimental flexural results (see Table 4, 6 and 8), it was established that the margins of errors of 36.36% of the results obtained from the sisal nanofibre reinforced epoxy resin composites were within the acceptable engineering percentage of error of ±5%. For the rice husk nanoparticle reinforced epoxy resin composites, 45.45% of the results were within the acceptable engineering error of ±5%. For the sisal/rice husk hybrid reinforced epoxy resin nanocomposites, 54.55% of the results were within the acceptable margin of error of ±5%. The deviations noted in the results could be attributed to the differences in the accuracy levels of the two methods. The experimental method has uncertainties that usually arise during procedural setups, such as the inherent differences between the presence and orientation of fibres (Bisanda, 2000). The FEA method gives approximate results since it considers the effects of non-linearities common in the fabrication of composites.

5.0 CONCLUSIONS

For the experimental approach of sisal nanofibre reinforced epoxy resin composites, the rate of increase of flexural strength with fibre volume fraction is fairly rapid initially up to fibre content of about 6.8 υ_f%, thereafter, the rate of increase reduces with fibre additions up to the maximum strength, corresponding to 9.5 υ_f% fibre content.

For the FEA approach of sisal nanofibre reinforced epoxy resin composites, a steady increase in flexural strength was observed up to the optimal point. The FEA results gave the optimal flexural strength at around 9 υ_f% fibre

volume fraction, corresponding to around 9.8 MPa.

For sisal nanofibre reinforced epoxy resin composites, the coefficient of correlation (0.9825 and 0.9966) for both the FEA and experimental results were found to be closer to 1, implying a perfect fit of the data set.

For the experimental approach of rice husk nanoparticle reinforced epoxy resin composites, the rate of increase of flexural strength with fibre volume fraction is fairly rapid initially up to fibre content of about 7.8 υ_f%, then the rate of increase reduces with fibre additions.

For the FEA approach of rice husk nanoparticle reinforced epoxy resin composites, a steady increase in flexural strength was observed up to fibre content of about 3.5 υ_f%, beyond which there was a reduction in flexural strength.

For the rice husk nanoparticle reinforced epoxy resin composites, both the FEA plot and the experimental plot intersect at around 3.6 υ_f%, with the corresponding flexural strength being 4 MPa.

For the experimental approach of sisal/rice husk hybrid reinforced-epoxy resin nanocomposites, the optimum flexural strength was realized at around 7 υ_f%. Beyond these optimum values of reinforcement volume fraction, the flexural strength began to fall gradually with fibre additions. The rate of increase of flexural strength with fibre contents decreased at higher fibre volume fractions.

In the FEA approach of sisal/rice husk hybrid reinforced epoxy resin nanocomposites, it was evident that there was a steady increase in the flexural strength up to the optimum point. The optimum point is at around 5.8 υ_f%. Beyond this optimum point, the flexural strength begins to reduce with an increase in fibre additions.

There was evidence that both the FEA and the experimental plots intersect at around 6.5 υ_f% and 9.6 υ_f% in the hybrid composites.

The hybrid composites depicted higher flexural performance than the monocomposites.

6.0 DECLARATIONS

6.1 Availability of data and Material

All data generated or analysed during this study are included in this published article.

6.2 Conflict of Interests

The authors have no conflict of interest to declare

7.0 REFERENCES

Akbar Tabar I, Emami M. Investigation of Mechanical Behavior of Hemp / Polyester Hybrid Polymer Background Composite Field. 11th National Conference on Textile Engineering of Iran. Iran, 2018.

Argon, A.S. and Shack, W.J. 2012. Theories of fibre cement and fibre concrete. Rilem Symposium on Fibre Reinforced Cement and Concrete, U.K, 39-52.

Bay, Mohammad Ali, Khademieslam Habibollah, Bazyar Behzad,, Najafi Abdollah and Hemmasi Amir Hooman. "Mechanical and Thermal Properties of Nanocomposite Films Made of Polyvinyl Alcohol/Nanofiber Cellulose and Nanosilicon Dioxide using Ultrasonic Method." International Journal of Nanoscience and Nanotechnology 17.2 (2021): 65-76.

Bisanda, E.T.N. 2000. The effect of alkali treatment on the adhesion characteristics of sisal fibres. Journal of Composite Science and Technology.7:331-339.

Börjesson, M., Sahlin, K., Bernin, D., & Westman, G. (2018). Increased thermal stability of nanocellulose composites by functionalization of the sulfate groups on cellulose nanocrystals with azetidinium ions. *Journal of Applied Polymer Science*, 135(10), 45963.

Dharmin, P., Khushbu, P. and Chetan, J. 2012. A Review on stress analysis of an infinite plate. International Journal of Scientific and Research Publications, 2(11):1–7.

El-Feky Mohammed Samy, Youssef Passant, El-Tair Ahmed Maher, Ibrahim Sara and Serag Mohamed.2019. "Effect of nano silica addition on enhancing the performance of cement composites reinforced with nano cellulose fibers." AIMS Materials Science 6.6 (2019): 864-883.

Farooq, Amjad., Patoary, Kayes Mohammed., Zhang, Meiling., Mussana, Hassan., Li, Mengmeng., Naim, Awais Muhammad., Mushtaq, Muhammad. Farooq, Aamir. And Liu, Lifang. "Cellulose from sources to nanocellulose and an overview of synthesis and properties of nanocellulose/zinc oxide nanocomposite materials." International journal of biological macromolecules 154 (2020): 1050-1073.

Ismail, Mostafa Y., Patanen Mina, Sirvio Juho Antti, Visanko Miika, Ohigashi Takuji, Kosugi Nobuhiro, Huttula Marko and Limatainen Henrikki. "Hybrid films of cellulose nanofibrils, chitosan and nano-silica—Structural, thermal, optical, and mechanical properties." Carbohydrate polymers 218 (2019): 87-94.

Jaafar, CN Aiza, Zainol, I., Ishak, N.S. and Ilyas, R.A. "Effects of the liquid natural rubber (LNR) on mechanical properties and microstructure of epoxy/silica/kenaf hybrid composite for potential automotive applications." Journal of Materials Research and Technology 12 (2021): 1026-1038.

Kelly, A. and Zweben, C.2016. Determination of fibre size distributions of injection moulded polypropylene/natural fibres using x-ray microtomography. Journal of Advanced Engineering Material, 10(1-2):126-130.

Kharat, A. and Kulkarni, V. 2013. Stress concentration at openings in pressure vessels–A 105 Review. International Journal of Innovation Resource, Science, Engineering and Technology, 2(3):670–678.

Kihiu, J. and Masu, L. 1995. The effect of chamfer and size on the stress distributions in a thick-walled cylinder with a cross bore under internal pressure, Jomo Kenyatta University of Agriculture and Technology. Digital Repository, 2(2):73–78.

Liimatainen, H., Ezekiel, N., Sliz, R., Ohenoja, K., Sirviö, J. A., Berglund, L., ... Niinimäki, J. (2013). High-strength nanocellulose–Talc hybrid barrier films. *ACS Applied Materials & Interfaces*, 5(24), 13412–13418.

Majumdar, A.J. 2008. Properties of fibre cement composites. Rilem Symposium on Fibre Reinforced Cement and Concrete, 279-314.

Manral A, Bajpai PK. Static and dynamic mechanical analysis of geometrically different kenaf/PLA green composite laminates. Polym Compos 2020;41 (2):691–706.

Masu, L.M. 1991. Cross bore geometry effects on the strength of pressure vessels. Proceedings of the International Conference on Mechanics of Solids and Structures, Nayang Technological niversity, Singapore, 261–272.

Moradi E, Zeinedini A, Heidari-Shahmaleki E. Mechanical properties of laminated composites reinforced by natural fibers of cotton, wool and kenaf under tensile, flexural and shear loadings. J Sci Technol Compos 2019;6:99–108.

Nia, Marzieh Heidari, Tavakolian Mandana, Kiasat Reza Ali and Van de ven G.M Theo. "Hybrid aerogel nanocomposite of dendritic colloidal silica and hairy

nanocellulose: an effective dye adsorbent." Langmuir 36.40 (2020): 11963-11974.

Nziu, P.K. 2018, Optimal Geometric Configuration of a Cross Bore in High-Pressure Vessels. In Doctorate Thesis, Vaal University of Technology.

Oksman, K., Aitomäki, Y., Mathew, A. P., Siqueira, G., Zhou, Q., Butylina, S., Hooshmand, S. (2016). Review of the recent developments in cellulose nanocomposite processing. Composites Part A, Applied Science and Manufacturing, 83, 2–18.

Qadir, M., and Redekop, D. 2009. SCF analysis of a pressurized vessel–nozzle intersection with wall thinning damage. International Journal of Pressure Vessels and Piping, 86(8):541–549.

Suhot, Mohamed Azlan, Hassan, Mohamad Zaki., Aziz, Sa'ardin Abdul and Md Daud, Mohd Yusof "Recent Progress of Rice Husk Reinforced Polymer Composites: A Review." Polymers 13.15 (2021): 2391.

Swift, D.G and Smith, R.B.L. 1979. Cement-based composites. Composites, 145-148.

Zhang, Q., Wang, Z.W., Tang, C.Y., Hu, D.P., Liu, P.Q., and Xia, L.Z. 2012. Analytical solution of the thermo-mechanical stresses in a multilayered composite pressure vessel considering the influence of the closed ends, International Journal of Pressure Vessels and Piping, 98:102–110.

CONSTITUTIVE PARAMETERS ELASTOPLASTIC MODEL FOR SHELLED MAIZE *EN MASSE*

E. Oranga[1*]

[1]PhD Candidate, Department of Environmental and Biosystems Engineering, University of Nairobi, P.O Box 30197-00100, Nairobi, Kenya;

Corresponding author*: *oranga@logassociates.com*

Publication Date: March 2023

ABSTRACT:

Granular materials are some of the most important form of engineering materials in the world. Agricultural cereals including cereal maize continue to be some of the most important crops in the world both for human and livestock consumption. Bulk harvesting, transportation, handling and processing of these crops is therefore important if the increasing global demand is to be met. The use of existing constitutive models for granular engineering materials would greatly help in accurate prediction of the behaviour of shelled maize *en masse*. This paper investigates the engineering properties of three varieties of shelled bulk maize pertinent to grain handling, storage and processing. In particular, it investigates the stress-strain properties of bulk maize using the Lade's elastoplastic constitutive model developed for cohesionless sand. Stress-strain characteristics of three varieties of bulk maize were determined at 12% moisture content (wet basis), using the triaxial equipment and the Senstar Universal Testing (SUT) machine. Three different initial bulk densities (IBD) of 730 kg/m^3, 768 kg/m^3 and 800 kg/m^3 under three levels of confining stresses of 100 kPa, 200 kPa and 300 kPa were used with the triaxial tests while two different initial bulk densities of 730 kg/m^3 and 800 kg/m^3 were used with the senstar testing machine under cyclic uniaxial isotropic loading. Both sets of tests were conducted at an axial strain rate (ASR) of 1.3 mm/min and data recorded after every 30 seconds for the SUT and after every 60 seconds for triaxial loading. The triaxial loading tests were continued until failure or until 20% deformation (whichever came first) while the SUT tests were conducted until 20% deformation. Results were verified and validated using data obtained from twenty-seven (27) different tests of the three maize varieties. The comparison between the measured and the calculated values under Lade's model gave coefficient of determination (R^2) values of 0.95, 0.94 and 0.93 for the three maize varieties (V1, V2 and V3, respectively) indicating that *en masse* maize can be considered as being elastoplastic under this model.

Keywords: *elastoplastic, cohesionless, stress, strain, triaxial, maize, granular*

Notation

B_{ur}	unloading and reloading bulk modulus, kPa
C	collapse modulus, kPa
E	elastic modulus tensor, kPa
E_{ur}	unloading and reloading elastic modulus, kPa
F_C	plastic collapse yield function, dimensionless
F_P	plastic expansive yield function, dimensionless

I_1	first invariant of stress tensor, kPa
I_2	second invariant of stress tensor, kPa
I_3	third invariant of stress tensor, kPa
K	elastic modulus number, dimensionless
K_C	plastic collapse work-hardening function, dimensionless
K_P	plastic expansive work-hardening yield function, dimensionless
P_a	atmospheric pressure, kPa
R, S, t	plastic expansive potential constants, dimensionless
S_{ij}	deviatoric stress, kPa
$\dot{S}_{ij}$	rate of deviatoric stress, kPa/s
S_{ij}^{y}	deviatoric stress reversal point, kPa
S_{ij}^{r}	yield deviatoric stress, kPa
G	elastic shear modulus, kPa
W_C	collapse work, kPa/mm
W_P	expansive work, kPa/mm
W_{ppeak}	expansive work at $f_p = \eta_1$, kPa/mm
e	void ratio, dimensionless
e_{ij}	deviatoric strain, mm mm^{-1}
$\dot{e}_{ij}$	rate of deviatoric strain, mm mm^{-1}s^{-1}
$\left\|\dot{e}_{ij}\right\|$	norm of deviatoric strain rate, mm mm^{-1}s^{-1}
f_c	plastic collapse loading function, dimensionless
f_p	plastic expansive loading function, dimensionless
g_c	plastic collapse potential, dimensionless
g_p	plastic expansive potential, dimensionless
n_{ij}	directional tensor, dimensionless
ν	poisson's ratio, dimensionless
$d\{\varepsilon_{ij}\}$	total strain increment tensor, dimensionless
$d\{\varepsilon_{ij}^{e}\}$	elastic strain increment tensor, dimensionless
$d\{\varepsilon_{ij}^{c}\}$	plastic collapse increment tensor, dimensionless
$d\{\varepsilon_{ij}^{p}\}$	plastic expansive strain increment tensor, dimensionless
$d\{\varepsilon_{r}^{c}\}$	volumetric strain increment, dimensionless
σ_m	mean stress, kPa
$\dot{\sigma}_m$	mean stress rate, kPa/s

η_1	yield constant, dimensionless

Subscripts, superscripts and exponents

a, b, q	intermediate variables
c	collapse yield function
e	base of natural logarithms
ij	plane and direction of stress or strain
m	yield exponent
n	elastic modulus exponent
p	collapse exponent
ur	unloading and reloading moduli
$\alpha, \beta, \theta, \ell$	work hardening constants

1.0 INTRODUCTION

Granular materials are large conglomerations of discrete macroscopic particles that do not quite fit into any of the known phases of matter: solid, liquid, or gas (Heinrich *et al*., 1996). Generally, granular materials are classified based on the particle dimensions and bulk density as follows (Horabik and Molenda, 2016): (a) by particle size; dust D≤0.42mm, grain D ≤3.35mm, lump D ≤40mm, clump D ≤200mm, and block D >200mm; or (b) by bulk density; light ρ<600kg m-3, medium 600kgm-3 < ρ ≤1100kg m-3, heavy, 1100kgm-3 < ρ ≤2000kg m-3 and very heavy, ρ > 2000kg m-3.

The changing personalities of granular materials can have devastating implications, for example the disturbance of the earth following an earthquake can be enough to trigger solid ground to turn to mush with catastrophic consequences. Tordesillas (2004) asserts that, *"Even a fractional advance in our understanding of how granular media behave can have a profound impact on the economic and general well-being of nations worldwide."* Yet, despite being second only to water on the scale of priorities of human activities and believed to account for ten per cent of all energy consumed on earth, the physics behind granular materials remain largely unknown.

Scientists have generally turned to the continuum theory for predicting the behaviours of solids, liquids and granular media (Harris, 2009) – it looks at an object as a whole rather than the sum of its parts. The alternative of modeling every single grain, as in the discrete element method (DEM), is computationally intensive and extremely costly.

Knowledge of constitutive relations in granular agricultural materials is important in transportation, processing and in the design of processing and storage structures such as silos and bins. Jansen's theory, for example, is commonly used in most international standards for silo design (Moya *et al*., 2002). This theory, as well as many others such as Airy's theory or Reimbert's theory considers some material properties such as the angle of internal friction, the grain wall friction coefficient and the specific weight. Hence, it is possible to find values for all these properties in literature to apply in design (Mohsenin, 1980). However, to accurately model silo loads, it is necessary to consider additional material properties not taken into account in the traditional methods (Moya *et al.*, 2002; Vanel *et al.*, 2000). Constitutive models continue to rely on the theory of elasticity to predict the load-deformation behaviour of granular materials (Harris, 2009).

In an attempt to understand this behaviour, previous studies of rheology and strength of agricultural materials have focused on loading specimens to failure at a constant deflection rate or applying impact

loading (Mohsenin, 1980). It is however well known that loading below the yield stress in metals and other composite engineering materials can eventually result in failure (Stinchcomb, 1989). Mclaughlin and Pitt (1984) showed that apple tissue could fail under cyclic or static loadings of magnitudes insufficient to cause failure initially.

Maize is the third most consumed cereal globally, coming only after wheat and rice. Currently, the global maize production stands at over 800 million metric tones, of which 25 percent is consumed directly by human. The rest is converted into livestock feed and other forms. Africa produces just about 7 percent of the global totals while the United States is the major world maize producer (FAO, 2022). In Kenya, maize is the staple food for the majority of the population. The area under maize is estimated 1.6 million hectares (KALRO 2022). Maize production currently stands at about 3.8 million tones against a demand estimated at 4 million tones per year. Demand for maize in Kenya is projected to grow to 7.3 million tones by 2050. As its production and consumption grows in Kenya and around the world, understanding of its bulk property continues to be of importance. This study targeted to help improve our understanding of the constitutive behavior of bulk shelled maize.

1.1 Objectives

The objectives of the study was to evaluate the elastoplastic constitutive parameters for cohessionless shelled maize *en-masse* based on Lade's elastoplastic constitutive model for cohesionless sand and also determine the failure criterion for bulk shelled maize.

1.0 Literature Review

2.1 Micro-to macro description of granular materials

From a microscopic discrete context, knowledge of forces acting on each particle, in bulk granular media, is sufficient to model dynamic and static forces of the system (Stefan, 2001). Tensorial quantities including stress (σ) and strain (ε) are not required for such models. However, in order to establish a correspondence to continuum theories, one has to compute tensorial fields as well as scalar material properties like, bulk and shear moduli. Such properties may then be theoretically averaged from the properties of the individual grains and that of the air occupying the spaces in between in order to establish the bulk behaviour of the granular matter (Latzel *et al.*, 2000a and 2000b). Such an approach, despite being cumbersome, is unreliable especially for agricultural materials (Foutz *et al.*, 1993).

Granular agricultural materials, looked at from the continuum perspective behave uniquely in processing and storage (Gumbe, 1993). This material behaviour varies under different loading conditions, which can be idealized as represented in *Figure. 1*

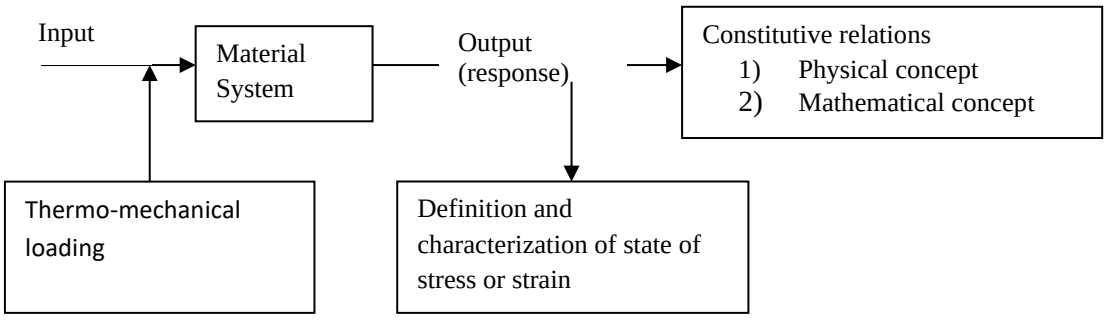

Figure 1: Granular Material Loading System (Gumbe, 1993)

Most studies of the system described in *Fig. 1* focus on the three-dimensional Euclidean space and for most part, the rectangular Cartesian coordinate system. The continuum theory however, regards matter as indefinitely divisible (Chung, 1988). This enables us to study the behaviour of granular material *en masse.*

2.2 Bulk shelled maize as continuous granular matter

Bulk maize storage in bins and silos create engineering and design challenges as the bulk grain is an ecological system in which deterioration results from interaction among physical, chemical and biological variables (Sinha, 1973). These variables seldom act alone or all at once. They usually interact with the grain and in groups, among themselves. Among the physical properties of grain *en-masse* that contribute to the final grain quality in storage include, (Sinha, 1973); grain porosity; which depends on the shape and size of grain, its elasticity and surface state, among others, flow; which refers to the viscous nature of the grains, layering; due to difference in terminal velocities and specific gravity of the grains, sorption; either adsorption, desorption or chemo-sorption, thermo-physical mass exchange properties; such as conductivity, diffusivity, moisture content and bin structure and it's interrelations; which include shape, size, site, construction material, crop type among others.

3.0 Elastoplastic Model and Failure Criterion

3.1 Lades elastoplastic model

The elastoplastic theory developed by Lade (1977) for cohesionless sand and verified for wheat *en masse* by Zhang *et al.* (1986) has the following form;

$$d\varepsilon_{ij} = d\varepsilon_{ij}^{e} + d\varepsilon_{ij}^{p} + d\varepsilon_{ij}^{c} \quad (3.1)$$

Where:

$d\varepsilon_{ij}$ is the total strain increment tensor, and superscripts e, p, and c, refer to the elastic, plastic and plastic collapse strain increment components respectively. The complete elastoplastic constitutive relationship includes an elastic component and two work hardening plastic components. *Fig. 2* shows basic elastoplastic components as described by Lade's model.

$d\varepsilon_{ij}$ is the volumetric strain increment

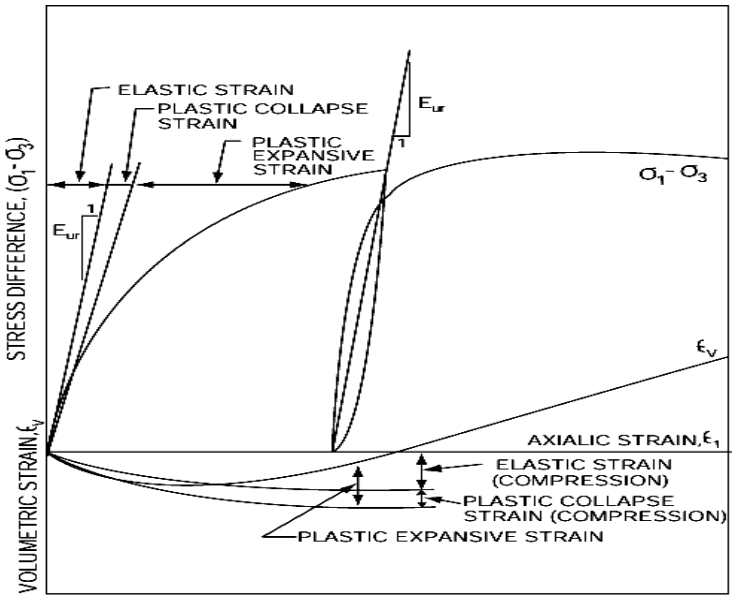

Fig 2: A schematic representation of elastic, plastic collapse and plastic expansive strain components determined in triaxial tests (Lade, 1977).

Lade and Nelson developed a procedure to construct an incremental elastoplastic model with multi-intersecting yield surfaces. By using this Lade-Nelson method Chi and Kushwaha (1990) derived the complete elastoplastic model as presented below;

Lade's complete Elastoplastic Constitutive Equation

The complete elastoplastic stress-strain equation developed by Lade may be written in incremental form as;

$$d\{\sigma\} = [E_{ep}]d\{\varepsilon\} \quad (3.2)$$

The elastoplastic constitutive matrix (3.2) can readily be determined if the stress state is known.

4.0 MATERIALS AND METHODS

4.1 Sample collection and preparation

Three different maize varieties were used in the experiments. Samples for both the triaxial tests and the senstar cyclic loading/unloading and stress relaxation tests were collected from three different field stations in two different climatic regions of Kenya. The Rift Valley region variety referred as (V1) and two varieties from Eastern Kenya, (V2) and (V3). In using these three varieties, the following assumptions were made,

a. The properties of the varieties were representative of the properties of shelled bulk maize available in Kenya.
b. Standard management practices had been applied on the samples both in the field and at post-harvest.
c. The assumptions of isotropy and that of the existence of deviatoric and hydrostatic stresses as proposed by Youngs (1982) applied for the selected grain.

Samples were carefully packaged in 50 kg bags which were properly sealed to avoid any moisture loss or gain during transit and then transported to the testing laboratories at the University of Nairobi. Samples were stored at ambient conditions for a period of 24 hours to reach equilibrium before any tests were conducted (Foutz *et al.*, 1993). The equilibrium moisture content was determined to be $12 \pm 1.5\%$ (w.b.). The relative humidity, which was determined from Mason's wet and dry bulb thermometer, was between 65% and 75% for the duration of the experiments.

4.1.1 Sample preparation for triaxial testing

The moisture content of the samples for the triaxial tests was determined using the oven drying method. The sample size for triaxial testing was 100 mm diameter and 200 mm height (Zhang *et al.*, 1998; Li *et al.*, 1990). Three levels of density were used during the tests. These were, 730 kg/m^3, 768 kg/m^3 and 800 kg/m^3. Higher density samples were obtained by putting the sample on a sieve-shaker for about five minutes (Li *et al.*, 1990) for the intermediate (768 kg/m^3) density and for ten minutes for the higher (800 kg/m^3) density. The lowest density (730 kg/m^3) was obtained by hand-filling the testing cell.

4.1.2 Sample preparation for SUT testing

The three varieties were tested at two different densities of 730 kg/m^3 and 800 kg/m^3. The low-density samples were obtained by carefully hand-filling the testing cell while higher densities were

achieved by placing the sample-filled cell on a sieve shaker and shaking for 10 minutes (Li *et al.*, 1990). The sample size used for the SUT tests was 50 mm in diameter and 150 mm in height. Samples which were prepared and conditioned as described in 4.1 were then used for cyclic loading/unloading experiments and stress relaxation tests as explained in the sections that follow.

4.2 Equipment Description

4.2.1 Triaxial testing equipment

Figure 3 shows a schematic diagram of the triaxial testing equipment used for the triaxial compression loading experiments. Standard triaxial testing procedures proposed by Bishop and Henkel (1957) were modified as suggested by Li *et al.*, (1990) and Zhang *et al.*, (1998) for testing of unsaturated granular agricultural materials.

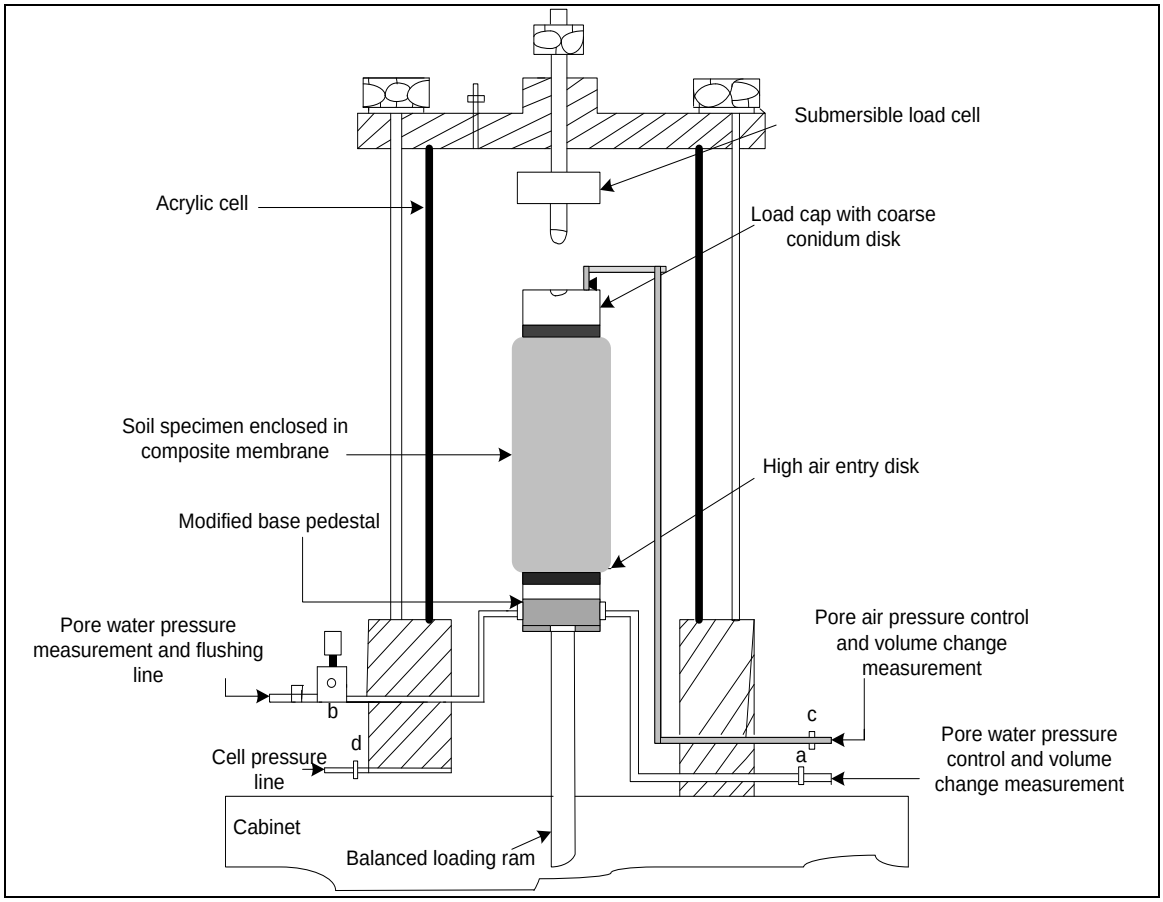

Fig.3: Modified triaxial test device for compression loading

The quantities that were measured during the tests included the stress transmitted by the cell fluid (air), the axial force applied to the loading ram and the change in length of the sample. To control pore pressure, the pore pressure channels were closed throughout the tests. Some of these quantities have been described below.

The following factors determined the choice of confining stress;

(a) the need to create some observable difference between atmospheric pressure and cell pressure so as to avoid running the test under atmospheric conditions

(b) permissible maximum pressure indicated on the acrylic cell

(c) recommended stress values from other researchers such as Zhang *et al.* (1998). Stresses between 100 kPa and 300 kPa were used.

The cell pressure provided the all-round stress on the sample giving the minor principal stress (σ_3). To ensure that a constant minor principal stress was maintained throughout the tests, the cell pressure line shown in Fig. 3 above was connected to a compressor vessel.

Axial stress is the axial force applied to the loading ram depended on the above cell stresses since these had to be overcome during the tests for effective stress to be registered. An area-correction factor used in determining this stress is described in Equation (4.2). *Pore pressure* is the pore pressure in the pore fluid (air, water or both air and water) play an important role in triaxial tests (Wood, 1990). With the assumption of incompressibility of air and in the case of unconsolidated undrained (UU) tests as the one conducted, these pressure channels were closed. The alternative tests i.e. consolidate drained (CD) or the consolidated undrained (CU) tests would require the opening of the channels.

Rate of loading of the samples were guided by, among other factors;

(a) need to maintain quasi-static loading state

(b) need to harmonise both the senstar and the triaxial experiments

(c) other research work on the area including Zhang *et al.* (1998) and Gray (2001)

4.2.2 Senstar universal testing equipment

The equipment used to conduct the cyclic loading and stress relaxation experiments was a 10-ton force Senstar Universal Testing (SUT) machine with an accuracy of 0.001 mm for displacement measurements and 0.1 kgf for load measurements. Due to lack of automation however, the data collected was accurate to 0.1 mm for displacement and 1 kgf for load. A rigid cell of diameter 50 mm and height 150 mm, which had been specifically designed for the uniaxial tests, was used to hold the sample (the dimensions being designed to maintain the recommended height-to-diameter ratio of between 2 and 3). The inner wall of the cell was oiled before every test so as to ensure minimal friction between the grains and the rigid wall.

4.3 Material Testing

4.3.1 Choice of confining stresses and rate of triaxial loading

Confining stresses of 100 kPa, 200 kPa and 300 kPa were used. This range of confining stresses was used by Chi *et al.* (1993) and Wang *et al.* (2002). An axial strain rate (ASR) of 1.3 mm/min was used for the triaxial compression tests. This loading rate conformed to the rate used for the cyclic loading/unloading tests. Furthermore, Zhang *et al.*, (1998) observed that speeds of between 0.5 mm/min and 6 mm/min had no noticeable influence on failure characteristics of Soybean under triaxial loading. Gray (2001) also reported that loading speeds within this range could be considered as quasi-static.

4.3.2 Triaxial tests

All triaxial tests included two stages, isotropic consolidation and axial compression. The purpose of the isotropic consolidation stage was to allow stabilization of volume change (Zhang *et al.*, 1998) and of confining stress. After the isotropic consolidation stage, the vertical loading system was turned on. The axial force was increased by compressing the sample at predetermined displacement rate of 1.3 mm/min until the test was terminated at failure or at an axial strain of 20%, whichever came first. The triaxial test cycle therefore consisted of the following four stages namely consolidation stage, compression stage, shear along an axis and finally failure of the sample

For each applied load, the axial unit strain (ε) was computed by dividing the change in length ($\Delta\ell$) of the specimen, by the initial length (ℓ_0) of the specimen;

$$\varepsilon = \frac{\Delta \ell}{\ell_0} \quad (4.1)$$

Each corresponding cross-sectional area (A) of the specimen was computed from;

$$A = \frac{A_0}{1-\varepsilon} \quad (4.2)$$

Where:

A_0 is the initial cross-sectional area of the specimen.

Each corresponding axial load was determined by multiplying the proving ring dial reading by the proving ring calibration. Finally, each unit axial load was computed by dividing each applied axial load by the corresponding cross-sectional area, for each specimen tested. The mean or equivalent stress, σ_m, was computed from;

$$\sigma_m = (\sigma_1 + 2\sigma_3)/3 \quad (4.3)$$

where:

σ_1, and, σ_3 are the applied axial stress and confining stress respectively.

4.3.3 Cyclic Loading Tests

Cyclic loading and unloading tests using the SUT machine were repeated three times for each of the variety and density. Six tests were carried out for each of the varieties and nine tests for each of the densities. A summary of the experimental design is shown in Table 1. All the tests were conducted at a moisture of content of $12 \pm$ 1.5% (w.b.)

Table 1: Summary of Cyclic Loading and Stress Relaxation Experiments

Variety	No of Replications	Density (kg/m^3)
V1	3	730
	3	800
V2	3	730
	3	800
V3	3	730
	3	800

Three loading and unloading cycles were conducted for each sample. Samples were loaded at a constant strain rate of 1.3 mm/min to a total strain of below 20% and then unloaded to zero. Load deformation data was manually recorded at intervals of 98.1 N (10 kgf). After the third and final test, the maize was carefully removed from the testing cell and discarded.

4.4 Determination of Elastoplastic Constitutive Parameters

The following dimensionless parameters defined under Lade's (1977) model were determined for the three varieties at the initial bulk density of 800 kg/m^3,

(1) Elastic parameters: Elastic modulus number, K, elastic modulus exponent, n, Poisson's ratio, ν

(2) Plastic Collapse Parameters: Plastic collapse modulus, C, plastic collapse exponent, P

(3) Plastic Expansive Parameters: Yield constant, η_1, yield exponent, m, first potential constant, R, second potential constant, S, potential exponent, t, work-hardening (first intermediate variable) constant, α, work-hardening (second intermediate variable) constant, β, peak work-hardening constant, θ, peak work-hardening exponent, ℓ

*4.4.1 **Elastic Parameters***

Volumetric Strain Increment

The volumetric strain increment ($\delta\varepsilon_p$) is defined as (Wood, 1990)

$$\delta\varepsilon_p = \frac{-\delta v}{v} \quad (4.4)$$

where:

v is the specific volume of the granular matter and the negative sign is required because, by convention compressive strains (and stresses) are taken as positive.

This relationship can be re-written in terms of void ratio (e) or porosity (n) as;

$$\delta\varepsilon_p = \frac{-\delta e}{1+e} = \frac{-\delta n}{1-n} \qquad (4.5)$$

The elastic strain increment is calculated using the generalized three-dimensional Hooke's Law (Timoshenko and Goodier, 1970):

$$d\{\varepsilon^e\} = [E]^{-1} d\{\sigma\} \qquad (4.6)$$

Where:

$d\{\varepsilon^e\}$ is the elastic Strain Increment

$d\{\sigma\}$ is the stress Increment

$d\{E\}$ is the elastic moduli tensor defined by the elastic constitutive matrix of Eqn (3.1)

Unloading and reloading moduli

The unloading and reloading elastic moduli, E_{ur}, were determined from hydrostatic loading experiments as described by Chi and Kushwaha (1990). Poisson's ratio was determined by Eqn (4.7a).

$$\nu = \frac{3B_{ur} - E_{ur}}{6B_{ur}} \qquad (4.7a)$$

Where:

B_{ur} is the unloading and reloading bulk modulus.

The elastic loading and unloading modulus E_{ur} is given as:

$$E_{ur} = K.P_a.(\sigma_3 / P_a)^n \qquad (4.7b)$$

From Fig. 2, E_{ur} is determined from the curve of deviatoric stress versus axial strain. Further, by plotting the same curve for deviatoric stress against volumetric strain, B_{ur} the bulk unloading and reloading modulus is obtained (Chi and Kushwaha, 1990). The mean poisson's ratio (ν), for each of the three samples at 12 $\pm$ 1.5% moisture content were determined in this manner.

The relationship between confining stress and elastic modulus has been given in Eqn (4.7b). Taking the atmospheric pressure as 98 kPa, the parameters in this equation were determined from experiments by graphical plots of $\mathrm{Log}(E_{ur}/P_a)$ versus $\mathrm{Log}(\sigma_3/P_a)$.

4.4.2 Plastic collapse parameters

The generalized Hooke's law is described in equations (3.2) and (4.6)

For a situation of collapse yielding, the condition;

$$f_C = K_C \qquad (4.9)$$

must apply.

Under the conditions of Eqn 4.17, for plastic collapse, plotting $\mathrm{Log}(W_c/P_a)$ versus $Log(f_c/P_a^2)$ gives the collapse modulus- C as its intercept and the collapse exponent- P as the slope.

4.4.3 Plastic expansive parameters

Yield parameters- the yield constant (η) has been used to define material failure (Zhang *et al.*, 1986). This constant is determined by splitting the plastic expansive equation $f_p = (I_1^3/I_3 - 27)(I_1/P_a)^m$ subject to the condition ($f_p = \eta_1$ at failure);

$$(I_1^3/I_3 - 27) = (P_a/I_1)^m.\eta_1 \qquad (4.10)$$

A graphical plot of $\mathrm{Log}(I_1^3/I_3)$ versus $\mathrm{Log}(P_a/I_1)$, gives the intercept and slope as η_1 and m, respectively.

4.4.4 Potential Parameters

The potential constants R, S and t are defined as $\eta_2 = S \cdot f_p + R \cdot \left(\frac{\sigma_3}{P_a}\right)^{1/2+t}$. To determine the potential parameters R, S and t, equation (4.11) (Chi and Kushwaha, 1990) was used;

$$\eta_2 = S \cdot f_p + Y \qquad (4.11)$$

and

$$Y = R\left(\frac{\sigma_3}{P_a}\right)^{1/2+t} \qquad (4.12)$$

where:

η_2 was determined from experimental data using Eqn (4.13);

$$\eta_2 = [3(1+v_p)I_1^2 - 27\sigma_3(\sigma_1 + v_p\sigma_3]/[\frac{P_a^m}{I_1}\{\sigma_3(\sigma_1 + v_p\sigma_3) - (m(1+v_p)I_1^2/(f_p(P_a/I_1)^m + 27)] \qquad (4.13)$$

The ratio, v_p, was defined as;

$$v_p = \frac{-d\varepsilon_p^3}{d\varepsilon_p^1}, \qquad (4.14)$$

which is the ratio of plastic expansive lateral strain to plastic longitudinal strain. This ratio has also been defined by the dilatancy angle ϕ, where,

$$\tan\phi = \frac{d\varepsilon_p^\tau}{d\varepsilon_p^\sigma} \qquad (4.15)$$

in the τ,(shear stress)-σ (axial stress) plane (Wood,1990)

By plotting η_2 against f_p, the potential constants, Y (the intercept) and S (the slope) were obtained. Similarly, for various values of σ_3, (varying values for Y), a plot of Y against $(\sigma_3/P_a)^{1/2}$, the slope R and the intercept t were obtained.

4.4.5 Work Hardening Parameters

The work hardening parameters were obtained as below.

The intercept and slope of $\text{Log}\frac{W_{ppeak}}{P_a}$ versus $\text{Log}\frac{\sigma_3}{P_a}$ curve gave the work hardening constant θ and exponent ℓ respectively. Similarly, the intercept and the slope of q versus (σ_3/P_a) curve (where q is defined by as $q = \alpha + \beta \cdot \frac{\sigma_3}{P_a}$) were the work-hardening constants α and β, respectively.

For different values of confining stresses, W_{ppeak} and q were determined. It was noted that for expansive yield condition, the following criterion must hold (Gumbe and Maina, 1990);

$$f_p = K_p, \qquad (4.16)$$

The plastic expansive loading function is equivalent to the plastic expansive work hardening function; both are dimensionless parameters implying that;

$$f_p = (I_1^3/I_3 - 27)(I_1/P_a)^m = K_P = a \cdot e^{-W_P}(W_P/P_a)^{1/q} \qquad (4.17)$$

where:

$$a = \eta_1 \left(\frac{e \cdot P_a}{W_{ppeak}} \right)^{1/q} \quad (4.18)$$

First, f_p was plotted against (W_p / P_a) from where the values of W_{ppeak} were read at $f_p = \eta_1$ Secondly, from the graph of $\mathrm{Log}(W_{ppeak} / P_a)$ versus $\mathrm{Log}(\sigma_3 / P_a)$, the intercept and slope gave ℓ and θ respectively. By substituting these values for the yield function, equation (4.19), was obtained.

$$q = \frac{\log(\frac{W_{ppeak}}{W_p}) - (\frac{1 - W_p}{W_{ppeak}}) \cdot \log(e)}{\log \frac{\eta_1}{f_p}} \quad (4.19)$$

By choosing $f_p = f_p,60 = 0.6 * \eta_1$ (Lade, 1977; Gumbe and Maina, 1990) from the f_p versus (W_p / P_a) curve, the values of q were calculated as;

$$q = \frac{\log(\frac{W_{ppeak}}{W_p,60}) - (\frac{1 - W_p,60}{W_{ppeak}}) \cdot \log(e)}{\log \frac{\eta_1}{f_p,60}} \quad (4.20)$$

a graphical plot of q versus (σ_3 / P_a), gave the intercept α and slope β.

4.5 Model Verification and Validation

Verification is the process by which, the internal logic of a given model is determined, while validation is the process of establishing the adequacy of a given model and involves tests to determine whether the given model is adequate or not i.e. whether the model is in agreement with the system or not (Agullo, 2003). In validating the above models for maize *en masse*, it was observed that the stress-strain characteristics of granular materials *en masse* are of practical importance to the point of material failure, or for strains of 20% and below. The models therefore had to make adequate predictions within this range. The applied models in the study were derived from the basic constitutive material behaviour which helped define the allowable parameter ranges. By varying the various components of the models, it was possible to observe the accuracy and stability of the models as they applied to maize *en masse*.

4.6 Statistical tests

Statistical tests were conducted as suggested by Li *et al.* (1990a) to compare the predicted and the observed behaviour of bulk maize. Among the statistical parameters that were determined were the coefficient of determination (R^2) and the t-test.

5.0 RESULTS AND DISCUSSIONS

The following section gives the parameters obtained from the various tests which were conducted at a moisture content of 12 $\pm$ 1.5% wet basis and 65% to 75% relative humidity. Poisson's ratio are presented in Table 3 for the three maize varieties.

Table 3: Poisson's ratio for the three maize varieties

Variety	***Poisson's Ratio***
V1	0.299
V2	0.263
V3	0.339

5.1 Triaxial compression test

The graphical representations of the triaxial test results obtained the different densities and under a confining stress of 100 kPa for the three varieties are given in Figures 5(a)-(c).

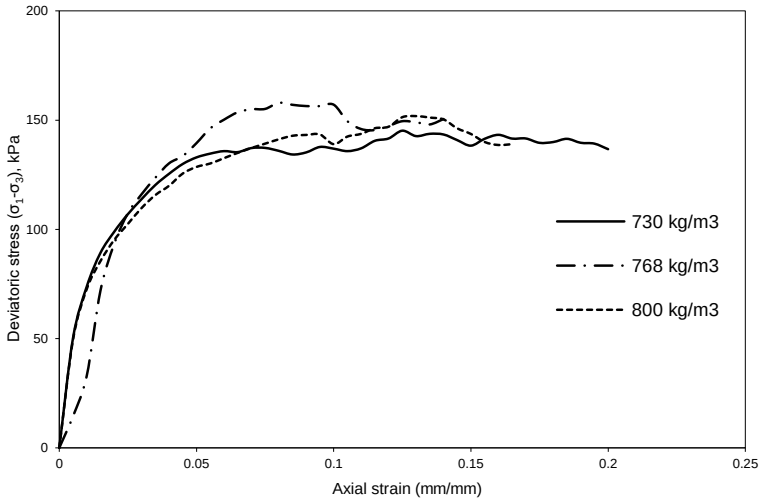

Fig 5a: Deviatoric stress-strain relations for VI sample under confining stress of 100 kPa at IBD of 730kg/m^3, 768 kg/m^3 and 800 kg/m^3

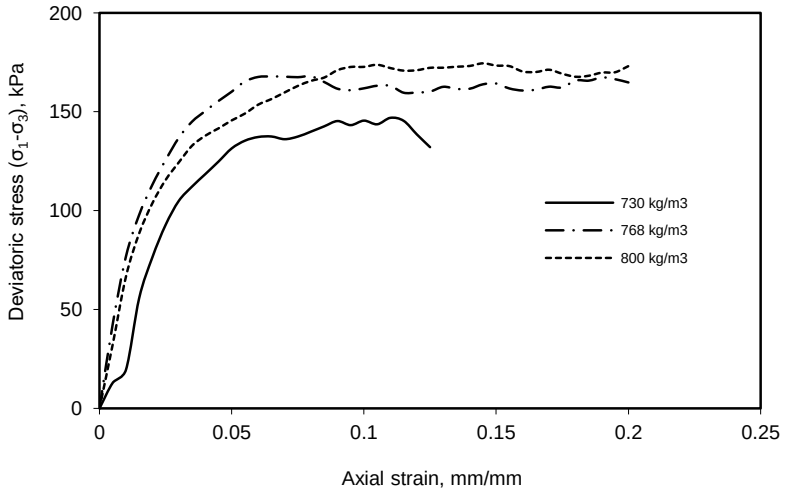

Fig 5b: Devatroric stress-strain relations for V2 sample under confining stress of 10kPa at IBD of 730kg/m^3, 768 kg/m^3 and 800 kg/m^3

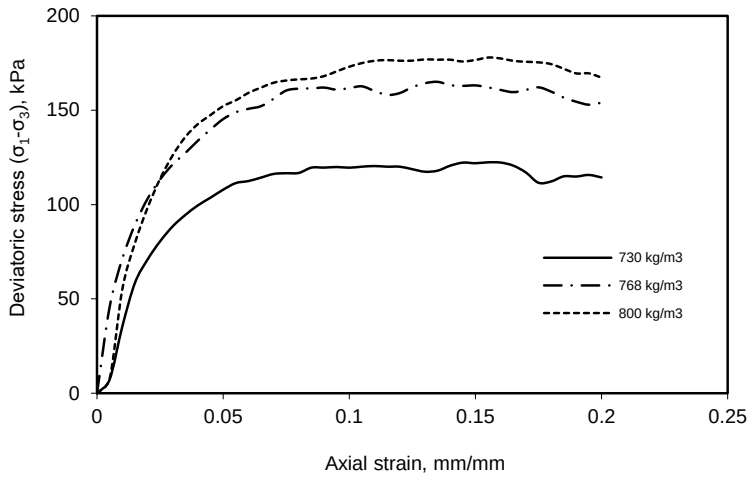

Fig 5c: Deviatroric stress-strain relations for V3 sample under confining stress of 10kPa at IBD of 730kg/m^3, 768 kg/m^3 and 800 kg/m^3

Figures 5a-c display the behaviour of typical stress-strain curves of most engineering materials. The stress-strain behaviour somewhat obeys Hooke's law up to a certain point (below 5% strain) before plastic behaviour sets in. The material then begins to exhibit both elastic and plastic behaviour for the greater part of the test until it finally collapses. Each of the figures can therefore be effectively divided into three portions namely elastic region, elastic-plastic region and the plastic collapse region. These regions however, have no distinct boundaries. Figures 5a-c also show a some dependence of stress-strain behaviour of shelled cohesionless bulk maize on the initial bulk density (IBD). At a higher IBD, there was a much steadier rise of stress with strain which resulted in higher collapse point (5c). However, it is important to note that this dependence appeared to be more visible only at strains greater than 10% as the curves seem to move together at the early stages of strain. To further examine this behaviour, two points were chosen on each of the stress-strain curves to assess whether there was any significant variation in the means of stress levels at the points. The points chosen were at 10% strain and 20% strain (or at collapse, whichever occurred first). The outcome is shown in Table 2

Table 2: Summary of stress at 10% strain and 20% strain (or at failure) for the three varieties.

Variety	**IBD (kg/m^3)**	**10% Strain**			**20%Strain (or at collapse)**		
		confining stress (kPa)			**confining stress (kPa)**		
		100	**200**	**300**	**100**	**200**	**300**
V1	**730**	137	261	406	143	292	388
	768	157	258	406	158	285	422
	800	139	253	399	152	266	399
V2	**730**	146	264	405	147	277	417
	768	162	314	415	167	313	417

	800	173	293	405	174	308	437
V3	**730**	120	346	441	122	368	441
	768	162	283	424	165	294	460
	800	173	302	407	177	310	456

The ANOVA results also showed a strong indication that confining stress highly influenced the stress-strain behaviour both at strains of 10% and at 20%. However, the influence of grain IBD on these characteristics is not as pronounced, being insignificant at the 5% level. This is in agreement with the observations of *Figs 5a-c*.

It is possible to visually verify the significance of these findings by considering the stress-strain behaviour displayed in *Figs 5a-5c* for different confining stresses

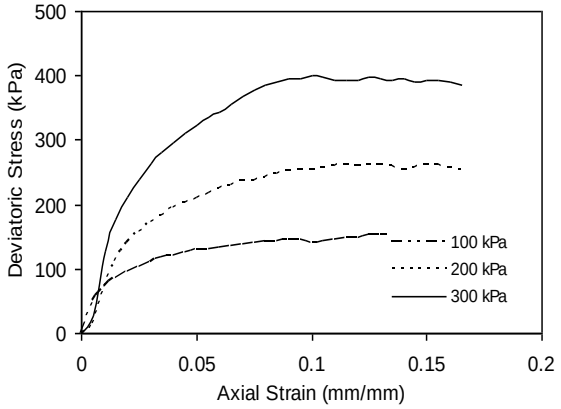

Fig. 6a: Deviatoric stress vs axial strain for VI at IBD of 800 kg/m3; confining stress of 100kPa, 200 kPa and 300 kPa

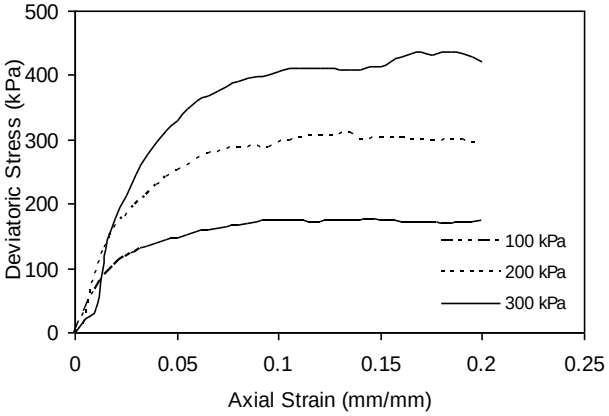

Fig. 6b: Deviatoric stress vs axial strain for V2 at IBD of 800 kg/m3; confining stress of 100kPa , 200 kPa and 300 kPa

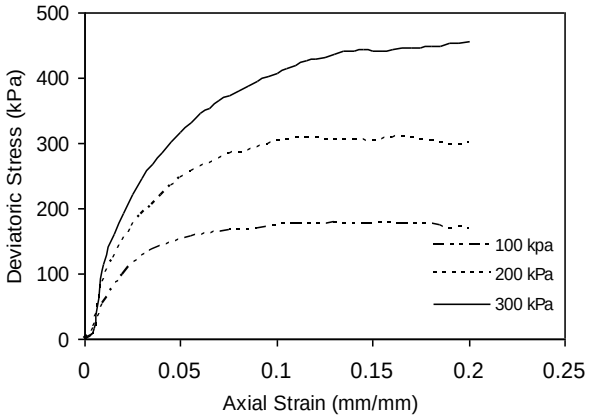

Fig. 6c: Deviatoric stress vs axial strain for V3 at IBD of 800 kg/m3; confining stress of 100kPa 200 kPa and 300 kPa

5.2 Cyclic Loading Tests

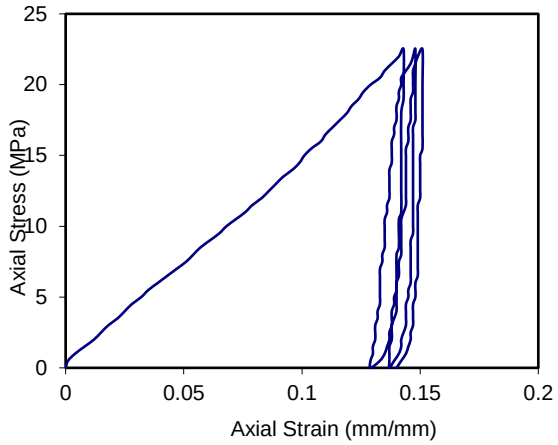

Figure 7a: Cyclic loading-unloading test for variety V1 at IBD of 800 kg/m^3

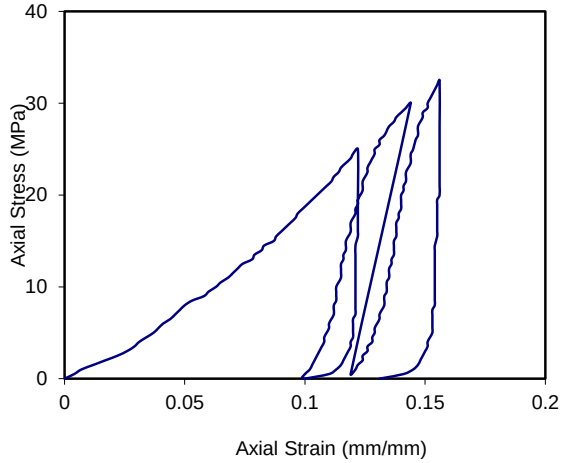

Fig. 7b: Cyclic loading-unloading test for variety V2 at IBD of 800 kg/m^3

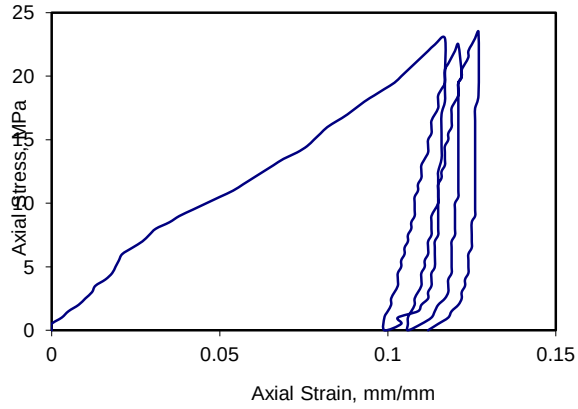

Figure 7c: Cyclic loading-unloading test for variety V3 at IBD of 800 kg/m^3

Figures 7a-7c show cyclic loading and unloading curves obtained from the cyclic loading and unloading experiments of the SUT machine for V1 V2 and V3 at IBD of 800 kg/m^3. The figures show that about 10% of the initial strain was not recovered in unloading for all the three varieties. Elasticity theories would have expected the stress to follow the same path in unloading as in loading. However, from *Figs 7a-7c*, it is evident that the bigger part of the initial strain is permanent. The cyclic loading section also produced curves that were almost parallel to each other (of slope E_{ur}) as was expected of other engineering materials on cyclic loading/unloading. These findings are consistent with those of Li *et al.* (1990) for granular agricultural materials. The resulting prestrain and the occurrence of hysteresis loops on *Figs 7a-7c* on cyclic loading/unloading are also characteristic of annealed engineering materials under similar loading conditions as reported by Chakrabarty (1987).

5.3 Elastoplastic Parameters

Summary of Lade's parameters for maize en masse

Figures 8a- g show how the various parameters of Lade's elastoplastic model were obtained graphically.

Figs 8a-g: Lade's elastoplastic parameters

Elastic parameters

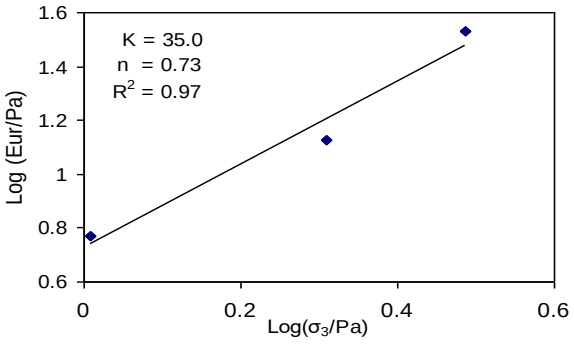

Fig. 8a: Elastic modulus number K and exponent n for V1

Plastic collapse parameters

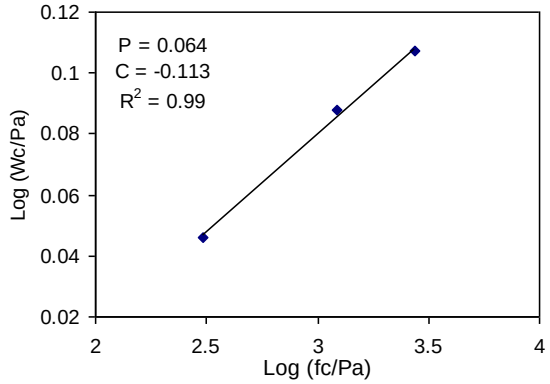

Fig. 8b: Plastic collapse parameters C and P for V1

Plastic expansive parameters

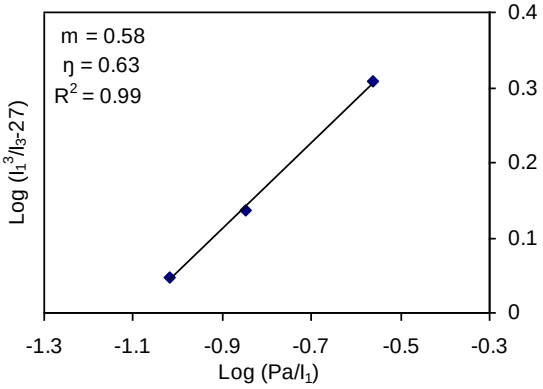

Fig. 8c: Plastic expansive yield constant, η_1, and exponent, m, for V1

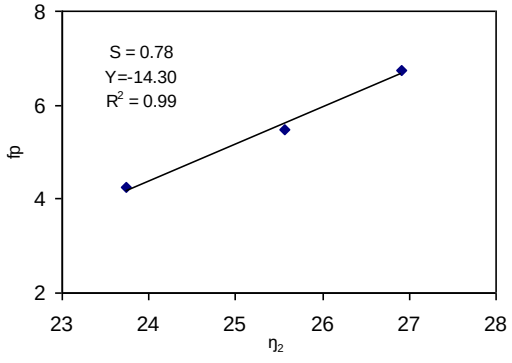

Fig. 8d: Potential constants Y and S for V1 (100kPa)

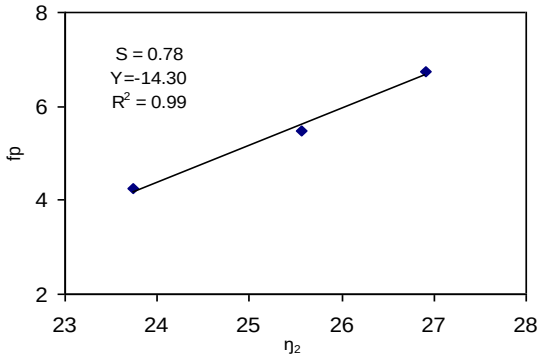

Fig. 8e: Potential constants Y and S for V1 (100kPa)

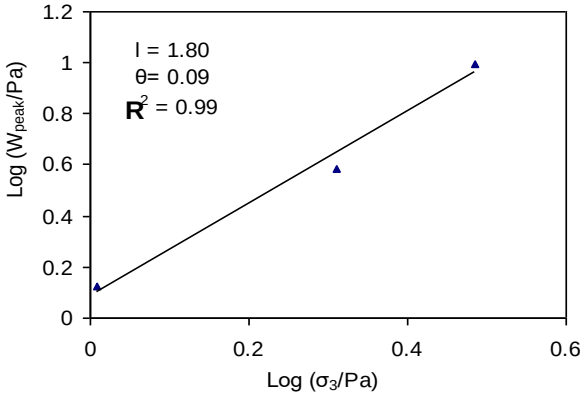

Fig. 8f: Work hardening constant, θ and exponent ℓ , for V1

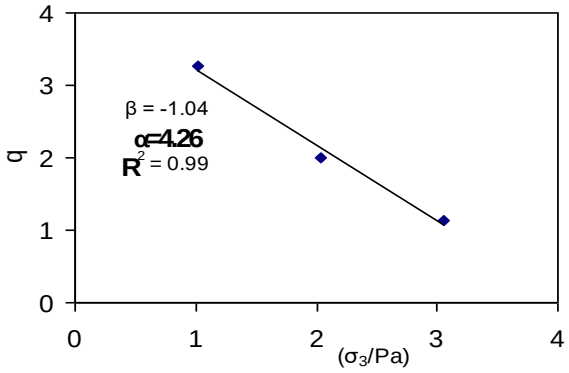

Fig. 8g: Work hardening constants, α and β , for V1

Table 4 shows a summary of the values of Lade's parameters obtained for shelled maize *en masse* and the values obtained for wheat by Li *et al.* (1989).With these parameters, it was possible to

completely define the elastoplastic model given by Eqn (3.2).

Table 4: Lade's Elastoplastic Parameters

	PARAMETER	SYMBOL	VALUE			
			V1	V2	V3	Li *et al*, (1989) (wheat)
ELASTIC	Modulus number	K	35.0	45.9	29.3	308
	Modulus Exponent	n	0.73	0.84	0.93	0.78
	Poisson's ratio	ν	0.30	0.26	0.34	0.26
PLASTIC COLLAPSE	Modulus	C	-0.113	-0.142	-0.122	0.004
	Exponent	P	0.064	0.081	0.061	0.739
PLASTIC EXPANSIVE	Yield constant	η_1	0.63	0.97	1.01	9.53
	Yield exponent	M	0.578	0.819	0.846	0.064
	Potential constant	R	-1.21	-1.73	-1.53	-0.04
	Potential constant	S (mean)	0.51	0.30	0.68	0.33
	Potential constant	t	0.50	1.17	0.86	0.45
	Work-hardening constant	α	4.261	6.297	6.107	3.66
	Work-hardening constant	β	-1.044	-1.602	-0.692	-0.18
	Work-hardening constant	θ	0.09	0.17	0.30	0.11
	Work-hardening exponent	ℓ	1.80	2.27	2.60	1.28

The R^2 value for all the parameters obtained was observed to be mostly within the 90% range and as such showed good fit of the parameters. As reported by Li *et al.* (1989) the elastic modulus number K seem to have been strongly dependent on the axial strain rate (ASR), where high rates of strain resulted in low K values. This is observable in much lower K values obtained for the maize varieties than those for the wheat as the strain rate used was slightly above that applied by Li and others. However, differences in material physical properties may also have contributed to similar deviations.

The elastic modulus exponent for the three maize varieties provided a maximum deviation of only about 19% form that of wheat, a finding which confirms the dependence of this factor on the initial bulk density and not the strain rate as reported by Zhang *et al.* (1989a). The magnitude of the plastic collapse modulus parameter obtained implied higher void ratio for maize therefore larger volume changes in compressive loading as compared to wheat en masse. This is consistent with the physical expectations and also confirms the findings of Zhang *et al.* (1989a).

The nine plastic expansive parameters, in physical terms, measured the response of the bulk maize to the deviatoric component of stress. This effect may be observable in hardening of the material, influencing the direction of plastic expansive strain or direction of failure of the material. The relatively higher values obtained for the plastic expansive parameters and, especially the work hardening parameters, are therefore expected to significantly influence the failure stress-strain characteristic of shelled maize *en masse* especially as regards energy storage within the material. These parameters, except for the work hardening constant α, are not affected by moisture content of the agricultural material (Zhang *et al.*, 1989a). The significance of these findings become more evident in the sections that follow.

5.4 Application of parameters to Lade's model

For strains beyond 0.1 mm/mm, the comparison between the results of Lade's model and the actual behaviour of bulk maize showed a consistent trend. This trend is indicated in Figure 9a–c taken from the three varieties at the initial bulk density of 800 kg/m^3 and a confining stress of 100 kPa.

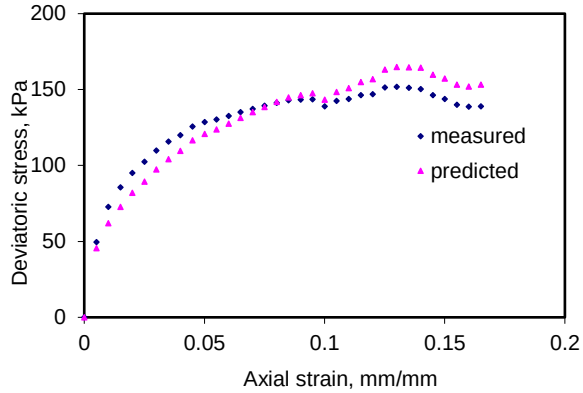

Fig. 9a: Relationship between measured stress-strain response and calculated response under Lade's model for variety V1

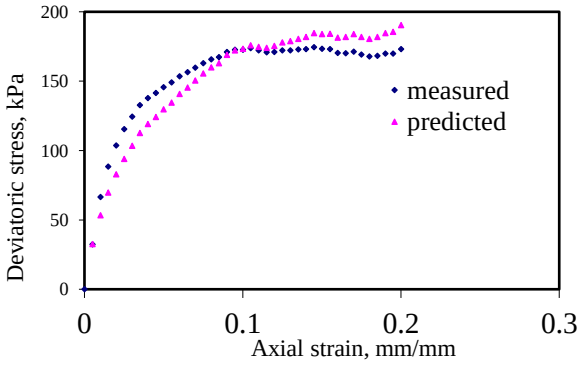

Fig. 9b: Relationship between measured stress-strain response and calculated response under Lade's model for variety V2

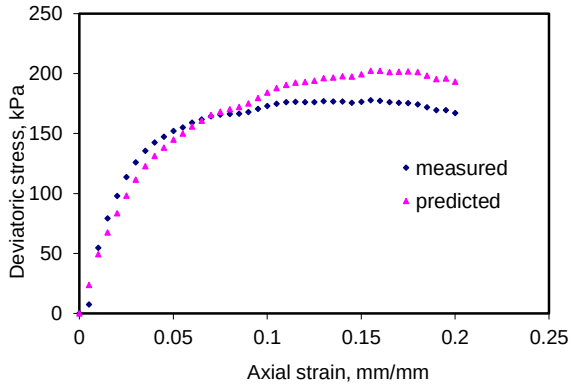

Fig. 9c: Relationship between measured stress-strain response and calculated response under Lade's model for variety V3

Figures 9a–9c indicate a consistent rise of values predicted by Lade's model above those experimentally determined at strains beyond 0.1 mm/mm. This could be the link between Mohr-Coulomb failure criterion for cohesionless granular maize and Lade's elastoplastic model for the same material. The difference in cohesiveness of soils as compared to bulk maize ($c \approx 0$, equation (3.3)) makes the response of the measured values reduce in magnitude at high strains, a factor that does not seem to have been taken care of in Lade's model. Similar trend was clearly observed in curves obtained by Zhang *et al*, (1989b) for wheat *en masse*.

Figures 10a-10c show the coefficient of determination values of deviatoric stress for the three maize varieties under a confining stress of 100 kPa and initial bulk density (IBD) of 800 kg/m^3.

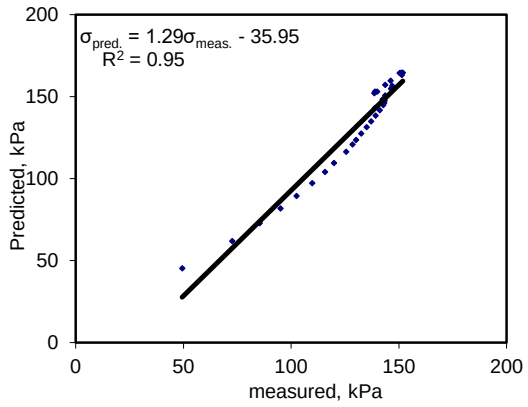

Fig. 10a: Coefficient of determination for variety V1 under 100 kPa confining stress

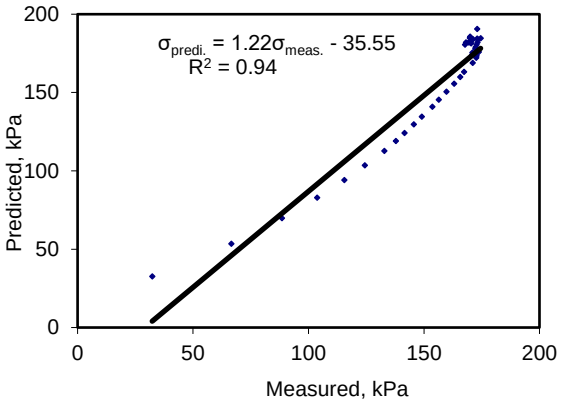

Fig. 10b: Coefficient of determination for variety V2 under 100 kPa confining stress

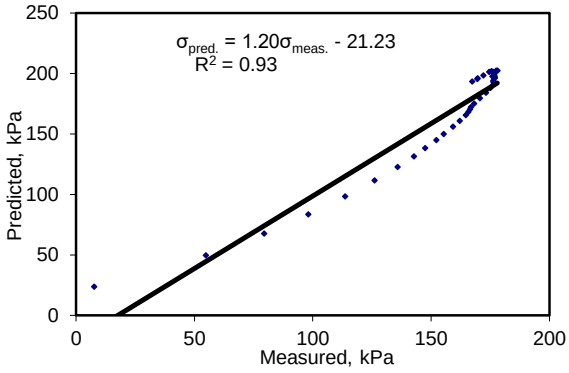

Fig. 10c: Coefficient of determination for variety V3 under 100 kPa confining stress

The behaviour of curves presented in *Figs 10a-10c* closely resemble those obtained by Zhang *et al.* (1989b) for bulk cohesionless wheat which indicated a linear correlation between the predicted values and the measured values. A two sample paired t-test gave p-values of 0.456, 0.624 and 0.0001 for V1, V2 and V3 respectively.

Figures 9a–c indicate three different distinct sections on the plots; the lower elastic section, the central elastic-plastic section and the collapse section. These sections correspond to the definition of elastoplastic constitutive models given by Eqn (3.1). It is therefore evident from these findings that Lade's model accurately describes the transition section between the elastic region and the collapse region of granular shelled maize *en masse* much more accurately than it does the elastic or the collapse sections.

6.0 CONCLUSIONS

Shelled maize *en masse* exhibits stress-strain behaviour that is consistent with other engineering materials. The fourteen elastoplastic parameters under Lade's elastoplastic model for cohesionless sand were determined for three local maize varieties. The values were then used to predict the behaviour of bulk maize under isotropic and triaxial loading conditions. The results showed that Lade's model can be used adequately to predict bulk maize behaviour especially at strains below 15%. The findings of this research have shown that shelled maize *en masse* may be considered as being elastoplastic based on Lade's model.

7.0 REFERENCES

Agullo J O (2003). Environmental simulation of a greenhouse system in Kenya. M. Sc. Thesis, University of Nairobi

Aklonis J J; MacKnight W J (1983). Introduction to Polymer Viscoelasticity. 2nd Ed. John Wiley and Sons, New York

Alonso-Marroquin F; Herrmann H J (2002). Ratcheting of granular materials ICA1, University of Stuttgart, Pfaffenwaldring 27, 70569 Stuttgart, germany, http:/arxiv.org/pdf/cond-mat/0305043

Bishop A W; Henkel D J (1957). The Measurement of Soil Properties in Triaxial Test. London, William Arnold

Boumans G (1983). Grain Handling and Storage. Elsevier Science Publishers. Amsterdam

Cates M E; Wittmer J P; Bouchaud J P; Claudin P (1999). Jamming and static stress in granular materials. *CHAOS*, Vol.9, No.3, pp.511-522 (1999); cond-mat/9901009

Chakrabarty J (1987). Theory of Plasticity.McGraw-Hill Inc. pp. 3-6.

Chi L; Kushwaha R L (1990). Lade's elastoplastic model for granular soils. American Society of Agricultural Engineers. Paper No. 90-1084.

Chi L; Tessier S; McKyes E; Laque C (1993). Modelling mechanical behaviour of agricultural soils. Trans. of ASAE 36(6); 1563-1570

Chung T J; (1988). Continuum Mechanics. Prentice-Hall International, Inc.

Cooper A R; Eaton L E (1962). Compaction behaviour of several ceramic powders. Journal of the American Ceramic Society 45(3): 97-101

Dartevelle S; (2003). Numerical and granulometric approaches to geophysical granular flows**,** Ph.D. thesis, Michigan Technological University, Department of Geological and Mining Engineering, Houghton, Michigan

FAO (2022). FAOSTAT 2022. http://faostat.fao.org/site

Foutz T L; Thompson S A; Evans M D (1993). Comparison of loading response of packed grain and individual kernels. ASAE Paper No. 92-4014

Fournier Z; Geromicholas D; Herminghaus S; Kohonen M M; Mugele F; Scheel M; Schulz M; Schulz B; Schier C; Seemann R; Skudlny A (2005). Mechanical properties of wet granular materials. J. Phys.: cond. Matter 17 S477

Goldhirsch I; Goldenberg C (2004). Stress in dense granular materials. In: The Physics of Granular media. Hinrichsen, H. and Dietrich E. W. (Eds). Wiley-VCH Vedag GmbH & Co. KGaA, Weinheim

Gremaud P A; Mathews J V (2000). Simulation of gravity flow of granular materials in silos. Department of Mathematics and Centre for Research in Scientific Computation. North Carolina State University, Raleigh, NC27695-8205, USA

Government of Kenya (2010). Agricultural Sector Development Strategy, 2010-2020. Government printers, Nairobi.

Gumbe L O (1995). Load deformation behaviour of soils and en-masse grains. Paper Presented at the Symposium on Unsaturated Soil Behaviour and Applications. Nairobi, Kenya

Gumbe L O (1993). Introduction to mechanical properties of engineering materials. Lecture Notes, Department of Agricultural Engineering. University of Nairobi. Unpublished

Gumbe L O; Maina B M (1990). Elastoplastic constitutive parameters for rice e*n-masse*. African Journal of Science and Tech. 2: 15-26

Harri D (2009). An elastoplastic model for deformation and flow of granular materials and its connection with micro mechanical quantities. In: Powders and Grains 2002: Proceedings of the 6th international conference on micromechanics of granular media. Vo. 1145 pp 1085-1088. doi: 10.1063/1.3179833

Heidarbeigi K; Ahmadi H; Kheiralipour K; Tabatabaeefar A (2009). Some physical and mechanical properties of Khinjuk. Pakistan Journal of Nutrition 8 (1): 74-77

Heinrich M J; Sidney R N; Robert P B (1996). The Physics of Granular Materials. In: Physics Today, pp 32

Horabik, J., and M. Molenda (2016) : Parameters and contact models for DEM simulations of agricultural granular materials: A review. Biosystems Engineering. Institute of Agrophysics Polish Academy of Science, Doswiadczalna 4, 20-290, Lublin, Poland. In ScienceDirect

Horabik, J., and M. Molenda (2014) : Mechanical properties of granular materials and their impact on load distribution in silo: A review. Scientia Agriculturae Bohemica. 45, 2014(4): 203-211

Knappman K (1999). Granular materials: liquid-like properties of sand. Physics NSF REU 1999 Program. The Ohio State University

KALRO (2022): Maize. https://www.kalro.org/maize/

Lade P V (1977). Elasto-plastic stress- strain theory for cohesionless soil with curved yield surface. International Journal of Solids and Structure; 13: 1019-1035

Latzel M; Luding S; Herrmann H J (2000a). From discontinuous models towards a continuum description. In P. A. Vermeer et al. (Eds), Continuous and Discontinuous Modeling of Cohesive Frictional Materials, Springer, Berlin: 215-230

Latzel M; Luding S; Herrmann H J (2000b). Macroscopic material properties from quasi-state, microscopic simulations of a two-dimensional shear-cell. Granular Matter 2(3): 123-135. cond-mat/0003180

Li Y; Puri V M; Manbeck H B (1990). Elasto-viscoplastic cyclic constitutive model parameter determination and evaluation for wheat en-masse. Trans. of ASAE 33(6): 1984-1995

Li Y; Zhang Q; Puri V M; Manbeck H B (1989). Elasto-plastic constitutive equation parameters and load response of wheat en-masse-part-I, initial density, moisture content and strain rate effects. Trans. of ASAE 32(1): 194-202

Mani S; Tabil L G; Sokhansanj S (2002). Compaction behaviour of some biomas grinds. Paper written for presentation at the AIC 2002 meeting, Saskatoon, Saskatchewan, Canada

McLaughlin N B; Pitt R E (1984). Failure characteristics of apple tissue under cyclic loading. Trans. of ASAE 27: SE 1984: 311-320

Mohsenin N N (1980). Thermal Properties of Foods and Agricultural Materials. Gordon and Breach, New York

Moukarzel F C (1998). Granular matter instability; a structural rigidity point of view. Proc. of Rigidity Theory and Applications. Traverse City, MI

Moya M; P. J. Aguado and F. Ayuga (2013). Mechanical properties of some granular agricultural materials used in silo design. Int. Agrophys., 2013, 27, 181-193: doi: 10:2478/v10247-012-0084-9

Moya M; Ayuga F; Guaita M; Aguado P J (2002). Mechanical properties of granular agricultural materials considered in silos design. ASCE Engineering Mechanics Conference; Colombia University, New York

Moya M; Guita M; Aguado P; Ayuga F (2006). Mechanical properties of granular agricultural materials. Transactions of the ASAE. Vol. 49 No. 2 pp 479-489

Novoa-Martinez B (2003). Strength properties of granular materials. M.Sc. Thesis. Department of Civil and Environmental Engineering, Louisiana State University and Agricultural and Mechanical College

Ozturk T; Esen B (2008). Physical and mechanical properties of barley. Agricultura Tropica et Subtropica. Vol. 41 (3)

Sinha R N (1973). Interrelations of physical, chemical and biological variables in determination of stored grains. Grain storage; part of a system: An AVI Publication, Westport, Connecticut: 15-47

Snedecor G W; Cochran W G (1980). Statistical Methods. The Iowa State University Press. Ames Iowa, U.S.A: pp 83-106

Stafford J V; Audsley E; Sharp J R (1986). The determination of best fit linear failure envelopes to Mohr Circles. J. Agric Eng. Res. (1986)33, 33-38

Steel R G; Torrie J H (1980). Principles and Procedures of Statistics, 2nd Ed., A Biometrics Approach. McGraw-Hill Inc

Stefan L (2001). From DEM simulations towards a continuum theory of granular matter. In: Powders and

Grains 2001, Y. Kishino (Ed.), Balkema, Netherlands 2001: 141-148

Stinchcomb W W (1989). Damage and fracture of composite materials under cyclic loads. Advances in fracture research. Salama, Ravi-Chandar, Taplin and Rama (eds); 4: 2939-2955

Svedsen B K; Hutter K; Laloui L (1999). Constitutive models for granular materials including quasi-static frictional behaviour: Toward a thermodynamic theory of plasticity. Continuum Mech. Thermodyn. 4: 263-275

Ti K S (2009). A review of basic soil constitutive models for geotechnical application. EJGE Vol. 14, Bund. J

Timoshenko S P; Goodier J N (1970). Theory of Elasticity. 3rd ed. McGraw-Hill Book Company

Tordesillas A (2004). The jekyl and hyde of granular materials uncovered. www.unimelb.edu.au/

Vanel L; Claudin P; Bouchaud P J; Cates M E; Clement E; Witterner J P (2000). Comparison between theoretical models and new experiments. Physical Review Letters; 84(7): 1439-1442

Wang Q; Pufahl D E; Fredlund D G (2002). A study of critical state on an unsaturated silty soil. Can. Geotech. J. 39: 213-218

Wood M W (1990). Soil Behaviour and Critical State Soil Mechanics. Cambridge University Press. Cambridge

Wulfsohn D; Adams A B; Fredlund D G (1996). Triaxial testing of unsaturated agricultural soils. J. Agric. Eng. Res. (1998) Vol.69, pp317-330

Yamada K (1999). Computation for rheological phenomena of elastic viscoplastic body. Journal of Engineering Mechanics; 125 (1): 11-18

Youngs R R (1982). A three dimensional effective stress model for cyclicly loaded granular soils. Ph. D. Dessertation. The University of California

Zhang Q; Puri V M; Manbeck H B (1994). Applicability of a two-parameter failure criterion to wheat *en masse*. Trans. of ASAE. 37(2): 571-575

Zhang Q; Puri V M; Manbeck H B (1986a). Determination of elasto plastic constitutive parameters for en-masse wheat. Trans. of ASAE 29(6): 1739-1746

Zhang Q; Puri V M; Manbeck H B (1986b). Finite element modelling of thermally induced pressures in grain bins filled with cohesionless granular materials. Trans. ASAE.29 (1): 248-256

Zhang Y H; Jofriet J C; Negi S C (1998). Stress-strain and volume strain-strain relationships for soybean. Canadian Agricultural Engineering. Vol.40, No 2; pp 105-111

Zhang Q; Li Y; Puri V M; Manbeck H B (1989a). Physical properties effect on stress-strain behaviour of wheat en-masse – Part I. Constitutive elastoplastic parameter dependence on initial bulk density and moisture content. Trans. of ASAE 32 SE 1989: 194-202

Zhang Q; Li Y; Puri V M; Manbeck H B (1989b). Elastoplastic constitutive equation parameter and load response of wheat en-masse- Part II, Constitutive equation parameter dependence on initial density and moisture content. Trans. of ASAE 32 SE 1989: 203-209

HIGH PERFORMANCE CONCRETE: An eco-friendly and sustainable construction material.

D.O. Koteng'[1*]

[1]Associate Professor and Director of the School of Civil and Resource Engineering, Technical University of Kenya, Nairobi, Kenya

Corresponding author*:

Publication Date: March 2023

ABSTRACT:

Environmental and sustainability concerns have been expressed in connection with the use of concrete as a construction material. These arise from high CO_2 emissions and energy demand associated with the production of cement, high consumption of natural raw materials in the production of cement and as aggregate for concrete, degradation of the landscape associated with the exploitation of raw materials, and in some cases low durability in harsh environments leading to high maintenance and replacement costs. The popularity of concrete as a construction material affects human life worldwide and heightens these concerns. On the other hand, concrete has demonstrated ability to absorb many post-consumer, industrial and agricultural wastes as cement replacement materials, and as alternative or partial replacement of conventional aggregates. By doing so, a large proportion of aforementioned negative effects are mitigated, and an avenue for the disposal of post-consumer, industrial and agricultural wastes is provided. Since concrete is a man-made product, it is argued that any problems that may be associated with concrete use lie with the concrete producer rather than the material itself. With good practices in concrete production and use, the material can sustain human construction needs as long as necessary while providing a clean environment.

Key words: *high performance, sustainable use of materials, reduced energy profile and CO_2 emissions, clean environment.*

1.0 INTRODUCTION

Concrete is a widely used construction material that has stood the test of time. Historical records show that as early as 7,000 BC, concrete was in use in the Middle East utilizing calcined limestone (CL) as a binder (Irish Concrete Society, 1973). On the other hand, the American Concrete Institute reports that a hydraulic binder consisting of lime mixed with a natural pozzolan (NP) was in use in the Persian Gulf as early as 5,000 BC (ACI Committee 232, 2000). Similarly, analysis of mortars from the Mediterranean basin have revealed that CL intermixed with crushed burnt bricks (CBB) or NP were used to produce mortar for masonry construction and plaster as far back as the Minoan civilization (3,300 – 1,100 BC) (Stefanidou, et al., 2013). On the other hand, the use of calcined gypsum as a binder n Egypt dating back to 3,000 BC has been reported (Li, 2011)

Early concrete consisted of mortar comprising fine aggregate and a binding paste, and was used for masonry construction and as plaster (Papayianni & Pachta, 2016). The incorporation of coarse aggregates to produce concrete as we know today is attributed to the Roman civilization (753 BC – 476 AD) (Jackson, et al., 2014), (Kramar, et al., 2011). It has been suggested that the Romans added animal fat, milk, and blood to improve the properties of concrete in the fresh and hardened state (Gromicko & Shepard, 1994) and also pioneered fibre

reinforcement of concrete by adding horse hair (Paul, 2016). These skills were carried to different parts of the Roman empire which encompassed a large part of Europe, Asia, and Northern Africa.

With the introduction of Portland cement (PC) in England in the !9th century, its largescale production made possible by the industrial revolution, and its worldwide distribution made possible by the British worldwide influence, PC became the primary binder for concrete throughout the 19th and a large part of the 20th century. Its ready acceptance was influenced by its higher rate of strength gain when compared with earlier binders. However, many environmental and durability shortcomings of PC concrete have brought into focus the need to blend PC with a variety of cement replacement materials (CRM) to influence the environmental, structural, cost, and sustainability properties of concrete.

According to the American Portland Cement Association, the current annual worldwide consumption of cement stands at about 4.3 billion tonnes (Portland Cement Association, 2015). With a global population of 8 billion (Giatec Scientific Inc., 2022), this translates to a per capita annual cement consumption of 538 kg. Since cement constitutes about 20% of concrete, the per capita concrete consumption stands at about 2,690 kg per annum. By comparison, the average per capita cement consumption in sub-Sahara Africa is estimated at 102 kg per annum (Harder, 2021), which translates to a per capita concrete consumption of 510 kg per annum. This low figure is due to high populations in sub-Sahara African countries accompanied by less intense construction compared to the more developed economies of America, Asia, and Europe. Nevertheless, these statistics attest to the potential influence concrete use can have on human life. Considering the large amounts of industrial, agricultural and post-consumer wastes that concrete can absorb as CRM or aggregate, concrete use can exert a big positive influence on the environment, economy, cost, and sustainability of the construction industry. This is the focus of this paper..

2.0 LITERATURE REVIEW

2.1 What is concrete?

The American Concrete Institute defines concrete as a “mixture of hydraulic cement, aggregates, and water, with or without admixtures, fibres, or other cementitious materials” (American Concrete Institute, 2013). It is essentially a 3-phase composite material consisting of aggregates of different sizes, a cementitious powder, and water, with or without admixtures and fibres. The water is necessary for the hydration of the cementitious powder, and the chemical composition of the powder determines the chemical activity that takes place in concrete leading to strength and durability. The aggregates are largely chemically inert and must have high crushing and abrasion resistance. A large proportion of aggregates consist of crushed stone, natural gravel, and sand or stone dust. Common CRMs are pozzolans such as fly ash (FA), silica fume (SF), volcanic ash (VA), and a variety of plant ashes. Ground granulated blast furnace slag (GGBFS) is also a common CRM. A super-plasticizing admixture is used to improve the rheology of the fresh concrete and to reduce the amount of water required to produce a workable concrete. Incorporation of fibres delays the propagation of microcracks in the mass of concrete and allows higher loads to be carried.

3.0 Physical and chemical activities in Portland cement concrete.

3.1. Chemical composition of Portland cement.

PC is produced by inter-grinding PC clinker with a small amount of gypsum, whose purpose is to control the rate of setting of the cement paste. The clinker is produced from oxides of calcium obtained from limestone or chalk, silicon obtained from clay or shale, aluminium from bauxite or shale, and iron from iron ore. The raw materials are mixed in predetermined quantities, crushed and ground in a ball mill, homogenized, pre-heated and led into a kiln where the powder known as raw meal is sintered at 1200-1400oC to form pellets known as clinker. The chemical composition of the clinker is dependent on the composition of the raw materials, the mixing ratios, and the burning temperature. Typical composition of European clinkers is given in Table 1 (Moir, 2003). The PC will have the chemical compounds in Table 1 together with about 5% gypsum (CaSO4.2H2O) and small quantities of CaO, Na2O, K2O, SO3 and MgO. The relative proportions of alite (C3S) and belite (C2S), and the

fineness of grinding determine the reactivity of the cement, while the amounts of aluminate (C3A) and C3S largely determine the amount of the heat of hydration of the cement.

Table 1. Typical composition of European clinkers.

Mineral name	**Chemical composition**	**Nomenclature**	**Typical range** (% by mass)	**Typical composition** (% by mass)
Alite	$3CaO{\cdot}SiO_2$	C_3S	45–65	57
Belite	$2CaO{\cdot}SiO_2$	C_2S	10–30	16
Aluminate	$3CaO{\cdot}Al_2O_3$	C_3A	5–12	9
Ferrite	$4CaO{\cdot}Al_2O_3{\cdot}Fe_2O_3$	C_4AF	6–12	10

3.2. The role of water.

Water hydrates the compounds in PC to produce new products as shown in equations 1-4. Equation 5 takes place only if there is excess aluminate.

$$2(3CaO{\cdot}SiO_2) + 6H_2O = 3CaO{\cdot}2SiO_2{\cdot}3H_2O + 3Ca(OH)_2 \quad (1)$$

$$2(2CaO.SiO_2) + 4H_2O = 3CaO{\cdot}2SiO_2{\cdot}3H_2O + Ca(OH)_2 \quad (2)$$

$$3CaO{\cdot}Al_2O_3 + 3(CaSO_4{\cdot}2H_2O) + 26H_2O = 3CaO{\cdot}Al_2O_3{\cdot}3CaSO_4{\cdot}32H_2O \quad (3)$$

$$4CaO{\cdot}Al_2O_3{\cdot}Fe_2O_3 + 3(CaSO_4{\cdot}2H_2O) + 26H_2O = 4CaO{\cdot}Al_2O_3{\cdot}Fe_2O_3{\cdot}3CaSO_4{\cdot}32H_2O \quad (4)$$

$$3CaO{\cdot}Al_2O_3 + 6H_2O = 3CaO{\cdot}Al_2O_3{\cdot}6H_2O \quad (5)$$

In traditional concrete, water beyond that required to hydrate the cement is used in order to provide a workable concrete. However, when the excess water evaporates, the concrete shrinks in proportion to the free water lost from the pores of the concrete. Shrinkage leads to cracks, loss of prestress in prestressed concrete, and enhanced creep in structural members subjected to sustained compression. Moreover, the loss of water from the pores of concrete leaves empty spaces that make the concrete porous and of low durability. In a fire situation, free water in concrete exerts steam pressure leading to spalling and early deterioration of concrete. Free water in the pores of concrete also supports chemical activity in hardened concrete which can lead to low durability. In steel reinforced concrete, water ionises in the presence of oxygen and acts as an electrolyte facilitating the movement of ions from one pole to the next, thereby supporting rebar corrosion (Domone, 2001).

3.3. Strength development.

Strength of concrete takes place through the formation of hydrated calcium silicates 3CaO.2SiO2.3H2O referred to as C-H-S which binds the aggregate particles together. Strength rises rapidly in the first 7 days due to the presence of large amounts of reactants. The rate of strength gain slows down as the reactants become less and less and levels off at 28 days with little gain beyond 28 days. Most of the early strength is due to the hydration of the alite, which hydrates faster than the belite, and also generates the larger proportion of heat of hydration. Little strength is contributed by the hydration of the aluminate

and ferrite, and portlandite, Ca(OH)2, released by the hydration of the calcium silicates, has no strength value.

3.4. The role of portlandite in concrete.

$Ca(OH)_2$ and secondary alkalis KOH and NaOH create an alkaline environment in concrete that leads to the passivation of steel rebars and prevent their corrosion. The carbonation of $Ca(OH)_2$ also leads to the absorption and sequestration of CO_2 (Bertos, et al., 2004) thereby reducing global warming.

On the converse, several negative outcomes arise from the presence of free lime in concrete. In the presence of reactive siliceous or carbonaceous aggregates, the $Ca(OH)_2$ reacts with the aggregates to form gels which absorb free water in the pores of concrete and form large compounds that lead to swelling and rupture of concrete (Sims & Poole, 2003). On the other hand, the leaching of $Ca(OH)_2$ by salt free water results in efflorescence, a white deposit on the surface of concrete which defaces the structure as shown in figure 1. Attack of $Ca(OH)_2$ by an acid can also result in leachable salts. For instance, the reaction of $Ca(OH)_2$ with sulphuric acid leads to the formation of gypsum which is moderately soluble in water and can lead to efflorescence. In addition, the infusion of atmospheric carbon dioxide (CO_2) into the pores of concrete and its dissolution in the free water produces an acid that reacts with $Ca(OH)_2$ as shown in equations 6-7.

$$CO_2 + H_2O = H_2CO_3 \quad (6)$$

$$H_2CO_3 + Ca(OH)_2 = CaCO_3 + 2H_2O \quad (7)$$

As can be observed, the reactions result in the conversion of $Ca(OH)_2$ to limestone, $CaCO_3$ leading to reduction in the pH of the pore solution. This process is known as carbonation of concrete. This leads to enhanced rebar corrosion in reinforced concrete as the passivating oxide layer on the rebar is lost (Chi, et al., 2002), (Alexander., et al., 2007). Shrinkage arising from carbonation has also been reported (Domone, 2001).

Figure 1. Efflorescence from a leaking water tank.

3.5. Sulphate attack

Dissolved calcium sulphate reacts with aluminate in the pore solution in the presence of water to form a large compound known as ettringite as shown in equation 8 (Kelham, 2003)

$$C_3A + 3CaSO_4 + 32H_2O = C_3A\cdot 3CaSO_4\cdot 32H_2O \quad (8)$$

In pore solution of low pH, magnesium sulphate can attack the hydrated calcium silicates as shown in equation 9, leading to total loss of strength (Domone, 2001).

$$3CaO\cdot 2SiO_2\cdot 3H_2O + 3(MgSO_4\cdot 7H_2O) = 3(CaSO_4\cdot 2H_2O) + 3(Mg(OH)_2) + 2SiO_2 \quad (9)$$

In addition, in wet conditions and in temperatures below 15ºC, thaumasite, a rare compound with the formula $CaSiO_3\cdot CaCO_3\cdot CaSO_4\cdot 15H_2O$ can form in concrete from the calcium silicates already in cement paste, from calcium carbonate in limestone aggregates, inert fillers, or due to carbonation of $Ca(OH)_2$ in the cement paste, and from sulphate ions from the soil or ground water. This form of attack is known as thaumasite sulphate attack (TSA) and it destroys the binding properties of the cement paste leading to a complete loss of strength (Domone, 2001).

4.0 Environmental and sustainability concerns in Portland cement concrete.

4.1. High CO_2 emission.

Limestone or chalk, bearers of $CaCO_3$, constitute more than 60% of the raw materials used in the manufacture of Portland cement clinker (Moir, 2003). Its calcination during the production of clinker produces large amounts of CO_2 as shown in equation 10.

$$CaCO_3 \xrightarrow{(900\text{-}1200^oC)} CaO + CO_2\uparrow \quad (10)$$

Other sources of CO_2 are the exhaust fumes from quarrying machinery and transport vehicles, and from fossil fuels used to fire the kiln. It is estimated that the ratio of CO_2 generated per unit of Portland cement produced can be as high as 1:1 (Chandler, 2019). This makes Portland cement a major contributor to global warming.

4.2. High energy consumption in the production of cement.

It is estimated that the cement industry consumes 4-5 GJ of energy for every tonne of cement produced (Taylor, et al., 2006). This energy goes directly into the processes that produce cement. By comparison, the energy requirement to produce 1 tonne of steel from iron ore stands at about 18 GJ, and 6.5 GJ per tonne when scrap metal is used (MOHSEN & AKASH, 1998). However, most of the energy is recoverable and can be used in other industrial processes. For instance, the heat from the blast furnace can be harnessed to produce steam for electricity generation and used in purification of cast iron or in subsequent stages of manufacturing. Thus, cement manufacturing is considered the most energy intensive industry despite the lower consumption per tonne.

4.3. High consumption of raw materials in cement production.

The production of PC uses naturally occurring deposits of limestone, chalk, shale, bauxite, and gypsum. These are non-renewable natural minerals which if not used rationally are likely to be exhausted in any given area. It is estimated that to produce 1 ton of cement, 1.5 - 1.7 tons of these raw materials is consumed depending on the richness of the deposits (Gao, et al., 2016). This calls into question the sustainability of Portland cement production in any given locality.

4.4. High heat of hydration.

A lot of heat of hydration is produced during the hydration of the calcium silicates in PC. For instance, tests have shown that the hydration of alite releases over 500 J/g (Jansen, et al., 2011), and the heat generated by the reaction of aluminate with gypsum can average close to 900 J/g in the first 3 days (Civil Unlimited, 2022). In

large concrete structures, the accumulation of heat of hydration can result in a hot interior and a cold exterior. With subsequent cooling of the hot interior shrinkage occurs resulting in internal thermal cracks and weakening of the structure.

4.5. Low durability.

White a large proportion of low durability of concrete arises from human involvement in the design, production and placement of concrete, the use Portland cement contributes to a significant part of the problem. The presence of dormant $Ca(OH)_2$ in the cement paste promotes attack by acids, alkali aggregate reaction, and efflorescent. The leaching of salts from concrete by acids and salt free water increases the porosity of concrete and allows ingress of harmful gases and fluids which cause rapid destruction of concrete.

5.0 Mitigating negative effects of Portland cement concrete.

5.1. Environmental.

Environmental concerns in the use of concrete can be summarized as high CO_2 emissions particularly in the production of cement, and high consumption of non-renewable raw materials in the production of cement and as aggregates for concrete. High CO_2 emissions contribute to global warming. On the hand, high consumption of natural raw materials results in rapid depletion of resources and their exploitation degrade the landscape.

Most of the negative effects of PC can be mitigated by using less of the cement in the production of concrete. This results in a reduced CO_2 signature, less raw material consumption, and less energy demand. Cements in this category are already being produced. For instance, European CEM II incorporate up to 35% pozzolanic materials in PC, while CEM IV allows up to 55% PC replacement. The pozzolanic materials are usually naturally occurring volcanic rocks and ashes, fly ash, and silica fume. The latter two are industrial wastes from the burning of coal and from the silicon-based industries respectively. Tests have also shown that good concrete can be produced by blending CEM I, a pure PC, with a variety of ashes from the agriculture industry such as rice husks ash (RHA) (Mahmud, et al., 2010), sugar cane bagasse ash (SCBA) (Abdalla, et al., 2022), and corn cob ash (CCA) (Olafusi & Olutoge, 2012), (Kamau, et al., 2016). On the other hand, CEM III replaces Portland cement with up to 95% blast furnace slag (BFS), a waste product from the extraction of steel from ore.

5.2. Durability.

A pozzolan is defined as a siliceous or silico-aluminous material that will, in finely divided form and in the presence of moisture, chemically react with calcium hydroxide at ordinary temperatures to form compounds having cementitious properties (American Concrete Institute, 2013). The inclusion of a pozzolan in Portland cement therefore introduces compounds that react with $Ca(CO)_2$ in PC paste to produce more cementitious compounds, thereby increasing the late age strength of concrete. Typical pozzolanic reactions resulting in the formation of calcium silicate and aluminate hydrates are shown in equations 11-12 (Koteng & Chen, 2015).

$$Ca(OH)_2 + SiO_2 + H_2O \rightarrow C\text{-}S\text{-}H \quad (11)$$

$$Ca(OH)_2 + Al_2O_3 + H_2O \rightarrow C\text{-}A\text{-}H \quad (12)$$

The formation of calcium silico-aluminate hydrate has also been reported (Abdalla, et al., 2022).

$$Ca\ (OH)_2 + Al_2O_3 + SiO_2 + H_2O \rightarrow C\text{-}A\text{-}S\text{-}H \quad (13)$$

On the other hand, the $Ca(OH)_2$ in PC paste activates dormant calcium silico-aluminate compound in BFS leading to their hydration to form calcium silicate and calcium silico-

aluminate hydrates as shown in equation 14-15 (Jing, et al., 2020), (LIU, et al., 2017).

$$2CaO{\cdot}Al_2O_3{\cdot}SiO_2 + Ca(OH)_2 + H_2O \rightarrow C\text{-}S\text{-}H + Ca(OH)_2 \quad (14)$$

$$2CaO{\cdot}Al_2O_3{\cdot}SiO_2 + Ca(OH)_2 + H_2O \rightarrow C\text{-}A\text{-}S\text{-}H + Ca(OH)_2 \quad (15)$$

The larger C-S-H and C-A-S-H compounds produced result in increased densification of the pore structure resulting in enhanced durability.

5.3. Sustainability.

It has been shown that high consumption of non-renewable raw materials and high CO_2 emissions can largely be mitigated by partial replacement of PC clinker with a variety of CRMs. These are largely industrial and agricultural wastes which have little alternative use and their incorporation in cement solves their disposal problem. Less demand for PC can also be achieved by designing strong structures which carry the desired loads with smaller member sizes which consume less materials. If these structures can be made to last many years then the need to replace them is reduced and demand for PC is reduced.

1. Production of high-performance concrete.

6.1. Definition.

High performance concrete is defined as concrete meeting special combinations of performance and uniformity requirements that cannot always be achieved routinely using conventional constituents and normal mixing, placing, and curing practices (American Concrete Institute, 2013). It can be referred as concrete that meets the desired objectives in the best ways possible. For most structural applications the main objectives will be high flowability without segregation in the fresh state to ease placement, high strength to provide efficiency in material consumption, and high durability to reduce life cycle costs.

6.2. Materials.

The materials used will be dictated by the desired objectives. Aggregates should have high crushing and abrasion strength, be well graded, rounded, and have low water absorption. A maximum aggregate size (MAS) of 12.5 mm is recommended for most reinforced concrete structures to allow easy flow between obstacles such as rebars and service ducts. Moreover, small MAS reduces the effect of inherent weaknesses in the mass of aggregates and increases the surface area in contact with the binding paste. Cement with a good chemical composition will provide enhanced strength and durability to concrete. For instance, a binary PC-pozzolana cement or a ternary PC-BFS-pozzolana cement will convert Free $Ca(OH)_2$ is the paste to cementitious compounds thereby increasing strength, reduce durability problems associated with free $Ca(OH)_2$, and improve the densification of the pore structure resulting in very low permeability. Mixing water must be free of undesirable suspended particles and dissolved harmful chemicals. Concrete strength is inversely proportional to the water/binder (w/b) ratio therefore as little water as possible should be used in concrete production for the hydration of the binder. This will compromise the workability of concrete and the use of a workability enhancing admixture becomes mandatory.

6.3. Production.

The mixer type whether passive or active, the moisture content of aggregates, and the sequence of charging the mixer, all have effect on the rheology, consistency, and strength of the concrete. Since low w/b is used, it is important that the water provided is used to hydrate the binding powder and not absorbed by aggregates. In some cases, saturated surface dry aggregates are used but this brings into question the issue of reduced fire resistance from steam generated by free water in the pores of aggregates. In other cases, oven dried aggregates are used to address this problem. Also, the point at which the plasticising admixture is added needs consideration as the chemical composition of the cement may affect the performance of the

plasticiser. Tests have shown that forced action (paddle mixer) and charging the mixer in the sequence of water-powder-fine aggregate-coarse aggregate produces good results (Achini, et al., 2021).

6.4. Placement and curing.

Good handling, placement, and curing methods as recommended in the concrete standards must be observed. During curing loss of moisture is prevented so that the water provided can hydrate the cement fully. Curing can be achieved by applying a waterproof coating on the surface of fresh concrete. However, moist curing is to be preferred as it creplaces any moisture lost. The structure should be sprayed with water in the evening and the surface covered where possible to increase the period of moisture retention. Generally the concrete surface should be protected from sun and wind, both of which increase moisture loss. Curing should continue as long as practically possible.

7.0 Economic advantages of high-performance concrete.

7.1. Rapid placement.

High flowability in the fresh state allows pumping to achieve high volume placement at a go. This helps to control positions of cold joints which are locations of potential weakness. Pumping concrete also reduces crowding on site and potential accidents. Faster rate of concreting is achieved resulting in reduced construction time.

7.2. High early strength.

High early strength reduces formwork removal time. Formwork and supporting falsework are removed when concrete has attained enough strength to support the applied loads. Tests have shown that even with strength grade 32.5 cements made to EN 197, cube crushing strength of 35 MPa can be achieved in 3 days (Ofwa, et al., 2020), (Achini, et al., 2021). Early demoulding allows reuse of the same formwork and supporting falsework, early onset of finishing work and faster construction. This can result in early release of manpower and equipment to be deployed on the next job hence reducing the need to invest in additional manpower and new equipment.

7.3. High ultimate strength.

28-day cube crushing strengths in excess of 60 MPa which continue to rise with time to 80 MPa at 180 days have been achieved (Abdalla, et al., 2022) (Adam, et al., 2022). This ensures that strong structures utilising small member sizes can be built resulting in saving of materials. In addition, the overall weight of the structure is reduced and smaller foundations can be used.

7.4. High durability

High durability results in reduced life cycle costs as one structure can serve for many years with minimal maintenance. This also results in less demand for construction materials and supports sustainable use of construction materials, reduction of CO2 emissions and energy use associated with concrete. Degradation of the landscape from exploitation of raw materials is also reduced.

8.0 Discussion.

It has been shown that a large number of industrial and agricultural wastes can be incorporated into PC as CRMs thereby mitigating the environmental and sustainability concerns in the production and use of concrete. It has also been shown that the chemical composition of the binding powder has influence on the chemical activity in the concrete that leads to strength and durability, and that high early and long-term strengths and durability lead to rational consumption of raw materials and reduction of immediate and life cycle costs.

Besides many advantages of using CRMs, concrete consists of approximately 70% aggregates of different sizes. A large proportion consist of natural sand, natural gravel, and crushed rock all of which are non-renewable natural materials whose quarrying and exploitation often degrade the landscape. However, concrete has the capacity to use a variety of alternative post-consumer, industrial and agricultural wastes as alternative to, or partial

replacement of conventional aggregates, thereby reducing their consumption. These include crushed demolition concrete (Tu, et al., 2006), bricks (Debieb & Kenai, 2008), ceramics (AGRAWAL, et al., 2016), glass (Srivastava, et al., 2014), bones (Akinyele, et al., 2020), plastics (Silva, et al., 2012 (preprint)), crumb rubber (Son, et al., 2011), animal shells (Reena, 2021), and fruit shells (Katte, et al., 2022).

Since concrete is a man-made material often produced at the time of use, the performance of concrete largely depends on the skills deployed in its production, placement, finishing, and curing. Much attention must be focussed in this area. It has been observed that much of the concrete produced globally are not as good as they should be (Neville & Aitcin, 1998). The authors point out that there was neither lack of knowledge nor the need for new research to be able to make good concrete.

9.0 Conclusion.

Concrete is a material that can incorporate a wide variety of materials that have little alternative use. These have several advantages. First the consumption of traditional raw materials for concrete production are reduced allowing rational consumption and sustainable use. Secondly, the negative effects of CO_2 emission and degradation of the landscape are reduced allowing a more pleasant living environment. Thirdly, concrete solves the disposal problem for such materials which fall into the waste category.

Designing and producing good, environmentally friendly concrete relies heavily on the skills employed in the exercise. Therefore, this area requires a lot of attention.

Concrete has been in use for more than 9000 years and despite great population increases during this time, concrete is still in use without exerting pressure on the available global resource. It has proved to be a versatile and sustainable material that changes with technology and existing circumstances. There is no reason to believe that it will not be in use in the next 9000 years.

References

Abdalla, T. A., Koteng, D. O., Shitote, S. M. & Matallah, M., 2022. Mechanical and durability properties of concrete incorporating silica fume and a high volume sugarcane bagasse ash. *Results in Engineering*, Volume 16.

Abdalla, T. A., Koteng, D. O., Shitote, S. M. & Matallah, M., 2022. Mechanical Properties of Eco-friendly Concrete Made with Sugarcane Bagasse Ash. *Civil Engineering Journal*, 8(June), pp. 1227-1239.

Achini, I. K., Koteng, D. O. & Mwero, J. N., 2021. Effect of Mixing Method On The Rheology And Hardened Properties of Concrete With Low Water/Binder Ratio. *International Journal of Civil Engineering*, 8(10), pp. 1-8.

ACI Committee 232, 2000. *ACI 232 1R-00 Use of Raw or Processed Natural Pozzolans*, Farmington Hills, Michigan, USA: American Concrete Institute.

Adam, M. G. O., Koteng, D. O., Thuo, J. N. & Matallah, M., 2022. Analysing the Effect of Cassava Flour as a Mixture on the Physical, Mechanical, and Durability Properties of High-Strength Concrete. *Civil Engineering Journal*, 8(12), pp. 3866-3882.

AGRAWAL, A., SRIVASTAVA, V., HARISON, A. & SURYAVANSHI, S., 2016. USE OF CERAMIC AND PLASTIC WASTE IN CONCRETE: A REVIEW. *International Journal of Engineering Research-Online* , 4(3).

Akinyele, J. O., Kehinde, H. A. & Igba, U. T., 2020. STRUCTURAL EFFICIENCY OF CONCRETE CONTAINING CRUSHED BONE AGGREGATES. *ARID ZONE JOURNAL OF ENGINEERING, TECHNOLOGY & ENVIRONMENT*, 16(4), p. 813=820.

Alexander., M. G., Mackechnie, J. R. & Yam, W., 2007. Carbonation of concrete bridge structures in three South African localities. *Cement & Concrete Composites*, Volume 29, pp. 750-759.

American Concrete Institute, 2013. *ACI Concrete Terminology, ACI CT-13*, Farmington Hills, USA: American Concrete Institute.

Bertos, M. F., Simons, S., Hills, C. & Carey, P., 2004. A review of accelerated carbonation technology in the treatment of cement-based materials and sequestration

of CO2. *Journal of Hazardous Materials,* Volume B112, pp. 193-205.

Brooks, J., 2003. Elasticity, shrinkage,. In: J. Newman & B. S. Choo, eds. *Advanced Concrete Technology, Concrete Properties* . Oxford, UK: Butterworth-Heinemann, pp. 7 1-18.

Chandler, D. L., 2019. *World Economic Forum.* [Online]
Available at: https://www.weforum.org/agenda/2019/09/cement-production-country-world-third-largest-emitter/
[Accessed 28 December 2022].

Chi, J. M., Huang, R. & Yang, C. C., 2002. EFFECTS OF CARBONATION ON MECHANICAL PROPERTIES AND DURABILITY OF CONCRETE USING ACCELERATED TESTING METHOD. *Journal of Marine Science and Technology,* 10(1), pp. 14-20.

Civil Unlimited, 2022. *HEAT OF HYDRATION OF CEMENT – DETAILED EXPLANATION.* [Online] Available at: https://civilunlimited.com/heat-of-hydration-of-cement/
[Accessed 28 December 2022].

Debieb, F. & Kenai, S., 2008. The use of coarse and fine crushed bricks as aggregate in concrete. *Construction and Building Materials,* Volume 22, pp. 886-893.

Domone, P., 2001. Concrete. In: J. Illston & P. Domone, eds. *Construction Materials, Their nature and behaviour.* London, UK: Spon Press, pp. 89-223.

Gao, T. et al., 2016. Analysis of material flow and consumption in cement production. *Journal of Cleaner Production,* Volume 112, pp. 553-565.

Giatec Scientific Inc., 2022. *World population.* [Online]
Available at: https://countrymeters.info/en/World#:~:text=As%20of%201%20January%202022%2C%20the%20population%20of,births%20exceeded%20the%20number%20of%20deaths%20by%2096%2C617%2C035.
[Accessed 25 December 2022].

Gromicko, N. & Shepard, K., 1994. *The History of Concrete.* [Online]
Available at: https://www.nachi.org/history-of-concrete.htm
[Accessed 26 December 2022].

Harder, J., 2021. *ZKG Cement Lime Gypsum.* [Online]
Available at: https://www.zkg.de/en/artikel/zkg_Latest_trends_in_Africa_s_cement_industry_3696965.html
[Accessed 25 December 2022].

Irish Concrete Society, 1973. *History of Concrete..* [Online]
Available at: https://concrete.ie/about-concrete/history-of-concrete/
[Accessed 25 December 2022].

Jackson, M. D. et al., 2014. Mechanical resilience and cementitious processes in Imperial Roman architectural mortar. *Proceedings of the National Academy of Sciences,* 111(52), p. 18484–18489 |.

Jansen, D., Bergold, S. T., Goetz-Neunhoeffer, F. & Neubauer, J., 2011. The hydration of alite: a time-resolved quantitative X-ray diffraction approach using the G-factor method compared with heat release. *Journal of Applied Crystallography,* Volume 44, pp. 1-7.

Jing, W., Jiang, J., Ding, S. & Duan, P., 2020. Hydration and Microstructure of Steel Slag as Cementitious Material and Fine Aggregate in Mortar. *Molecules ,* 25(19), pp. 1-17.

Kamau, J., Ahmed, A., Hirst, P. & Kangwa, J., 2016. Suitability of Corncob Ash as a Supplementary Cementitious Material. *International Journal of Materials Science and Engineering,* 4(4), pp. 215-228.

Katte, A. R., Mwero, J., Gibigaye, M. & Koteng, D. O., 2022. Effect of saponification-based treatment of palm kernel shell aggregates on the mechanical properties of palm kernel shell aggregates concrete. *Construction and Building Materials,* 357(November), pp. 129-343.

Kelham, S., 2003. Acid, soft water and sulfate attack. In: J. Newman & B. S. Choo, eds. *Advanced Concrete Technology, Concrete Properties.* Oxford, UK: Butterworth-Heinemann, pp. 12 1-12.

Koteng, D. O. & Chen, C.-T., 2015. Strength development of lime–pozzolana pastes with silica fume and fly ash. *Construction and Building Materials,* Volume 84, p. 294–300.

Kramar, S. et al., 2011. Mineralogical and microstructural studies of mortars from the bath complex of the Roman villa rustica near Mošnje (Slovenia). *MATERIALS CHARACTERIZATION,* 52(July), p. 1042 – 1057.

LIU, S., HAN, W. & LI, Q., 2017. Hydration Properties of Ground Granulated Blast-Furnace Slag (GGBS) Under Different Hydration Environments. *MATERIALS SCIENCE,* 23(1), p. 1392–1320.

Li, Z., 2011. *Advanced Concrete.* Hoboken, New Jersey, USA: JOHN WILEY & SONS, INC.

Mahmud, H. B., Hamid, N. A. A. & Chi, K. Y., 2010. *Production of high strength concrete incorporating an agricultural waste - rice husk ash.* Cairo, Egypt, Institute of Electrical and Electronics Engineers.

MOHSEN, M. S. & AKASH, B. A., 1998. ENERGY ANALYSIS OF THE STEEL MAKING INDUSTRY. *INTERNATIONAL JOURNAL OF ENERGY RESEARCH,* Volume 22, pp. 1049-1054.

Moir, G., 2003. Cements. In: J. Newman & B. S. Choo, eds. *Advanced Concrete Technology: Constituent Materials.* Oxford, UK: Butterworth-Heinemann, pp. 1-45.

Neville, A. & Aitcin, P.-C., 1998. High performance concrete- An overview. *Materials and Structures/Mat~riaux et Constructions,* 31(March), pp. 111-117.

Ofwa, T. O., Koteng', D. O. & Mwero, J. N., 2020. Evaluating Superplasticizer Compatibility in the Production of High Performance Concrete using Portland Pozzolana Cement CEM II/B-P. *International Journal of Civil Engineering,* 7(6), pp. 92-100.

Olafusi, O. S. & Olutoge, F. A., 2012. Strength Properties of Corn Cob Ash Concrete. *Journal of Emerging Trends in Engineering and Applied Sciences,* 3(2), pp. 297-301.

Papayianni, I. & Pachta, V., 2016. *THE EVOLUTION OF THE BINDING AGENTS' TECHNOLOGY,* Thessaloniki, Greece: Laboratory of Building Materials, Dept. of Civil Engineering, Aristotle University of Thessaloniki.

Paul, A., 2016. *The Civil Engineering website.* [Online]
Available at: ttps://civildigital.com/use-of-synthetic-fibres-in-concrete-flooring-and-plastering-advantages [Accessed 26 December 2022].

Portland Cement Association, 2015. *Global Cement Consumption on the Rise,* Skokie, Illinois, USA: Portland Cement Association.

Reena, L., 2021. Partial Replacement of Oyster Shells as Coarse Aggregate in Concrete. *International Journal of Engineering Research & Technology,* 10(4), pp. 136-138.

Silva, R. V., deBrito, J. & Salkia, N., 2012 (preprint). Influence of curing conditions on the durability-related performance of concrete made with selected plastic waste aggregates. *Cement & Concrete Composites.*

Sims, I. & Poole, A., 2003. Alkali–aggregate reactivity. In: J. Newman & B. S. Choo, eds. *Advanced Concrete Technology, Concrete Properties.* Oxford, UK: Butterworth-Heinemann, pp. 13 1-37.

Son, K. S., Hajirasouliha, I. & Pilakoutas, K., 2011. Strength and deformability of waste tyre rubber-filled reinforced concrete columns. *Construction and Building Materials,* Volume 25, pp. 218-226.

Srivastava, V., Gautam, S. P., Agarwal, V. C. & Mehta, P. K., 2014. Glass Wastes as Coarse Aggregate in Concrete. *Journal of Environmental Nanotechnology,* 3(1), pp. Volume 3, No.1 pp. 67-71.

Stefanidou, M. et al., 2013. Analysis and characterization of hydraulic mortars from ancient cisterns and baths in Greece. *Materials and Structures.*

Taylor, M., Tam, C. & Gielen, D., 2006. *Energy Efficiency and CO2 Emissions from the Global Cement Industry ,* Paris, France: Energy Technology Policy Division, International Energy Agency .

Tsung-Yueh Tu a, ∗. Y.-Y. C. b., n.d. Properties of HPC with recycled aggregates.

Tu, T.-Y., Chen, Y.-Y. & Hwang, C.-L., 2006. Properties of HPC with recycled aggregates. *Cement and Concrete Research,* Volume 36, p. 943–950.

SCALING UP NEW FRONTIERS OF KNOWLEDGE ENGINEERING AND DISSEMINATION – PRESIDENT'S MESSAGE

The Institution of Engineers of Kenya (IEK) is the learned society of the engineering profession and co-operates with national and international institutions in developing and applying engineering to the benefit of humanity.

One of the ideals and objectives of the institution is to promote, encourage and improve the application of engineering to technical and other related practices. In addition, the institution also facilitates the exchange of information and ideas on technical and other related matters.

The engineering fraternity in the African continent has in the recent past witnessed a convergence of purpose and vision from all the arms of the engineering practice. The societies representing the welfare of engineers are collaborating at a more enhanced level more than ever before. One of the most important collaborations is that between the industry and the academia. In the African continent, there is visible collaboration between professional engineering institutions with more countries joining the Federation of African Engineering Organizations (FAEO) to unleash engineering opportunities in African Continental Free Trade Area (ACFTA).

At the regulatory level, Registrars of the Engineering Boards and Councils are coming together to unify and establish a common baseline that will define the licensing of practicing engineers. At the academic level, collaborations between universities offering engineering courses continue to scale up the ladder of mutual recognition agreements.

The Institution of Engineers of Kenya (IEK) has responded to the need for a platform for engineers in academia who include students at Masters and PHD levels together with researchers in the industry be able to share and compare domain specific discoveries. The African Journal for Engineering, Research and Innovation (AJERI) becomes a vehicle through which this collaboration will be achieved.

The Editorial team of the AJERI comprises of carefully searched accomplished and world class recognized engineering academicians and practitioners. The composition of the editorial team represents the face of Africa in both inclusion and diversity.

The articles that will be carried by AJERI will come from all over the world and the peer-reviewers will constitute a resource pool that will be a rich blend from world class universities and research institutions.

I acknowledge the effort and the work done by IEK members and the editorial team in the journey towards the realization of a dream come true for IEK. AJERI will add on to the portfolio mix of the rich blend of publications by the institution.

I would like to thank our key sponsor for the first issue of AJERI, the Engineers Board of Kenya (EBK) for walking with us and partnering to see the first issue of AJERI released in a timely manner.

I call upon all researchers and students of institutions of higher learning to take advantage of this platform that has been provided by IEK, to share research findings in all the engineering fields through publishing with AJERI.

Eng. Erick Ohaga, CE, FIEK, MKIM, AMCIARB (UK)

President Institution of Engineers of Kenya

THE LAUNCH OF THE AFRICAN JOURNAL OF ENGINEERING RESEARCH AND INNOVATION (AJERI) - HON. SEC's MESSAGE

The launch of The African Journal of Engineering Research and Innovation (AJERI) on 4th March 2023 is a key step in fulfilment of one of IEK's strategic goal. There was no better time to launch AJERI than 50 years after IEK was founded and on its 51st year.

The peer-reviewed journal will provide a platform for all engineers and engineering practitioners in the world to publish their original research and innovations. The journal comes at the right time when Africa is awakening the giant within.

Africa has produced some foremost thinkers and intellectuals in engineering. However, they have not had a platform they can easily identify with as an avenue to publish their works. AJERI comes in to fill this gap and more importantly as a platform for exchange of ideas to foster a vibrant industry and academia discourse. This will address the myriad and current issues affecting the society now and into the future.

Since many postgraduate students are required to publish their works in a peer-reviewed journal before they graduate, AJERI provides this platform for them. With scholars and practicing engineers drawn from all of Africa forming the panel of peer-reviewers, AJERI promises to be a very important outlet for original ideas of researchers and intellectuals.

Indeed Africa has come of age and this journal communicates just that; that engineers and engineering in Africa has matured and will add to the global body of knowledge. AJERI will play its role in curing the dearth of publishing from this part of the world.

We now invite scholars, practicing engineers and researchers from all over the world to find an avenue to let the world interact with their ideas through AJERI.

Eng. Shammah Kiteme, CE, MIEK
Honorary Secretary
The Institution of Engineers of Kenya

ENGINEERS BOARD OF KENYA WELCOMES THE OFFICIAL LAUNCH AND FIRST ISSUE OF JOURNAL OF ENGINEERING RESEARCH AND INNOVATION (AJERI)

The Engineers Board of Kenya (EBK) is pleased to welcome the inaugural launch of African Journal of Engineering Research and Innovation (AJERI). The Journal will provide the much-needed space for the generation of knowledge, dialogue, critique, debate, and collaboration among an international community on engineering and innovations.

The Board envisions that AJERI will make it possible for engineers to connect to each other, develop the engineering field and to be directly involved in ongoing regional and global knowledge construction. AJERI should strive to create a high-quality publication that will be relevant, challenging, thought-provoking, and inclusive of a diverse range of voices and perspectives, including graduate students, academic researchers and scholars, policymakers, innovators, inventors, and the entire industry. This can only be made possible through the publication of original research, theoretical contributions, reviews of the literature, critical commentaries, case studies, and book reviews.

The legal framework on the regulation and development of engineering practice in Kenya as provided for under the Engineers Act 2011 offers the Board the opportunity and obligation to carry various functions in the engineering value chain. The Act makes the Board a regulator as well as an agent of the development of the profession. The Board in effect has offered itself as the liaison between the industry and the academia by engaging the academia to understand the requirements of the industry and seek conformity to these standards.

The Engineers Act further empowers the Board to publish and disseminate materials relating to its work and activities. The Journal will therefore in a big way help the Board in the furtherance of its mandate in education, training and practice. The Journal is specifically key in the delivery of academia industry linkage through research-based solutions. AJERI is a perfect platform to publish progress on the collaboration between Academia and the State Department of Roads on Research and Capacity Building for Sustainable Road Infrastructure. The collaboration objectives aims at promoting collaborative research, nurturing the application of local Knowledge and innovations. The collaboration also seeks to initiate and enhance technical collaborations between the academia and Road Agencies and promote efficient use of road networks through application of innovative and modern technologies. The Board will champion similar collaborations to be replicated in all the sectors of the economy.

The Engineers Board of Kenya is therefore excited to be part of this inaugural launch of AJERI and looks forward to its success in the subsequent issues.

Eng. Erastus K. Mwongera CBS, CE, FIEK
Chairman-Engineers Board of Kenya

ENGINEERS BOARD OF KENYA
Enhancing Professionalism

About the Engineers Board of Kenya

The Engineers Board of Kenya (EBK) is a statutory body established under section 3(1) of the Engineers Act, 2011. The Board is responsible for the registration of Engineers and Engineering firms, regulation of engineering professional services, setting of standards, development, and general practice of engineering

MESSAGE FROM THE REGISTRAR ENGINEERS BOARD OF KENYA

The Board is proud to partner with The Institution of Engineers of Kenya (IEK) in the launch and first issue of African Journal of Engineering Research and Innovation (AJERI). The confluence of various emerging engineering knowledge and practices like the Outcome Based Education (OBE), liberalization of professional engineering services also known as trade in services under the East Africa Community (EAC) and the African Continental Free Trade Area (AfCFTA), and innovative financing of projects makes this journal especially timely.

The AJERI provides a platform to strengthen the quintuple helix model involving academia, industry, government, and society. The collaboration between industry, academia, government, society, and the regulatory bodies should form one interdependent ecosystem that leads to the development of funding models to sustain it. Collaboration should make it possible for the academia to understand the societal challenges while industry is able to solve the challenges and make life better. The industry-academia engagement will therefore minimize challenges of funding and lack of focused research whose findings are not readily consumed by the industry, and bridge gaps amongst actors in the engineering value chain.

The Engineers Board of Kenya has several ongoing programs to strengthen these linkages while developing capacities for engineers. The Board has in place Academia Based Graduate Engineers Internship Programme, the Collaboration Between Academia and the State Department of Roads on Research and Capacity Building for Sustainable Road Infrastructure, various programmes in preparations towards acceding to Washington Accord that includes, training of engineering academic staff on OBE, and training of Accessors. The Board is also actively involved in Trade in Service negotiation in the region and Africa and shall be able to make periodic updates in this Journal. The Board will also hold the Engineering Partnership Convention (EPC) 2023 in June 2023. Emerging engineering practices that include intelligent application systems, innovative financing and climate action plans will generate lots of dialogue and development of standards, manuals and guidelines that will find themselves in AJERI.

The African Journal of Engineering Research and Innovation (AJERI) therefore presents opportunities to put some bold and innovative ideas on the table. Congratulations!

Eng. Margaret N. Ogai, CE
Registrar/ CEO
Engineers Board of Kenya

Editorial Committee

Name	Category	Country
Eng. Prof. Lawrence Gumbe	Chair	Kenya
Eng. Prof. Leonard Masu	Secretary	Kenya
Eng. Prof. Ayodeji Oluleye	Member	Nigeria
Eng. Dr. Slah Msahli	Member	Tunisia
Eng. Prof. Bernadette W. Sabuni	Member	Kenya
Prof. Anish Kutien	Member	South Africa

Editorial Board

	Name
Chairperson:	Eng. Prof. Lawrence Gumbe
Members:	Eng. Paul Ochola- Secretary
	Eng. Sammy Tangus- Treasurer
	Eng. Erick Ohaga – President, IEK
	Eng. Shammah Kiteme- Honorary Secretary, IEK
	Eng. Prof. Leornard Masu
	Eng. Margaret Ogai
	Eng. Nathaniel Matalanga
	Eng. Dr. Sam Roy Orenge – Technical Editor

INSTRUCTIONS TO CONTRIBUTORS

The editorial staff of the AJERI requests contributors of articles for publication to observe the following editorial policy and guidelines accessible at https://www.iekenya.org/ in order to improve communication and to facilitate the editorial process.

Criteria for Article Selection

Priority in the selection of articles for publication is that the articles:

a. Are written in the English language
b. Are relevant to the application relevant of engineering and technology research and Innovation
c. Have not been previously published elsewhere, or, if previously published are supported by a copyright permission
d. Deals with theoretical, practical and adoptable innovations applicable to engineering and technology
e. Have a 150 to 250 words abstract, preceding the main body of the article
f. The abstract should be followed by a list of 4 to 8 "key Words"
g. Manuscript should be single-spaced under 4,000 words (approximately equivalent to 5-6 pages of A4-size paper)
h. Are supported by authentic sources, references or bibliography

Rejected/Accepted Articles

a. As a rule, articles that are not chosen for AJERI publication are not returned unless writer (s) asks for their return and are covered with adequate postage stamps. At the earliest time possible, the writer (s) is advised whether the article is rejected or accepted.
b. When an article is accepted and requires revision/modification, the details will be indicated in the return reply from the AJERI Chief Editor, in which case such revision/modification must be completed and returned to AJERI within three months from the date of receipt from the Editorial Staff.
c. Complementary copies: Following the publishing, three successive issues are sent to the author(s)

Procedure for Submission

a. Articles for publication must be sent to AJERI on the following address:

The Chief Editor
African Journal of Engineering Research and Innovation
P.O Box 41346- 00100
City Square Nairobi Kenya
Tel: +254 (20) 2729326, 0721 729363, (020) 2716922
E-mail: editor@iekenya.org

b. The article must bear the writer (s) name, title/designation, office/organization, nationality and complete mailing address. In addition, contributors with e-mail addresses are requested to forward the same to the Chief Editor for faster communication.

For any queries, authors are requested to contact by mail (editor@iekenya.org).

PUBLISHER

The Institution of Engineers of Kenya

P.O Box 41346- 00100
City Square Nairobi Kenya
Tel: +254 (20) 2729326, 0721 729363, (020) 2716922
Email: editor@iekenya.org
Website: www.iekenya.org

PRINTED BY

MichiMedia Limited

Vision Plaza, Mombasa Road,
P.O Box 4653-00506
Nairobi Kenya
Cell: +254 722 999 361
Tel: +254 2023631270
Email: info@michi-media.com

In partnership with


REPUBLIC OF KENYA
ENGINEERS BOARD OF KENYA
epc 2022
ENGINEERING PARTNERSHIPS CONVENTION | 2023
4TH ENGINEERING PARTNERSHIPS CONVENTION
Growing Kenya's Economy – Engineers' Contribution to Development
1 NO POVERTY
4 QUALITY EDUCATION
8 DECENT WORK AND ECONOMIC GROWTH
9 INDUSTRY, INNOVATION AND INFRASTRUCTURE
11 SUSTAINABLE CITIES AND COMMUNITIES
17 PARTNERSHIPS FOR THE GOALS
Pillars of the Convention
1 Engineering and Economic Development
2 Developing the Engineering Professional
3 Liberalizing Professional Engineering Services in the East African Community and AFCTA
4 Enhancing Compliance for Delivery of Safe, Efficient, and Effective Infrastructure
Date: 14th to 16th June 2023
Venue: Naivasha, Nakuru County
18 PDUs
Charges
Virtual - Kshs. 5,000
Physical - Kshs. 45,000
+254 202 719 974 | +254 722 509 972 info@ebk.go.ke www.ebk.go.ke
Kenya VISION 2030
acek

CONTENTS **Pages**